

LOW TEMPERATURE LASER-INDUCED FLUORESCENCE STUDIES OF
CHROMOPHORES IN SOFT SOLIDS AND BIOLOGICAL MATTER

by

CHEN LIN

B.S., Beijing University of Aeronautics and Astronautics, 2007

AN ABSTRACT OF A DISSERTATION

submitted in partial fulfillment of the requirements for the degree

DOCTOR OF PHILOSOPHY

Department of Chemistry
College of Arts and Science

KANSAS STATE UNIVERSITY
Manhattan, Kansas

2013

Abstract

Low-temperature laser-induced fluorescence spectroscopy has various applications in analytical, physical, and biophysical chemistry. This technique provides information on the fluorescence origin band, zero-phonon lines and phonon-sidebands, inhomogeneous broadening, electron-phonon coupling strength, and ground- and excited-state vibrational frequencies of studied molecules. Examples discussed in this work include studies of DNA/metabolites and monoclonal antibody (mAb)/antigen interactions. The structural basis for the increased reactivity of BPDE towards guanines at 5-methylcytosine (^{Me}C):G sites in DNA was investigated by low temperature laser-based spectroscopy, studying the nature of physical complexes of benzo[*a*]pyrene tetraol in a series of 5-methylcytosine structural DNA analogs. We found that the presence of a C-5 substituent on cytosine and related structural modifications influences the conformation of BPT in DNA analogs, and could explain the increase in guanine reactivity at ^{Me}C:G sites of the *p53* tumor suppressor gene that contains endogenous 5-^{Me}C. It has been demonstrated that various mAbs can bind a particular cross-reactant by adopting two distinct “red” and “blue” conformations of its binding sites. We showed that the blue conformation of pyrene in several mAbs (including 4D5 mAb) is consistent with π -cation interactions, underscoring the importance of π -cation interaction in ligand binding. We propose that considerable narrowing of the fluorescence origin band of the ligand in the protein environment could be regarded as a simple indicator of π -cation interactions. It is also shown that time-resolved delta fluorescence line-narrowing (Δ FLN) spectroscopy, using excitation within the (0,0)-transition band, provides more reliable information of the frequency dependence of the electron-phonon coupling (Huang-Rhys factor, S). Finally, analytical formulas were developed to describe FLN spectra with excitation energy transfer present. Our calculated FLN spectra are compared with spectra obtained by a simple convolution method (SC) and a more rigorous treatment using Redfield theory. We demonstrate that, under the condition of weak coupling between pigments (i.e., the coupling constant is smaller than the reorganization energy) and weak electron-phonon coupling strength ($S < 1$), our analytical formulas provide an excellent approximation of the SC and Redfield methodologies. We argued that our approach could also model FLN spectra obtained for very complex biological systems.

LOW TEMPERATURE LASER-INDUCED FLUORESCENCE STUDIES OF
CHROMOPHORES IN SOFT SOLIDS AND BIOLOGICAL MATTER

by

CHEN LIN

B.S., Beijing University of Aeronautics and Astronautics, 2007

A DISSERTATION

submitted in partial fulfillment of the requirements for the degree

DOCTOR OF PHILOSOPHY

Department of Chemistry
College of Arts and Sciences

KANSAS STATE UNIVERSITY
Manhattan, Kansas

2013

Approved by:

Major Professor
Ryszard Jankowiak

Copyright

CHEN LIN

2013

Abstract

Low-temperature laser-induced fluorescence spectroscopy has various applications in analytical, physical, and biophysical chemistry. This technique provides information on the fluorescence origin band, zero-phonon lines and phonon-sidebands, inhomogeneous broadening, electron-phonon coupling strength, and ground- and excited-state vibrational frequencies of studied molecules. Examples discussed in this work include studies of DNA/metabolites and monoclonal antibody (mAb)/antigen interactions. The structural basis for the increased reactivity of BPDE towards guanines at 5-methylcytosine (^{Me}C):G sites in DNA was investigated by low temperature laser-based spectroscopy, studying the nature of physical complexes of benzo[*a*]pyrene tetraol in a series of 5-methylcytosine structural DNA analogs. We found that the presence of a C-5 substituent on cytosine and related structural modifications influences the conformation of BPT in DNA analogs, and could explain the increase in guanine reactivity at ^{Me}C:G sites of the *p53* tumor suppressor gene that contains endogenous 5-^{Me}C. It has been demonstrated that various mAbs can bind a particular cross-reactant by adopting two distinct “red” and “blue” conformations of its binding sites. We showed that the blue conformation of pyrene in several mAbs (including 4D5 mAb) is consistent with π -cation interactions, underscoring the importance of π -cation interaction in ligand binding. We propose that considerable narrowing of the fluorescence origin band of the ligand in the protein environment could be regarded as a simple indicator of π -cation interactions. It is also shown that time-resolved delta fluorescence line-narrowing (Δ FLN) spectroscopy, using excitation within the (0,0)-transition band, provides more reliable information of the frequency dependence of the electron-phonon coupling (Huang-Rhys factor, S). Finally, analytical formulas were developed to describe FLN spectra with excitation energy transfer present. Our calculated FLN spectra are compared with spectra obtained by a simple convolution method (SC) and a more rigorous treatment using Redfield theory. We demonstrate that, under the condition of weak coupling between pigments (i.e., the coupling constant is smaller than the reorganization energy) and weak electron-phonon coupling strength ($S < 1$), our analytical formulas provide an excellent approximation of the SC and Redfield methodologies. We argued that our approach could also model FLN spectra obtained for very complex biological systems.

Table of Contents

List of Figures	ix
List of Tables.....	xi
List of Abbreviations.....	xii
Chapter 1 General Introduction	1
1.1 General Overview	1
1.2 Basic Aspects of Fluorescence Line-Narrowing (FLN) Spectroscopy	4
1.2.1 Homogenous and Inhomogeneous Broadening	4
1.2.2 Zero-Phonon Lines and Phonon Sidebands	6
1.2.3 Electron-Phonon Coupling Strength	10
1.2.4 Lineshape Function of FLN Spectra	11
1.2.5 Origin Band Excitation—Ground-State Vibrational Frequencies	13
1.2.6 Vibronically Excited FLNS—Excited-State Vibrational Frequencies.....	15
1.2.7 Delta Fluorescence Line-Narrowing Spectroscopy (Δ FLNS)	18
1.3 Excitation Energy Transfer (EET) and Modeling Study.....	18
1.3.1 EET and Coupling Constant	18
1.3.2 Convolution Method	20
1.3.3 Redfield Theory	22
1.4 Organization of Thesis	25
References.....	26
Chapter 2 Influence of C-5 Substituted Cytosine and Related Nucleoside Analogs on the Conformation of Benzo[<i>a</i>]pyrene Tetrol (BPT)/DNA Complex: Spectroscopic Study	31
2.1 Introduction.....	34
2.2 Materials and Methods.....	38
2.2.1 Low Temperature Fluorescence Spectroscopy	40
2.3 Results.....	41
2.3.1 Selection of Nucleobase Analogs and Oligonucleotide Synthesis.....	41

2.3.2 Spectroscopic Studies of BPT Complexed with Oligonucleotide Duplex Sequence Derived from p53 exon 5 and its C-5 Analogs	42
2.4 Discussion and Conclusion	45
References	48
Chapter 3 On Stabilization of a Neutral Aromatic Ligand by π -Cation Interactions in Monoclonal Antibodies	53
3.1 Introduction	55
3.2 Materials and Methods	57
3.2.1 Low-temperature Fluorescence Spectroscopy	57
3.3.2 Monoclonal Antibodies (mAbs)	58
3.2.3 Haptens	59
3.2.4 Computational Methodologies	59
3.3 Results	60
3.3.1 Conformation of Py/4D5 mAb complex	60
3.3.2 NLN Fluorescence Spectra of Py Complexed with anti-PAH and 4D5 mAbs ...	62
3.3.3 Calculated (0,0) bands	66
3.3.4 FLN spectra obtained for free Py and various Py/mAb complexes	68
3.4 Discussion	74
3.4.1 Comments on Control Experiments – Specificity of Binding	74
3.4.2 the Origin of Conformations I and II	75
3.5 Conclusions	76
References	77
Chapter 4 Fluorescence line-narrowing difference spectra: dependence of Huang-Rhys factor on excitation wavelength	80
4.1 Introduction	81
4.2 Experiments	83
4.3 Results	84

4.4	Discussion.....	87
4.4.1	Challenges in Measuring the S -Factor	87
4.4.2	Effect from Line Width of ZPL and Excitation Laser.....	88
4.4.3	On Spectroscopy of Pyrene.....	89
4.4.4	Intermolecular Repulsive-Dispersive Potentials: Variation of S within IDF	92
4.5	Conclusions.....	99
	Reference	100
Chapter 5	Modeling of Fluorescence Line-Narrowed Spectra in Weakly Coupled Dimers	103
5.1	Introduction.....	105
5.2	Derivation of Analytical Formulas to Calculate FLN Spectra in the presence of EET	107
5.3	Results and Discussion	111
5.3.1	Spectral Density	111
5.3.2	Building Single-Site Spectrum for the Analytical Formula Method	112
5.3.3	Comparison of Three Calculation Methods to Obtain FLN Spectra	113
5.3.4	Fluorescence Line-Narrowing Spectra of CP47 Antenna Complex	121
5.4	Conclusions.....	123
	References.....	125
Chapter 6	Concluding Remarks and Future Prospects	128
	References.....	129
Appendix A	Supporting Information for Chapter 5.....	130

List of Figures

Figure 1-1. Schematic view of homogeneous and inhomogeneous broadening.	5
Figure 1-2. Schematic view of inhomogeneously broadened fluorescence origin band and fluorescence ZPL and PSB.	8
Figure 1-3. Configurational coordinate diagram for the analysis of the optical transition between the ground (E_0) and excited (E_1) states.	9
Figure 1-4. Diagram of potential curves in linear electron-phonon coupling and molecular line shapes of corresponding transitions.	12
Figure 1-5. Origin band excitation in FLNS.	14
Figure 1-6. Jablonski diagram of FLNS and absorption cross section of vibronic transition and resulting FLN spectrum.	17
Figure 1-7. Schematic of the electronic coupling between the two pigments donor (D) and acceptor (A), giving rise to either electron transfer or EET.	19
Figure 1-8. Schematic view of systems with weakly and strongly coupled chromophores.	23
Scheme 2-1. Metabolic activation of benzo[<i>a</i>]pyrene to BPDE and the formation of guanine adducts.	36
Scheme 2-2. Nucleoside analogs employed in the study.	39
Figure 2-1. Low temperature (77 K) fluorescence origin band spectra of BPT obtained in the absence and in the presence of DNA duplexes.	43
Figure 3-1. Model of the 4D5 mAb fragment with Py docked in the lowest binding energy conformation in the mAb binding pocket represented by its molecular surface.	61
Figure 3-2. Low temperature NLN fluorescence spectra of immunocomplexed Py in <i>anti</i> -PAH mAb and 4D5 mAb.	64
Figure 3-3. Py of nine calculated lowest-energy conformations inside the binding pocket of 4D5 mAb.	67
Figure 3-4. FLN spectra of Py in various mAbs at $T = 4.2$ K obtained with λ_{ex} of 364 nm.	69
Figure 3-5. FLN spectra of Py in various mAbs at $T = 4.2$ K obtained with $\lambda_{\text{ex}} = 358.5$ nm. ...	70

Figure 3-6. FLN spectra of Py in various mAbs at T = 4.2 K obtained with λ_{ex} of 354 nm.	71
Figure 4-1. FLN spectra of Py in ethanol glass at T = 5 K.	85
Figure 4-2. Fluorescence origin-band and origin-band excited Δ FLN spectra of Py in ethanol glass at T = 5 K obtained at various excitation wavelengths.	86
Figure 4-3. Calculated inhomogeneous band and frequency-dependance of S factor.	95
Figure 4-4. Frequency-dependance of S factor within IDF from experimental data.	98
Figure 5-1. Calculated spectra of weakly coupled dimer with degenerate site energies at 15000 cm^{-1} . $V_{\text{AB}} = 0 \text{ cm}^{-1}$; Γ_{inh} is 200 cm^{-1} ; Huang-Rhys factor $S = 0.2$	115
Figure 5-2. Calculated spectra of weakly coupled dimer with degenerate site energies at 15000 cm^{-1} . $V_{\text{AB}} = 0 \text{ cm}^{-1}$; Γ_{inh} is 200 cm^{-1} ; Huang-Rhys factor $S = 0.8$	116
Figure 5-3. Calculated spectra of weakly coupled dimer with degenerate site energies at 15000 cm^{-1} . $V_{\text{AB}} = 25 \text{ cm}^{-1}$; Γ_{inh} is 200 cm^{-1} ; Huang-Rhys factor $S = 0.8$	119
Figure 5-4. Calculated and experimental FLN spectra of CP47.	122
Figure A-1. Calculated spectra of weakly coupled dimer site energies at 14950 cm^{-1} and 15050 cm^{-1} . $V_{\text{AB}} = 0 \text{ cm}^{-1}$; Γ_{inh} is 200 cm^{-1} ; Huang-Rhys factor $S = 0.2$	130
Figure A-2. Calculated spectra of weakly coupled dimer site energies at 14950 cm^{-1} and 15050 cm^{-1} . $V_{\text{AB}} = 0 \text{ cm}^{-1}$; Γ_{inh} is 200 cm^{-1} ; Huang-Rhys factor $S = 0.8$	131
Figure A-3. Calculated spectra of weakly coupled dimer with degenerate site energies at 15000 cm^{-1} . $V_{\text{AB}} = 25 \text{ cm}^{-1}$; Γ_{inh} is 200 cm^{-1} ; Huang-Rhys factor $S = 0.2$	132
Figure A-4. Calculated spectra of weakly coupled dimer site energies at 14950 cm^{-1} and 15050 cm^{-1} . $V_{\text{AB}} = 25 \text{ cm}^{-1}$; Γ_{inh} is 200 cm^{-1} ; Huang-Rhys factor $S = 0.2$	133
Figure A-5. Calculated spectra of weakly coupled dimer site energies at 14950 cm^{-1} and 15050 cm^{-1} . $V_{\text{AB}} = 25 \text{ cm}^{-1}$; Γ_{inh} is 200 cm^{-1} ; Huang-Rhys factor $S = 0.8$	134

List of Tables

Table 3-1. Spectral characteristics of Py/ <i>anti</i> -PAH mAb and Py/4D5 mAb complexes in PBS and G/PBS (1:1) matrices at 4.2 K.	65
Table 3-2. Calculated (0,0) Transition of Py in Py/4D5.	67
Table 4-1. Apparent Huang-Rhys factor values at different wavelengths for pyrene in EtOH glass at 5 K.	86

List of Abbreviations

α	Debye-Waller factor	Γ_{hom}	(width of) homogeneous
Ab	antibody		broadening
AE	analytical expression	Γ_{inh}	(width of) inhomogeneous
(-)-anti-BP	(-)-anti-benzo[<i>a</i>]pyrene- <i>s</i> -7, <i>t</i> -8-		broadening
DE	dihydrodiol- <i>t</i> -9,10-epoxide	Dft	2,4- difluorotoluene
(±)-anti-	(±)-anti-benzo[<i>a</i>]pyrene- <i>r</i> -7, <i>t</i> -8-	dPER	perimidine-2-one
BPDE	dihydrodiol- <i>t</i> -9,10-epoxide		deoxyribonucleoside
Arg	arginine	E_{λ}	reorganization energy
B[<i>a</i>]P	benzo[<i>a</i>]pyrene	EET	excitation energy transfer
BChl	bacteriochlorophylls	el-ph	electron-phonon
BP78D	benzo[<i>a</i>]pyrene-7 <i>S</i> - <i>trans</i> -7,8-	Et-C	5-ethylcytosine
	dihydrodiol	EtOH	ethanol
BPDE	benzo[<i>a</i>]pyrene diol epoxide	F-C	5-fluorocytosine
(+)-BP-diol	(+)-benzo[<i>a</i>]pyrene-7 <i>S</i> - <i>trans</i> -7,8-	FLN	fluorescence line-narrowing
	-dihydrodiol	ΔFLNS	delta fluorescence
BPT	benzo[<i>a</i>]pyrene- <i>r</i> -7, <i>t</i> -8,9,10-		line-narrowing spectroscopy
	tetrahydroetraol	FMO	Fenna-Mathews-Olson
Br-C	5-bromocytosine	FWHM	full-width at half maximum
CD	circular dichroism	Glu	glutamine
CDR	complementarity determining	(S)HB	(spectral) hole-burning
	region	HG-HL	half-Gaussian half-Lorentzian
CE	capillary electrophoresis	HPLC-ESI	high performance liquid
Chl	chlorophylls	- MS/MS	chromatography-electrospray
Cl-C	5-chlorocytosine		ionization-tandem mass
CW	continuous wave		spectrometry

I-C	5-iodocytosine	PBS	phosphate-buffered saline buffer
IDF	inhomogeneous distribution function	PDA	point-dipole approximation
$J(\omega)$	spectral density	PDB	protein data bank
LIF	laser-induced fluorescence	Pr-C	5-pro-pynylcytosine
L-J	Lennard-Jones	Prop-C	5-propylcytosine
Lys	lysine	PSB	phonon sideband
mAb	monoclonal antibody	Py	pyrene
MALDI-	matrix-assisted laser desorption	pyrrolo-C	5-pyrrolocytosine
TOF MS	ionization mass spectrometry with time-of-flight detection	RA	Redfield approach
^{Me}C	5-methylcytosine	RHB	resonant hole-burning
N^2-BPDE-	7,8,9-trihydroxy-10-(N^2 -	S	Huang-Rhys factor
dG	deoxyguanosyl)-7,8,9,10-tetrahydrobenzo[<i>a</i>]pyrene	SCM	simple convolution method
N^4Et-C	N^4 -ethylcytosine	SDF	site-distribution function
NLN	non-line narrowing	TrEsp	transition charges from electrostatic potentials
NPHB	non-photochemical hole-burning	V_{mn}	electronic coupling constant
NRHB	non-resonant hole-burning	ω_m	mean phonon frequency
PAH	polycyclic aromatic hydrocarbons	ZPL	zero-phonon line

Chapter 1

General Introduction

(Based in part on a book chapter: Lin, C., Feng, X., Jankowiak, R., *Low-Temperature Laser-Induced Fluorescence Studies of Various Biological Systems with Pyrene Chromophore*, in: Ruzicka, P., Kral, T. (Ed.) **Pyrene: Chemical Properties, Biochemistry Applications and Toxic Effects**, Nova Science Publishers, New York, 2013, in press.)

1.1 General Overview

It is well-known that fluorescence signals from chromophores with multiple fused aromatic rings are sensitive to the molecular structure and polarity of its microenvironment. Therefore, fluorescence spectroscopy is a powerful tool to study complex biological systems. In conventional spectroscopy, fluorescence spectra are typically collected at ambient temperature using non-resonant broad-band excitation. Excitation energy used under these conditions is usually much larger than the energy gap between ground and first excited electronic (S_1) state (i.e. chromophores are excited to S_2 or even higher states). This leads to population of all sites within the inhomogeneously broadened band, resulting in a broad emission spectrum. In addition, thermal broadening in spectra collected at room temperature will further widen the bandwidth and decrease the resolution of this spectroscopic method. Therefore, subtle changes of fluorescence spectra of complex biological systems measured by conventional spectroscopic method remain hidden beneath the broad and featureless origin band. Nevertheless, these broad spectra can still provide information about the energies of the (0,0)-transition (pure electronic transition between S_1 state and ground state), and intensity variation of the (0,0)- and vibronic

bands of chromophores induced, for example, by the polarity of microenvironment [1, 2].

One way to conquer the shortcomings of conventional fluorescence spectroscopy is to lower the temperature of the system. At 77 K (in liquid nitrogen temperature) or 5 K (in vapor of liquid helium), thermal broadening will be largely reduced. Under this condition, even broad spectra obtained at non-resonant excitation will be more informative. For example, in ref. [3], room-temperature fluorescence spectra show only ~ 2 nm red shift of origin band for immunocomplexed pyrene relative to free pyrene (Py); while at 4.2 K, fluorescence origin band of free Py was narrowed by around 50% compared to room-temperature spectrum, and a clear peak splitting could be observed for immunocomplexed Py, which was hidden by thermal broadening in fluorescence spectra collected at ambient temperature. Generally, fluorescence signals obtained at low temperature are more appropriate to determine the properties of complex systems, and have been successfully applied in conformational studies of benzo[*a*]pyrene tetrol (BPT)/DNA physical complexes [4]. In addition, low-resolution fluorescence spectra collected at cryogenic temperature are prerequisites for fluorescence line-narrowing (FLN) spectra collection, as they determine the detection range and excitation wavelengths for both the origin-band and vibronically excited fluorescence line-narrowed (FLN) spectra.

The resolution of fluorescence spectra can be further enhanced by exciting chromophores within their S_1 vibronic or (0,0)-transition bands at cryogenic temperature (~ 5 K). In this approach, so-called fluorescence line-narrowing spectroscopy (FLNS) [5-14], contributions from both thermal and solvent broadening could be largely reduced or even eliminated, resulting in highly structured fluorescence spectra providing information about ground-state and/or

excited-state vibrational energy levels. Thus, this method is used to obtain information such as interactions between chromophores and biopolymers that could not be provided by other techniques. In life sciences and environmental studies, FLNS has been applied to molecular identification and conformational studies, e.g. systems containing carcinogenic polycyclic aromatic hydrocarbons (PAHs) and their DNA-adducts and metabolites (reviews [15, 16] and references therein). In addition, this “information-rich” detection technique can be interfaced with various separation methods ([17] and references therein), for better characterization and determination of analytes in complex mixtures. Besides, this frequency-domain spectroscopic method can be used to obtain information regarding molecular dynamics and electron-phonon coupling. Therefore, FLNS has also been extensively used in photosynthesis research, e.g. in studies of chlorophyll-like molecules [18-23], bacteriochlorophylls [24, 25], and various photosynthetic complexes containing fluorescent chromophores ([26] and references therein).

In order to perform FLNS experiments, four major components are required for measurement: a spectrally narrow excitation source (a tunable pulsed laser), an optically accessible low-temperature sample chamber (i.e., a low-temperature cryostat), a dispersion device (a monochromator with different gratings), and a gated detection system [5, 6, 27-29]. In order to achieve high-quality FLN spectra, for vibronic excitation, where the vibronic modes of analytes are of interest, 0.06 nm resolution ($\sim 3\text{-}5\text{ cm}^{-1}$ in the range of 350 nm to 450 nm) is sufficient; while for excitation within the origin band, the highest available resolution (preferably about 0.5 cm^{-1}) has to be utilized to obtain reliable data for fitting and modeling studies.

In this chapter, the basic concepts and the underlying physics of NLN (non-line

narrowing) and FLN spectroscopies will be introduced. We will discuss homogeneous and inhomogeneous broadening, the zero-phonon line (ZPL) and phonon sideband (PSB), electron-phonon (el-ph) coupling strength, and the information these spectroscopic techniques provide. This is followed by a brief description of excitation energy transfer (EET), and two calculation methods (simple convolution approach and Redfield) for calculating FLN spectra. At the end of this chapter, the organization of this thesis is described.

1.2 Basic Aspects of Fluorescence Line-Narrowing (FLN) Spectroscopy

1.2.1 Homogenous and Inhomogeneous Broadening

Generally speaking, when chemically identical chromophores experience the same environment, e.g., when embedded in a perfect crystal, these chromophores absorb exactly the same energy and give a narrow Lorentzian-shaped absorption spectra, which are homogeneously broadened [30] as shown in Figure 1-1A. The full-width at half maximum (FWHM) of these spectral lines can be defined as homogeneously broadened line width, Γ_{hom} , which can be directly related to the total dephasing time (T_2) of the optical transition by

$$\frac{1}{T_2} = \pi c \Gamma_{\text{hom}} = \frac{1}{2T_1} + \frac{1}{T_2'}, \quad (1-1)$$

where c is the speed of light, T_1 is the excited-state lifetime, and T_2' is the pure dephasing time [31, 32].

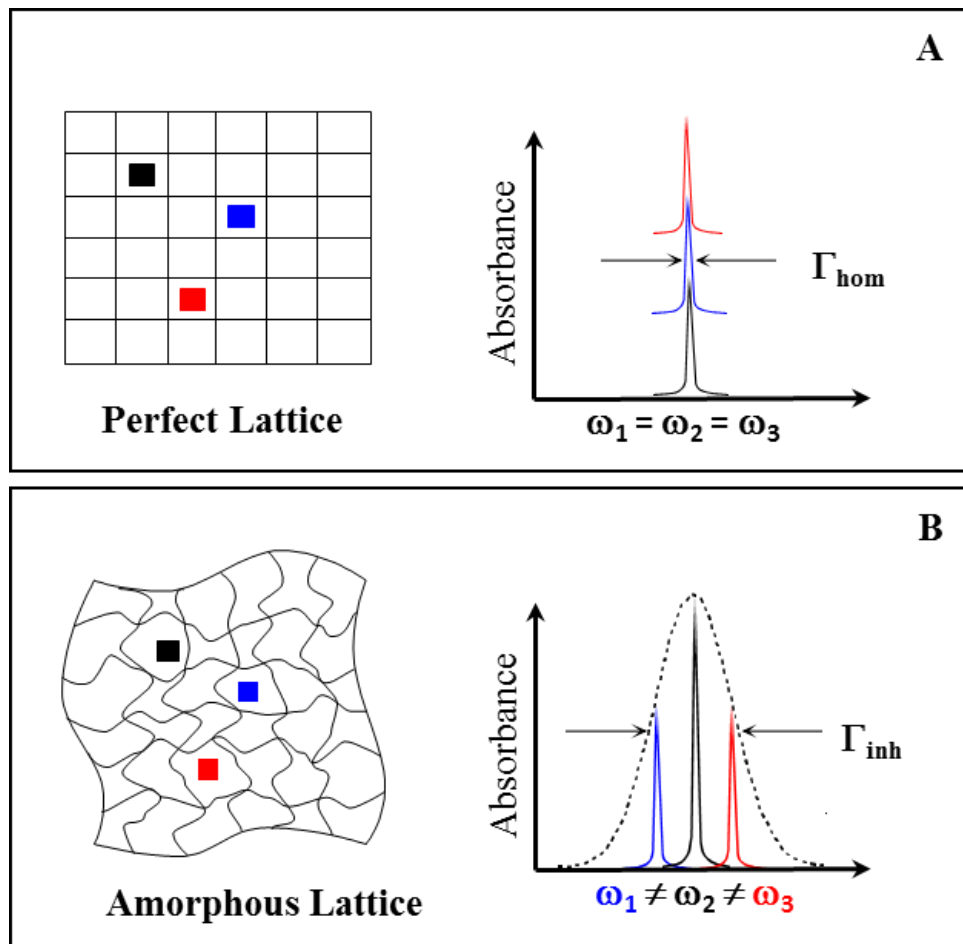


Figure 1-1. Schematic view of homogeneous and inhomogeneous broadening. Frame A: Chromophores are doped in highly ordered system (crystalline environment) and absorption lines are only homogeneously broadened. Frame B: Molecules are in a disordered matrix so the absorption is inhomogeneously broadened.

However, when the molecules are in solution or in an amorphous solid, each fluorophore's immediate microenvironment is different, resulting in modified interactions between the molecules and their surroundings. Thus, each molecule has its own well-defined absorption energy level, leading to the total absorption of all the chromophores in the system to form a broad band, referred to as an inhomogeneously broadened absorption band (Figure 1B). Its FWHM (neglecting contribution from phonons) describes the inhomogeneous broadening (Γ_{inh}) [33-35].

The total band shape reflects the property of the micro-environment of the chromophores, i.e., it describes a distribution of energetically inequivalent sites and their coupling to an environment in which fluorophores reside.

1.2.2 Zero-Phonon Lines and Phonon Sidebands

As mentioned above, the inhomogeneous broadening itself describes reasonably well the (0,0)-absorption (or fluorescence) band at low temperature (~ 5 K) only for very weak electron-phonon (el-ph) coupling strength, as the total absorption bandwidth (origin band) is described by $\Gamma_{inh} + S\omega_m$, where S is the Huang-Rhys factor (see below) and ω_m is the mean phonon frequency. Though gas-phase absorption and emission spectra contain sharp bands corresponding to transitions between different energy levels of an analyte itself, pure electronic transitions of the chromophores in solution or amorphous solid matrices are always accompanied by the lattice vibrational transitions (phonons) [36]. Theoretically, when the laser width and instrumental resolution are much smaller than Γ_{hom} , and one excites the chromophores resonantly

within its (0,0)-origin band at low temperatures (e.g., at 5 K), the resulting spectrum could look like the one shown in Figure 1-2. The sharp and narrow band with a Lorentzian line shape is called a zero-phonon line (ZPL) and corresponds to a pure electronic transition of the fluorophore with a bandwidth of Γ_{hom} [33]. However, the experimentally measured ZPL is much narrower than that shown schematically in Figure 1-2 (e.g., the width of ZPL of Py in cyclohexane is around 10^{-5} cm^{-1} without considering pure dephasing time). At the low-energy side of ZPL, there is a broad band called phonon sideband (PSB), characterizing the vibrational transitions of matrix that accompanies the electronic transition of the analytes. Its intensity, compared to the peak intensity of the ZPL, depends on the el-ph coupling strength (*vide infra*). As mentioned above, the peak of PSB provides the mean phonon frequency, ω_m .

In absorption spectra, PSB appears at higher frequency than the corresponding ZPL; the shape of the PSB is well described as a half-Gaussian and half-Lorentzian for $\omega < \omega_m$ and $\omega > \omega_m$, respectively. In emission spectra, the PSB is located at lower energies than the corresponding ZPL, i.e., its profile is reversed on the frequency scale. From the integrated intensity of the ZPL (I_{ZPL}) and the PSB (I_{PSB}), a Debye-Waller factor α can be obtained using the following formula [7, 37]:

$$\alpha = I_{\text{ZPL}} / (I_{\text{ZPL}} + I_{\text{PSB}}). \quad (1-2)$$

At low-temperature limit ($T \sim 0 \text{ K}$), the dimensionless Huang-Rhys factor is related to α by

$$S = -\ln\alpha, \quad (1-3)$$

and the width of the inhomogeneously broadened fluorescence origin band is also given by $\Gamma_{\text{inh}} + S\omega_m$. The physical meaning of Huang-Rhys factor is discussed in section 1.2.3.

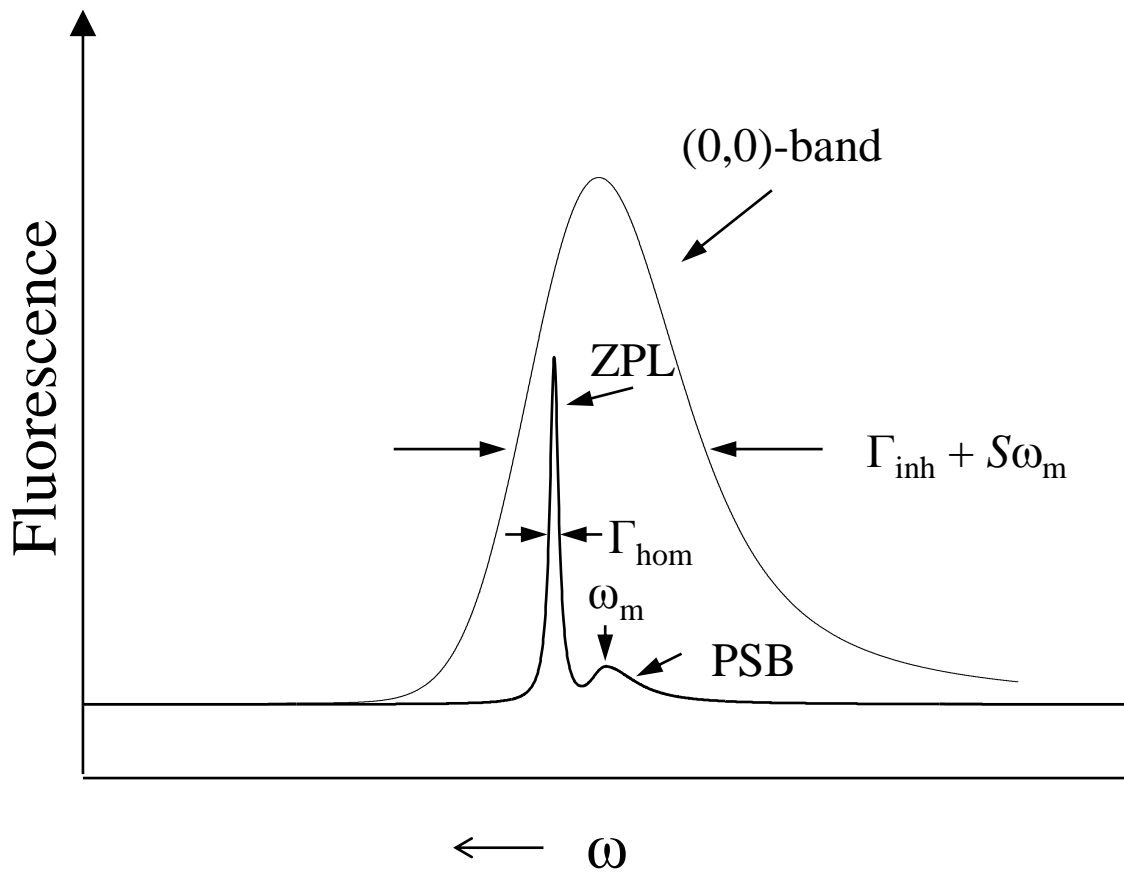


Figure 1-2. Schematic view of inhomogeneously broadened fluorescence origin band and fluorescence ZPL and PSB. The value of mean phonon frequency ω_m is the difference between the peak positions of ZPL and PSB in the unit of frequency.

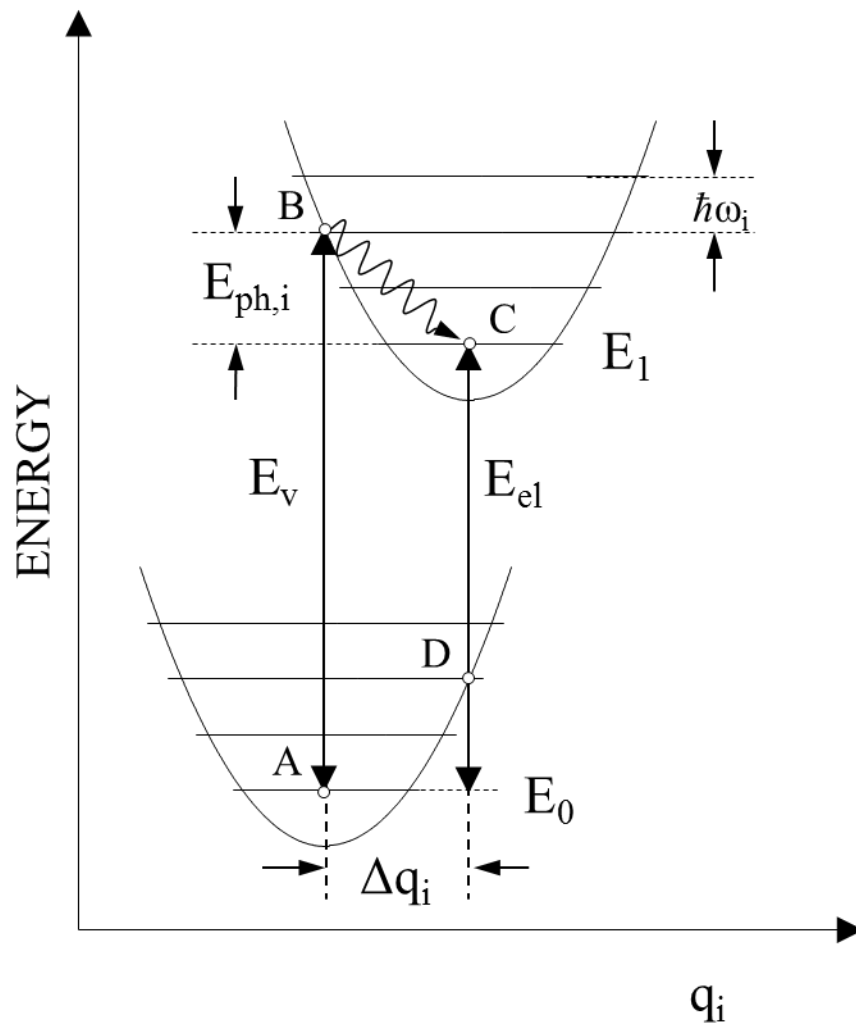


Figure 1-3. Configurational coordinate diagram for the analysis of the optical transition between the ground (E_0) and excited (E_1) states.

1.2.3 Electron-Phonon Coupling Strength

This section addresses the coupling between electronic excitation of chromophore and the external lattice vibrational transition modes. Figure 1-3 illustrates the energy levels of a hypothetical guest chromophore in a glassy matrix. The two parabolas represent the potential energy of the ground and excited electronic states (E_0 for ground state and E_1 for excited state). Except for the lowest horizontal lines in these two states, which depict the pure electronic states of the molecule, other lines stand for the energy levels of the chromophore interacting with local phonon i . Note these levels are not vibrational levels of the molecule in ground or excited states. Multiple phonon quanta (energy $\hbar\omega_i$) can be described by a harmonic oscillator model (not shown in the figure).

The potential energy can be expressed in the following general form [38]:

$$V = \sum_i A_i q_i + \sum_{ij} B_{ij} q_i q_j \quad (1-4)$$

In Eq. (1-4), A_i is the linear coupling coefficient, describing the change of excited-state energy during optical transition because of equilibrium shift of the normal oscillator. B_{ij} is the quadratic coupling coefficient; for $i = j$, it describes the change in the energy of the excited state resulting from the change in the normal oscillator frequencies during an excitation. For $i \neq j$, they describe the change in the energy due to mixing of normal coordinates [13]. Our discussion below assumes a linear electron-phonon coupling approximation, where the second term of equation (1-4) is negligible. Here, q_i stands for the lattice normal coordinate belonging to phonon mode i , and Δq_i represents the change of equilibrium position. In Figure 1-3, E_v is the vertical transition

energy, and E_{el} is the pure electronic transition energy in this process. $E_{ph,i} = E_v - E_{el}$ is the lattice vibrational transition energy involved in the vertical transition. Therefore, the strength of el-ph coupling is measured by the above-mentioned Huang-Rhys factor, S , defined as

$$S = E_{ph,i} / \hbar\omega_i. \quad (1-5)$$

In low-temperature limit, S is given by [12, 61, 65]

$$S(T=0) = \sum_i \frac{M_i \omega_i}{2\hbar} (\Delta q_i)^2, \quad (1-6)$$

where M_i and ω_i are the reduced mass and frequency of the phonon mode i , respectively. Considering equations (1-2) and (1-3) for the relationship among S , α , and the integrated intensity of ZPL and PSB, it's obvious that when the equilibrium position shift is small from ground state to excited state, S is small, resulting in a larger α value and a larger integrated area of ZPL, as shown in the upper part of Figure 1-4. Generally speaking, systems with $S < 1$ have weak el-ph coupling (upper part of Figure 1-4); $S \sim 1$ to ~ 3 is referred to an intermediate el-ph coupling, while $S > 3$ is observed in strongly coupled systems (lower part of Figure 1-4); When $S \geq 10$, the el-ph coupling is very strong for the system, and no ZPL can be observed [13].

1.2.4 Lineshape Function of FLN Spectra

Under linear Franck-Condon approximation and the case in which phonons are sufficiently delocalized, single-site fluorescence profile is described by [39, 40]:

$$F(\omega) = e^{-S} l_0(\omega - \Omega_0) + \sum_{R=1}^{\infty} S^R \frac{e^{-S}}{R!} l_R(\omega - \Omega_0 + R\omega_m). \quad (1-7)$$

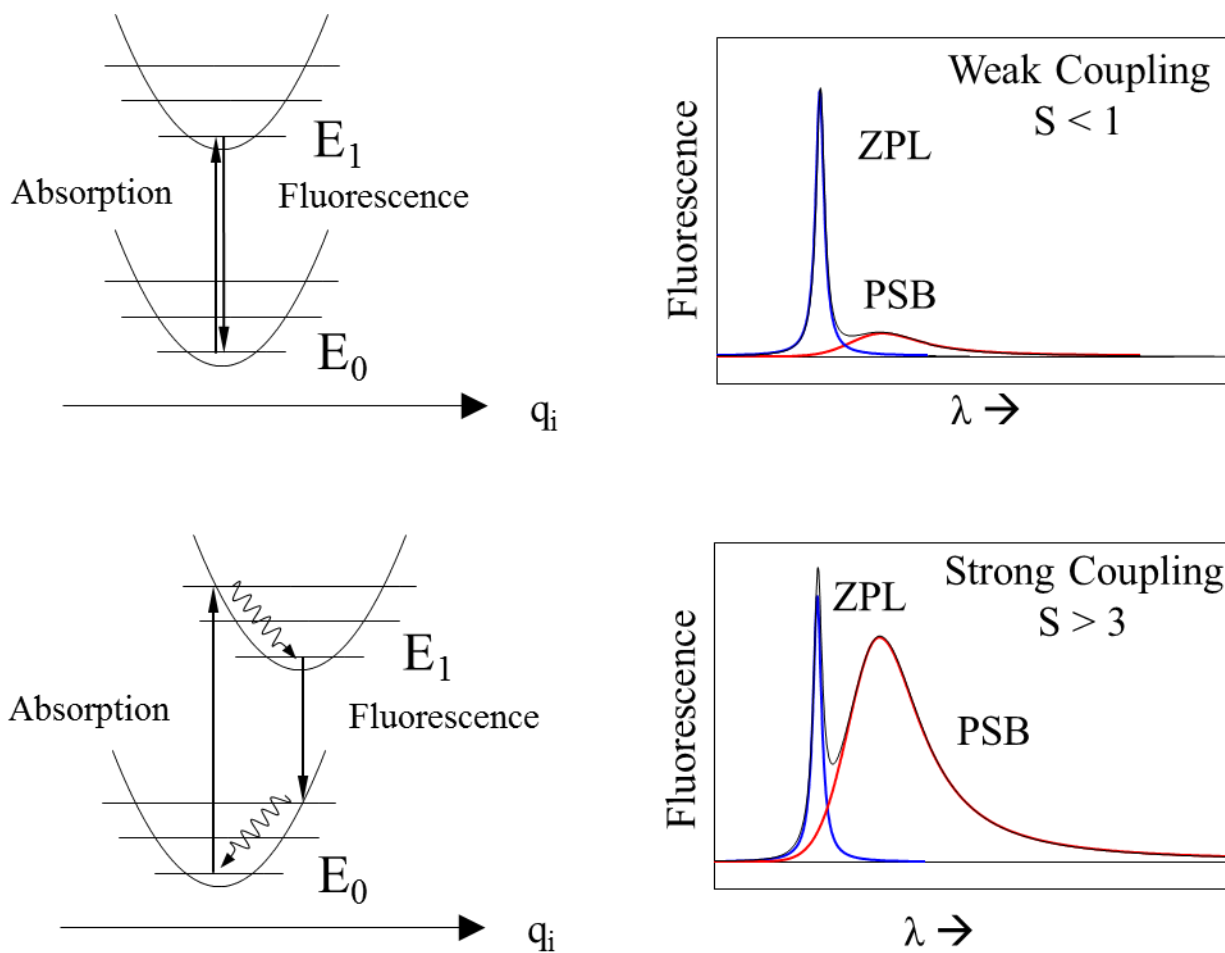


Figure 1-4. Diagram of potential curves in linear electron-phonon coupling and molecular line shapes of corresponding transitions.

In this equation, ω_m is the phonon mean frequency; $l_0(\omega - \Omega_0)$ is the Lorentzian line shape of the ZPL peaking at Ω_0 ; $l_R(\omega - \Omega_0 + R\omega_m)$ stands for the normalized line-shape function of the R -phonon transition ($R = 1, 2, \dots$) with peak position at $\Omega_0 - R\omega_m$. A Poisson weighting factor for every R determines the intensity distribution of the PSB. The profile l_R is obtained by folding l_1 with itself for R times. Single-site absorption $A(\omega)$ is symmetric to $F(\omega)$ with respect to $\omega = \Omega_0$. If $G(\omega_0)$ represents the distribution ensemble of chromophores, the resulting FLN spectrum excited at ω_{ex} can be written as [13]:

$$F(\omega, \omega_{ex}) = \int_0^{\infty} F(\omega - \omega_0) G(\omega_0) A(\omega_{ex} - \omega_0) d\omega_0. \quad (1-8)$$

1.2.5 Origin Band Excitation—Ground-State Vibrational Frequencies

When a narrow-band laser (frequency ω_L , laser linewidth $\Gamma_L \ll \Gamma_{hom}$) is used to selectively excite molecules within the inhomogeneously broadened (0,0)-absorption band in a glassy matrix at $T \sim 5$ K (origin-band excitation mode, as shown in Figure 1-5A), only a subset of chromophores, whose (0,0)-transition energy overlaps with that of the excitation laser, can be excited. A schematic of the resulting spectrum consisting of the ZPL (ω_{ZPL}) and two vibrational bands (with frequencies of ω_α and ω_β) is shown in the lower panel of Figure 1-5A. Vibrational ZPLs correspond to transitions terminating at vibrational levels of S_0 state. Thus, origin band excitation provides ground-state vibrational frequencies (ω_α and ω_β) and relative vibrational intensities, which, in combination, may serve as a fingerprint of studied chromophores.

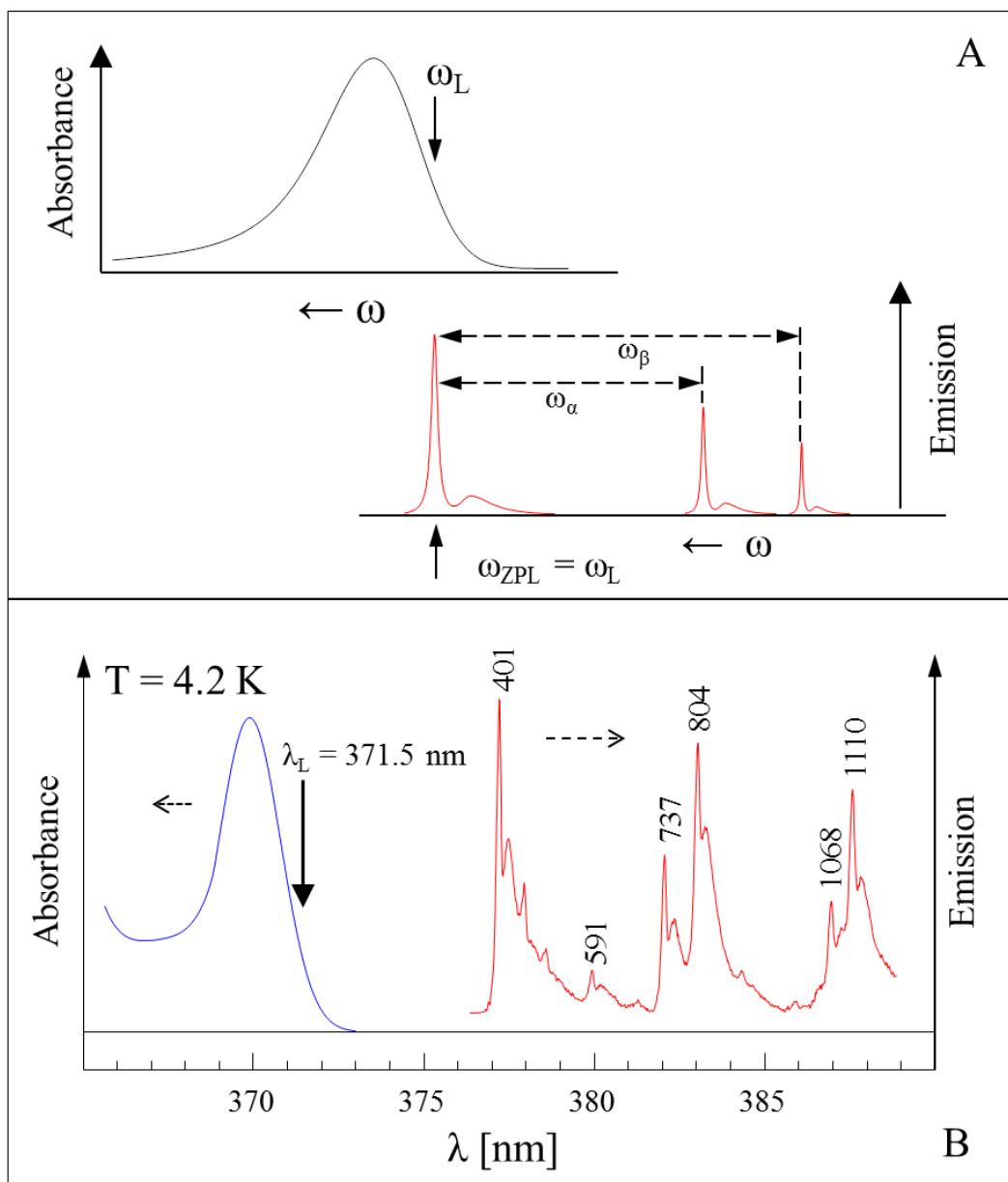


Figure 1-5. Origin band excitation in FLNS. Frame A: Laser frequency, ω_L , excites only those chromophores whose (0,0)-transitions overlap with the laser profile (see text for details). ω_α and ω_β correspond to the ground-state vibrational frequencies in cm^{-1} . Frame B: (0,0)-absorption band and FLN spectrum obtained for pyrene in ethanol glass at $T = 4.2$ K, $\lambda_{\text{ex}} = 371.5$ nm. The sharp peaks (bands) correspond to the pyrene ground-state vibrational bands. Numbers above ZPLs are vibrational frequencies in cm^{-1} determined by the difference between positions of ZPL peaks and laser excitation. Note that between 373 and 376.5 nm, data were not collected.

As an example, Figure 1-5B shows the (0,0)-absorption band (left) and the ground-state-excited FLN spectrum of pyrene in ethanol glass at $T = 4.2$ K (right). Only part of this spectrum is shown for clarity; all narrow peaks are ZPLs and the numbers above correspond to the ground-state vibrational frequencies (in cm^{-1}). Due to lattice phonon transitions coupled with electronic transitions, broad PSBs can be observed at low-energy side of ZPLs. FLN spectra with ground-state excitation can provide information of not only S_0 state vibrational modes, but also strength of el-ph coupling.

1.2.6 Vibronically Excited FLNS—Excited-State Vibrational Frequencies

Vibronic levels are vibrational levels of molecules in excited electronic states. Vibronically excited FLNS, which probes the S_1 -state vibrational levels, is more often used for identification of closely related analytes (reviews [5, 6, 15, 41] and references therein). In this approach, the laser is tuned to the vibrational levels in first excited state (S_1) of chromophores. S_1 -state vibrational dynamics, frequencies, and intensities are extremely sensitive to subtle changes in the structures of the chromophore and its environment, and this sensitivity is directly reflected in the FLN spectra obtained through this excitation mode [5, 6, 42]. Figure 1-6 illustrates how vibronically excited FLN spectroscopy probes S_1 -state vibrational-level structure. Slanted lines in the S_1 -state (upper frame) schematically indicate inhomogeneous broadening, corresponding to the broad absorption origin-band (gray curve) and vibronic bands represented by different Gaussian curves (lower frame, one color stands for one vibronic level). Due to inhomogeneity of the matrix, several vibronic bands may overlap on the energy scale. Therefore,

laser may excite a number of overlapping vibronic energy levels. Figure 1-6 shows a case where three overlapping vibronic levels are excited. After relaxation to the respective zero-point levels, these three “isochromats” reach their correlated $v = 0$ levels of S_1 state and fluoresce. Pink, blue and red lines within the origin-band come from the different (0,0)-transitions, and the difference between these ZPLs and laser excitation frequency gives excited-state vibrational frequencies at ω_a , ω_b , and ω_c . Furthermore, transitions also happen between $v = 0$ level in S_1 state and vibrational levels in ground state, resulting in weaker vibronic lines, providing information about vibrational levels on the ground-state vibrational frequencies (ω'_a , ω'_b , and ω'_c). Of course the multiplet of ZPLs observed within the fluorescence origin band depends not only on excitation wavelengths but also on the absorption cross section of the vibronic transitions. In actual experiments, typically several ZPLs are observed that contribute to the multiplet origin structure for each excitation frequency, providing many “fingerprints” of studied molecules. Since the pattern of ZPLs varies from molecule to molecule, this spectroscopic method can be used for chemical identification, conformational analysis, and/or probing the microenvironment of DNA (or protein) adducts ([5, 6] and references therein).

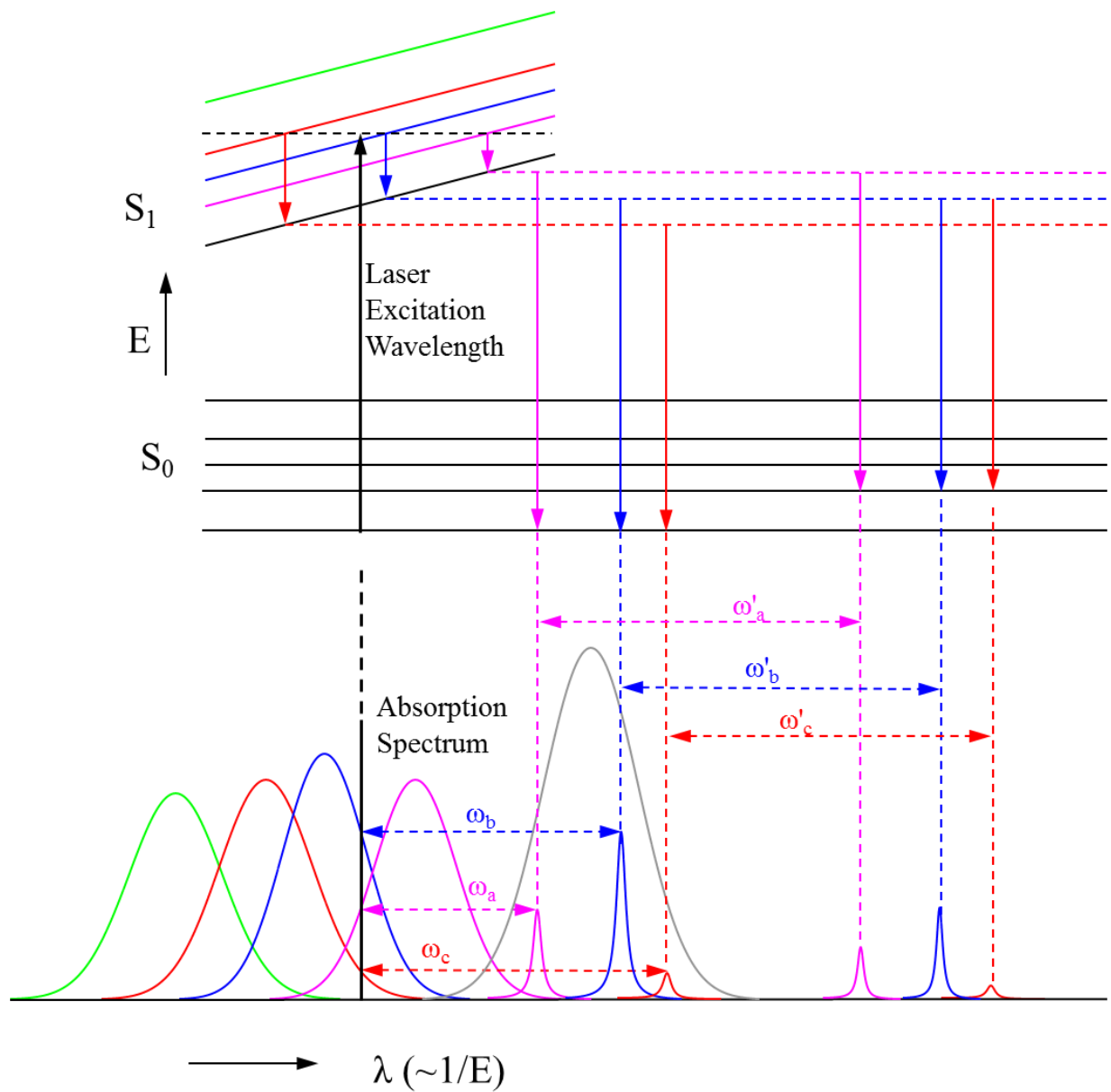


Figure 1-6. Jablonski diagram of FLNS and absorption cross section of vibronic transition and resulting FLN spectrum. Gray line: (0,0)-transition. El-ph coupling is neglected in this graph. Details are discussed in text.

1.2.7 Delta Fluorescence Line-Narrowing Spectroscopy (Δ FLNS)

As a combination of spectral hole-burning (HB) and FLNS, Δ FLNS measures the difference between preburn and postburn FLN spectra [43-46], i.e., two consecutive FLN measurements are separated by a certain period of exposure to the laser excitation, allowing for partial HB. Δ FLN spectrum is then obtained by subtracting the latter FLN spectrum from the initial FLN measurement. This method can be used to better resolve the ZPLs and minimize contributions from molecules that absorb via their broad PSB. Δ FLN spectroscopy has been successfully applied to investigate the el-ph coupling strength in various photosynthetic complexes [23, 47-52].

1.3 Excitation Energy Transfer (EET) and Modeling Study

1.3.1 EET and Coupling Constant

When multiple chromophores are spatially close enough to each other and their dipole moments are properly oriented, the interaction (characterized by coupling constant V) among these chromophores make excitation energy transfer (EET) possible among the pigments, which is the case for antenna systems in photosynthetic complexes. Figure 1-7 shows the most simplified case where two chromophores are excitonically coupled. Notice that top right of Figure 1-7 describes the process of electron transfer, which is observed in reaction centers of various photosynthetic systems (see review [26] and references therein).

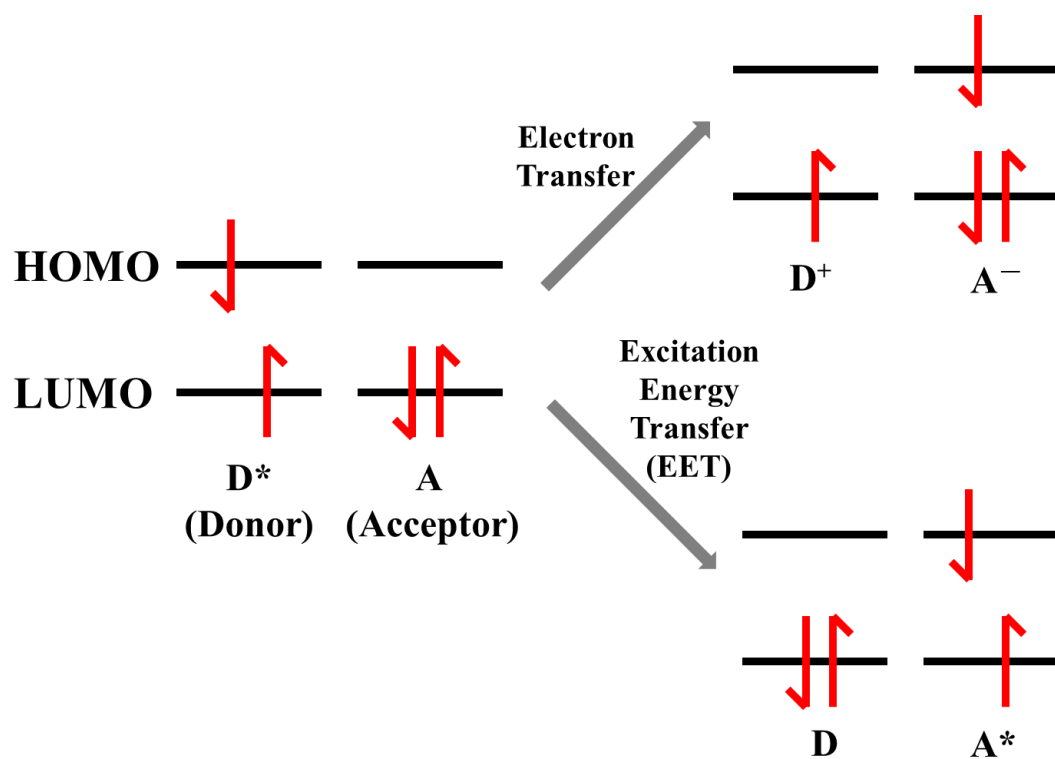


Figure 1-7 Schematic of the electronic coupling between the two pigments donor (D) and acceptor (A), giving rise to either electron transfer (top right) or EET (bottom right) from D* to A. Star indicates excited state, while + and - indicate the charge of pigments.

Electronic coupling constant can be calculated in various ways. When pigments are spatially far apart, and the coupling is assumed to be dominated by the Coulomb interaction, V is calculated using the point-dipole approximation (PDA) [53-55]. The approximation is known to break down for shorter distances between the interacted chromophores [55-58]. Renger *et al.* developed a method called transition charges from electrostatic potentials (TrEsp) for coupling constant determination [53, 55]:

$$V_{mm} = \frac{f}{4\pi\epsilon_0} \sum_{i,j} \frac{q_i^T \cdot q_j^T}{|\mathbf{R}_m^i - \mathbf{R}_m^j|}, \quad (1-9)$$

where f and ϵ_0 are screening factor and electric constant, respectively. q_i^T is the atomic transition charges on pigment i , while \mathbf{R}_m^i denotes the coordinates of the i^{th} atom of chromophore m in the system.

Depending on the extent of electronic coupling (V) between donor and acceptor, EET mechanism can be divided into two categories – incoherent and coherent [59, 60]. For weak coupling, $V/E_\lambda < 1$ (E_λ is the reorganization energy, which is discussed in section 1.3.3), the EET is considered as an incoherent hopping process between the localized donor and acceptor. For the strong coupling, $V/E_\lambda > 1$, the initial excited state is delocalized and the process is considered as a wave-like coherent process [61].

1.3.2 Convolution Method

Under static lattice approximation, calculation for the excitonic states is carried out using Frenkel Hamiltonian [62]:

$$H = \sum_n (\varepsilon_n + d_n) |n\rangle\langle n| + \sum_{n \neq m} V_{nm} |n\rangle\langle m|. \quad (1-10)$$

In this equation, $|n\rangle$ and $|m\rangle$ denote the localized monomer states, and n and m refer to n^{th} and m^{th} pigment, respectively. ε_n is the average transition energy of n^{th} monomer, while d_n stands for the offset energy due to diagonal site excitation energy disorder. The Hamiltonian is described by symmetrical matrix H of $n \times n$ dimension with the site energies in diagonal elements and the coupling V_{nm} in off diagonal elements. Recall that in section 1.2.1, the transition frequency of chemically identical pigments is shifted by inequivalent microenvironment, resulting in a Gaussian distribution of transition energies called inhomogeneous distribution function (IDF) or site distribution function (SDF). This random disorder is taken care of by Monte Carlo simulation—for one cycle, a random set of feasible sites of all pigments is selected, and this is treated by the Hamiltonian given eq. (1-10). After diagonalization the matrix, the excitonic energy (E_α) and wavefunction $|\alpha\rangle$ can be obtained as

$$|\alpha\rangle = \sum_n c_n^{(\alpha)} |n\rangle, \quad (1-11)$$

$|c_n^{(\alpha)}|^2$ provides the probability that chromophore n contributes to the α^{th} excitonic state, so $\sum_n |c_n^{(\alpha)}|^2 = 1$. Excitonic transition dipoles are calculated by:

$$\vec{\mu}_\alpha = \sum_n c_n^{(\alpha)} \vec{\mu}_n, \quad (1-12),$$

where $\vec{\mu}_n$ is the transition dipole of monomer pigment n . The absorption spectrum of the α^{th} exciton state, neglecting the phonons and intramolecular vibrations, is given by:

$$d_\alpha(\omega) = \left\langle |\vec{\mu}_\alpha|^2 \delta(\omega - \omega_{\alpha 0}) \right\rangle_{\text{dis}}. \quad (1-13)$$

In Eq. 1-13, $\omega_{\alpha 0}$ is the energy of the α^{th} exciton state and $\langle \dots \rangle_{\text{dis}}$ denotes an average over disorder in site energies [62]. Net absorption spectrum is given as the sum over the absorption

for all excitonic states after convolution with the appropriate single-site absorption spectra, while fluorescence spectrum is obtained by convoluting single-site emission spectrum with only the lowest excitonic state ($d_1(\omega)$). Contribution of a single pigment to the total SDF can be expressed as [62]:

$$f_n(\omega) = \left\langle \sum_{\alpha} |c_n^{(\alpha)}|^2 \delta(\omega - \omega_{\alpha 0}) \right\rangle_{\text{dis}} . \quad (1-14)$$

1.3.3 Redfield Theory

Figure 1-7 (*vide supra*) showed schematically the EET process within a weakly coupled dimers. The same exciton “hopping” could be extended to multi-chromophore system, as shown in Figure 1-8 on the left, where the excited states are localized on each pigment. However, when coupling constants are large enough, excitonic states are delocalized, as shown in Figure 1-8 on the right. In this case, when a higher excitonic state is occupied, relaxation to a lower state can occur by exchanging energy with the “bath”, and this coupling to the bath is represented by a spectral density $J(\omega)$, which describes the coupling of the electronic transition to matrix vibrations. $J(\omega)$ (in units of angular frequency) can be expressed mathematically as [7]

$$J(\omega) = \sum_i \frac{M_i \omega_i}{2\hbar} (\Delta q_i)^2 \delta(\omega - \omega_i), \quad (1-15)$$

In this equation, M_i , ω_i , and q_i denote the reduced mass, frequency, and the shift in minimum of the excited state potential energy surfaces relative to the ground state of bath mode i , respectively.

$J(\omega)$ is often referred to as one-phonon profile that is scaled by the Huang-Rhys factor.

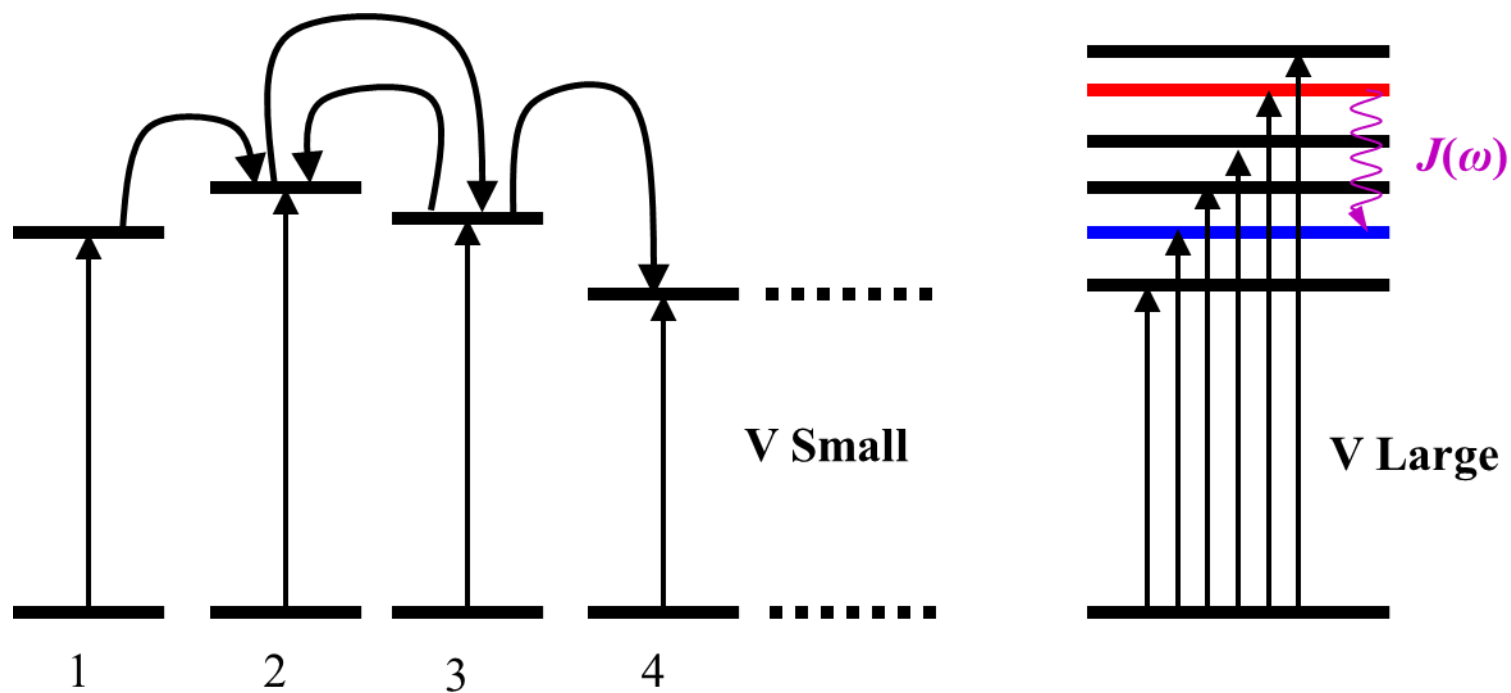


Figure 1-8. Schematic view of systems with weakly (left) and strongly (right) coupled chromophores.

At $T = 0$ K, the Huang-Rhys factor (S)

$$S = \int_0^\infty J(\omega) d\omega = \sum_i \frac{M_i \omega_i}{2\hbar} (\Delta q_i)^2, \quad (1-16)$$

which is the same as Eq. (1-6). At the same time, reorganization energy E_λ is defined as

$$E_\lambda = \int_0^\infty d\omega \hbar \omega J(\omega), \quad (1-17)$$

The value of reorganization energy plays an important role in electronic dynamics [63]. Generally speaking, Redfield theory describes relaxation rates of a multi-level system coupled to a large manifold of harmonic or effective harmonic oscillators [60, 64, 65]. This theory more accurately reflects the influence of electron-phonon coupling and energy-transfer lifetime broadening on calculated spectra than convolution method. In section 1.3.2, transition line shapes are obtained by convoluting the calculated pure electronic spectrum with an assumed (or experimentally determined) single-site absorption (or emission) spectrum in convolution method [62]; while within the scope of the Redfield theory, the system is treated with a reduced statistical density operator

$$\hat{\rho}(t) = \sum_{\mu\nu} \rho_{\mu\nu}(t) |\mu\rangle \langle \nu|. \quad (1-18)$$

For excitonic states μ and ν , the equations of motion for the exciton density matrix $\rho_{\mu\nu}(t)$ are given in terms of the correlation function $C(t)$ of the optical energy gap of the pigments (see ref. [63] for details). $C(t)$ can be expressed in terms of the spectral density $J(\omega)$:

$$C(t) = \int_0^\infty d\omega \omega^2 \{ [1 + n(\omega)] J(\omega) e^{-i\omega t} + n(\omega) J(\omega) e^{i\omega t} \}, \quad (1-19)$$

where

$$n(\omega) = \frac{1}{e^{\hbar\omega/kT} - 1} \quad (1-20)$$

is the mean number of vibrational quanta for an oscillator of frequency ω in thermal equilibrium.

(Details of the Redfield theory can be found in references [60, 63-65].)

1.4 Organization of Thesis

In chapter two, low-temperature laser-induced fluorescence spectroscopy is used to investigate the mechanism of enhanced reactivity of base paired guanine of endogenous 5-methylcytosine towards carcinogenic diolepoxide metabolites of polycyclic aromatic hydrocarbons (PAH) present in cigarette smoke. Because of the fast hydrolysis process of diolepoxide of interest (benzo[*a*]pyrene diolepoxide, BPDE), its hydrolyzed product (i.e., BPT) is used as a model molecule to study the effects of various substituents on cytosine (C-5) on the formation of physical complexes on CG base pairs. We show that enhanced π - π interaction introduced by the methyl group of cytosine facilitate the formation of intercalative BPT/DNA complexes. We argue that the same trend should be observed in BPDE/DNA complexes, that is, the enhanced π - π interaction should place BPDE in a favourable orientation for nucleophilic attack by the N^2 position of guanine.

In the third chapter, spectroscopic and modeling data are presented for the “blue conformation” of Py in several monoclonal antibodies (mAbs, including 4D5 mAb). We show that π -cation plays an important role in ligand binding and stabilization. We propose that a considerable narrowing of the fluorescence origin band of ligand in the protein environment might be regarded as a simple indicator of π -cation interactions for haptens in mAb binding pocket.

In chapter four, different line shapes of FLN and Δ FLN spectra obtained for pyrene (Py) in ethanol glass is observed at various excitation wavelengths using time-resolved fluorescence measurements, suggesting (in agreement with ref. [66]) that Δ FLN spectra obtained in the low fluence limit can be described by the single-site fluorescence line shape function. A peculiar

dependence of the Huang-Rhys factor (S) on excitation wavelength was discovered, and discussed in terms of the solute-solvent, intermolecular Lennard-Jones potential. A V-shaped frequency dependence of the S -factor, also observed earlier for chlorin-doped 1-propanol glass [50] suggests that the repulsive-dispersive potential proposed by Renge *et al.* [67] is not sufficient to account for a complex “color effect”. At the high frequency edge the electron-phonon coupling is strongly enhanced by electrostatic interactions.

Chapter five describes simple “analytical” expressions to calculate the absorption, emission, and FLN spectra for weakly coupled dimers with EET present. This theory can be easily extended to multiple chromophores. Theoretical calculations (assuming low fluence and weak coupling limit) show that the spectra calculated for various dimers using our analytical expressions are in good agreement with spectra calculated by the simple convolution method and the more rigorous treatment from the Redfield theory, as long as the bulk absorption spectra are made to match for all approaches. The analytical expressions clearly reveal the presence or absence of EET in FLN spectra. We argue that our simple approach can model very complex systems in a relatively short time providing very smooth spectra. This method has been applied to FLN spectra obtained for CP47 antenna complex [68], which indicated the presence of uncorrelated EET between pigments contributing to the nearly degenerated two low-energy absorption bands. Calculated FLN spectra show a good agreement with experimental results.

References

- [1] Nakajima, A., *B. Chem. Soc. JPN* 1971, 44, 3272-3227.
- [2] Kalyanasundaram, K., Thomas, J. K., *J. Am. Chem. Soc.* 1977, 99, 2039-2044.
- [3] Grubor, N. M., Hayes, J., Small, G. J., Jankowiak, R., *Natl. Acad. Sci. USA*. 2005, 102,

7453-7458.

- [4] Jankowiak, R., Lu, P. Q., Small, G. J., Geacintov, N. E., *Chem. Res. Toxicol.* 1990, 3, 39-46.
- [5] Jankowiak, R., Small, G. J., *Anal. Chem.* 1989, 61, 1023 A -1032A.
- [6] Jankowiak, R., Small, G. J., *Chem. Res. Toxicol.* 1991, 4, 256-269.
- [7] Personov, R. I., in: Agranovich, V. M., Hochstrasser, R. M. (Ed.), *Spectroscopy and Excitation Dynamic of Condensed Molecular Systems*, North-Holland, Amsterdam 1983, pp. 555-619.
- [8] Hofstrat, J. W., Gooijer, C., Velthorst, N. H., in: Schulman, S. G. (Ed.), *Molecular Luminescence Spectroscopy: Methods and Applications*, John Wiley and Sons, New York 1988, pp. 383-459.
- [9] Fidy, J., Vanderkooi, J. M., in: Douglas, R. H., Moan, J., Ronto, G. (Ed.), *Light in Biology and Medicine*, Plenum Press, New York 1991, pp. 367-374.
- [10] Weber, M. J., *J. Lum.* 1987, 36, R3-R4.
- [11] Price, B. B., Wright, J. C., *Anal. Chem.* 1990, 62, 1989-1994.
- [12] Riesen, H., *Commet. Inorg. Chem.* 1993, 14, 323-347.
- [13] Jankowiak, R., in: Gooijer, C., Ariese, F., Hofstraat, J. W. (Ed.), *Shpol'skii Spectroscopy and Other Site-Selection Methods*, John Wiley and Sons, Inc., New York 2000, pp. 235-271.
- [14] Ariese, F., Jankowiak, R., in: Gooijer, C., Ariese, F., Hofstraat, J. W. (Ed.), *Shpol'skii Spectroscopy and Other Site-Selection Methods*, John Wiley and Sons, Inc., New York 2000, pp. 333-362.
- [15] Jankowiak, R., Rogan, E. G., Cavalieri, E. L., *J. Phys. Chem. B* 2004, 108, 10266-10283.
- [16] Ariese, F., Bader, A. N., Gooijer, C., *TRAC-Trend. Anal. Chem.* 2008, 27, 127-138.
- [17] Roberts, K. P., Jankowiak, R., Small, G. J., *Anal. Chem.* 2001, 73, 951-956.
- [18] Telfer, A., Pascal, A. A., Bordes, L., Barber, J., Robert, B., *J. Phys. Chem. B* 2010, 114, 2255-2260.

- [19] Rebane, K. K., Avarmaa, R. A., *Chem. Phys.* 1982, 68, 191-200.
- [20] Avarmaa, R., Jaaniso, R., Muring, K., Renge, I., Tamkivi, R., *Mol. Phys.* 1986, 57, 605-621.
- [21] Pascal, A., Peterman, E., Gradinaru, C., van Amerongen, H., van Grondelle, R., Robert, B., *J. Phys. Chem. B* 2000, 104, 9317-9321.
- [22] Renge, I., Muring, K., Sarv, P., Avarmaa, R., *J. Phys. Chem. US.* 1986, 90, 6611-6616.
- [23] Raetsep, M., Linnanto, J., Freiberg, A., *J. Chem. Phys.* 2009, 130.
- [24] Raetsep, M., Cai, Z.-L., Reimers, J. R., Freiberg, A., *J. Chem. Phys.* 2011, 134, 024506-024506.
- [25] Wendling, M., Pullerits, T., Przyjalowski, M. A., Vulto, S. I. E., Aartsma, T. J., van Grondelle, R., van Amerongen, H., *J. Phys. Chem. B* 2000, 104, 5825-5831.
- [26] Jankowiak, R., Reppert, M., Zazubovich, V., Pieper, J., Reinot, T., *Chem. Rev.* 2011, 111, 4546-4598.
- [27] Selzer, P. M., in: Yen, W. M., Selzer, P. M. (Eds.), *Topics in Applied Physics*, Springer Verlag, New York, Heidelberg, Berlin 1986, p. 113.
- [28] Jankowiak, R., Small, G. J., in: Neilson, A. H. (Ed.), *the Handbook of Environmental Chemistry: PAHs and Related Compounds*, Springer-Verlag, Berlin, Heidelberg, New York 1998, pp. 119-145.
- [29] Abram, I., Auerbach, R. A., Birge, R. R., Kohler, B. E., Stevenso.Jm, *J. Chem. Phys.* 1974, 61, 3857-3858.
- [30] Friedrich, J., Haarer, D., *Angew. Chem. Int. Edit.* 1984, 23, 113-140.
- [31] Jankowiak, R., Hayes, J. M., Small, G. J., *Chem. Rev.* 1993, 93, 1471-1502.
- [32] Moerner, W. E., *Topics in Current Physics. Persistent Spectral Hole Burning: Science and Applications.*, Springer-Verlag, New York 1988.
- [33] Rebane, K. K., *Impurity Spectra of Solids*, Plenum, New York 1970.
- [34] Völker, S., in: Fünfschilling, J. (Ed.), *Relaxation Processes in Molecular Excited States*, Kluwer Academic Publishers, Dordrecht 1989, p. 113.

- [35] Stoneham, A. M., *Rev. Mod. Phys.* 1969, *41*, 82-108.
- [36] Skinner, J. L., Moerner, W. E., *J. Phys. Chem. US.* 1996, *100*.
- [37] Osadko, I. S., in: Dusek, K. (Ed.), *Advances in Polymer Science*, Springer-Verlag, Berlin 1994, p. 123.
- [38] Sapozhnikov, M. N., Sapozhnikov, *Phys. Status. Solidi. B. Basic Research* 1976, *75*, 11-51.
- [39] Hayes, J. M., Gillie, J. K., Tang, D., Small, G. J., *Biochim. Biophys. Acta.* 1988, *932*, 287-305.
- [40] Hayes, J. M., Lyle, P. A., Small, G. J., *J. Phys. Chem. US.* 1994, *98*, 7337-7341.
- [41] Jankowiak, R., Roberts, K. P., Small, G. J., *Electrophoresis* 2000, *21*, 1251-1266.
- [42] Dushinsky, F., *Acta Physiochem.* 1937, 551-557.
- [43] Bogner, U., Schwarz, R., *Phys. Rev. B* 1981, *24*.
- [44] Yaaniso, R. V., *Proc. Acad. Sci. Estonian SSR Phys. Math.* 1985, *34*, 277-283.
- [45] Yaaniso, R. V., *J. Appl. Spectrosc.* 1986, *44*, 365-370.
- [46] Fünfschilling, J., Glatz, D., Zschokkegranacher, I., *J. Lum.* 1986, *36*, 85-92.
- [47] R äsep, M., Freiberg, A., *Chem. Phys. Lett.* 2003, *377*, 371-376.
- [48] Timpmann, K., R äsep, M., Hunter, C. N., Freiberg, A., *J. Phys. Chem. B.* 2004, *108*, 10581-10588.
- [49] Freiberg, A., R äsep, M., Timpmann, K., Trinkunas, G., *Chem. Phys.* 2009, *357*, 102-112.
- [50] R äsep, M., Pajusalu, M., Freiberg, A., *Chem. Phys. Lett.* 2009, *479*, 140-143.
- [51] R äsep, M., Pieper, J., Irrgang, K.-D., Freiberg, A., *J. Phys. Chem. B.* 2008, *112*, 110-118.
- [52] R äsep, M., Freiberg, A., *J. Lum.* 2007, *127*, 251-259.
- [53] Renger, T., *Photosynth. Res.* 2009, *102*, 471-485.
- [54] Krueger, B. P., Scholes, G. D., Fleming, G. R., *J. Phys. Chem. B* 1998, *102*, 5378-5386.
- [55] Madjet, M. E., Abdurahman, A., Renger, T., *J. Phys. Chem. B* 2006, *110*, 17268-17281.
- [56] Howard, I. A., Zutterman, F., Deroover, G., Lamoen, D., Van Alsenoy, C., *J. Phys. Chem. B*

- 2004, *108*, 19155-19162.
- [57] Linnanto, J., Korppi-Tommopä, J. E. I., Helenius, V. M., *J. Phys. Chem. B* 1999, *103*, 8739-8750.
- [58] Beljonne, D., Curutchet, C., Scholes, G. D., Silbey, R. J., *J. Phys. Chem. B* 2009, *113*, 6583-6599.
- [59] Rahman, T. S., Knox, R. S., Kenkre, V. M., *Chem. Phys.* 1979, *44*, 197-211.
- [60] Kühn, O., Renger, T., May, V., Voigt, J., Pullerits, T., Sundström, V., *Trends Photochem. Photobiol.* 1997, *4*, 213-256.
- [61] Sundström, V., Pullerits, T., van Grondelle, R., *J. Phys. Chem. B* 1999, *103*, 2327-2346.
- [62] Reppert, M., Acharya, K., Neupane, B., Jankowiak, R., *J. Phys. Chem. B* 2010, *114*, 11884-11898.
- [63] Renger, T., Marcus, R. A., *J. Chem. Phys.* 2002, *116*, 9997-10019.
- [64] Blum, K., *Density Matrix Theory and Application*, Plenum, New York 1981.
- [65] May, V., Kühn, O., *Charge and Energy Transfer Dynamics in Molecular Systems: A Theoretical Introduction*, Wiley-VCH, Berlin 2000.
- [66] Reppert, M., Naibo, V., Jankowiak, R., *J. Chem. Phys.* 2010, *133*, 014506.
- [67] Renge, I., Rätsep, M., Freiberg, A., *J. Lum.* 2011, *131*, 262-265.
- [68] Neupane, B., Dang, N. C., Acharya, K., Reppert, M., Zazubovich, V., Picorel, R., Seibert, M., Jankowiak, R., *J. Am. Chem. Soc.* 2010, *132*, 4214-4229.

Chapter 2

Influence of C-5 Substituted Cytosine and Related Nucleoside Analogs on the Conformation of Benzo[*a*]pyrene Tetrol (BPT)/DNA Complex: Spectroscopic Study

This chapter discusses a spectroscopic component of the manuscript entitled: “**Influence of C-5 Substituted Cytosine and Related Nucleoside Analogs on the Formation of Benzo[*a*]pyrene Diol Epoxide-dG Adducts at CG Base Pairs of DNA**” and published in *Nucleic Acids Research*, 2011, 39, 3988-4006 by

Rebecca Guza, Delshanee Kotandeniya, Kristopher Murphy, Thakshila Dissanayake, George Madalin Giambasu, Rahul R. Lad, Filip Wojciechowski, Shantu Amin, Shana J. Sturla, Robert H.E. Hudson, Darrin M. York, Chen Lin, Ryszard Jankowiak, Roger Jones, and Natalia Y. Tretyakova

Abstract

Endogenous 5-methylcytosine (^{Me}C) residues are found at all CG dinucleotides of the *p53* tumor suppressor gene, including the mutational “hotspots” for smoking induced lung cancer. ^{Me}C enhances the reactivity of its base paired guanine towards carcinogenic diolepoxide metabolites of polycyclic aromatic hydrocarbons (PAH) present in cigarette smoke. In the present study, the structural basis for these effects was investigated using a series of unnatural nucleoside analogs and a representative PAH diolepoxide, benzo[*a*]pyrene diolepoxide (BPDE) using low temperature laser-based fluorescence spectroscopy. Spectroscopic study shows that BPT assumes both quasi-external and intercalated geometries in its complexes with DNA, and a greater contribution of intercalated structures is observed in the presence of ^{Me}C and dPER as compared to unmodified duplex. A similar trend is expected for DNA complexes with BPDE. This is in agreement with molecular docking studies which revealed that 5-alkylcytosines and unnatural nucleobase analogs with extended aromatic systems facilitate the formation of intercalative BPDE-DNA complexes, placing BPDE in a favourable orientation for nucleophilic attack by the *N*² position of guanine.

List of Abbreviations

(±)-*anti*-BPDE, (±)-*anti*-benzo[*a*]pyrene-*r*-7,*t*-8-dihydrodiol-*t*-9,10-epoxide; (-)-*anti*-BPDE, (-)-*anti*-benzo[*a*]pyrene-*s*-7,*t*-8-dihydrodiol-*t*-9,10-epoxide; B[*a*]P, benzo[*a*]pyrene; (+)-BP-diol, (+)-benzo[*a*]pyrene-7*S*-*trans*-7,8-dihydrodiol; BP78D, benzo[*a*]pyrene-7*S*-*trans*-7,8-dihydrodiol; BPDE, benzo[*a*]pyrene diol epoxide; BP78D, benzo[*a*]pyrene-7*S*-*trans*-7,8-dihydrodiol; BPT, benzo[*a*]pyrene-*r*-7,*t*-8,9,10-tetrahydroetraol; Br-C, 5-bromocytosine; Cl-C, 5-chlorocytosine; Dft, 2,4- difluorotoluene; dPER, perimidine-2-one deoxyribonucleoside; Et-C, 5-ethylcytosine; F-C, 5-fluorocytosine; I-C, 5-iodocytosine; ^{Me}C, 5-methyl-cytosine; *N*²-BPDE-dG, 7,8,9-trihydroxy-10-(*N*²-deoxyguanosyl)-7,8,9,10-tetrahydrobenzo[*a*]pyrene; PAHs, polycyclic aromatic hydrocarbons; Pr-C, 5-propynylcytosine; pyrrolo-C, 5-pyrrolocytosine.

2.1 Introduction

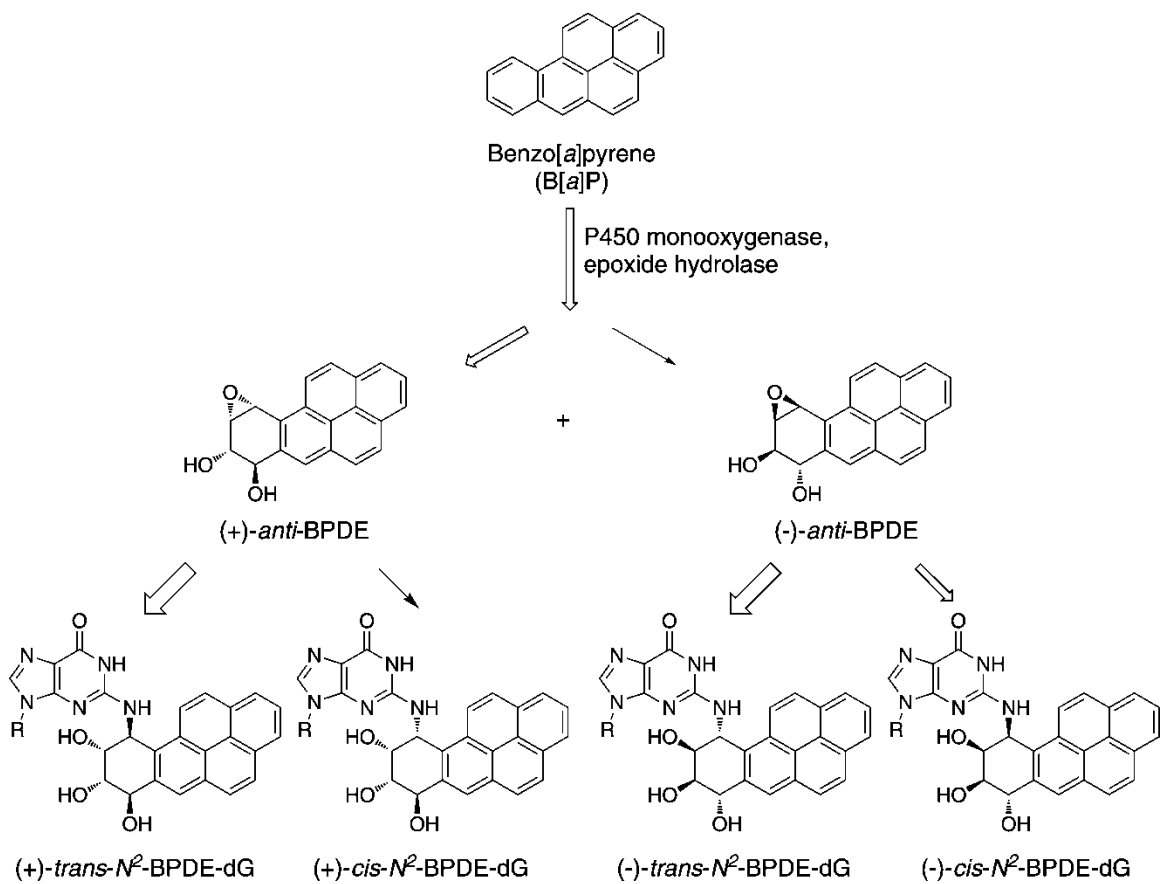
Benzo[*a*]pyrene (B[*a*]P, Scheme 2-1) is the best known representative of polycyclic aromatic hydrocarbons (PAH) produced from incomplete combustion of organic material. B[*a*]P and other PAHs are ubiquitously present in cigarette smoke, urban air, and cooked food. Studies in animal models have shown that B[*a*]P is a potent systemic and local carcinogen that induces skin, stomach, and lung tumors, and is considered a likely causative agent for smoking-induced cancer [1, 2]. Metabolic activation of B[*a*]P by cytochrome P450 monooxygenases produces DNA-reactive “bay region” diol epoxides, e.g. (+)-*anti*-benzo[*a*]pyrene-*r*-7,*t*-8-dihydrodiol-*t*-9,10-epoxide ((+)-*anti*-BPDE) and (-)-*anti*-benzo[*a*]pyrene-*s*-7,*t*-8-dihydrodiol-*t*-9,10-epoxide ((-)-*anti*-BPDE) (Scheme 2-1) which are considered the ultimate carcinogenic species of B[*a*]P [3-5].

Spectroscopic studies have shown that BPDE forms physical complexes with DNA, which precede their chemical reactions with DNA. Both major groove binding and intercalative BPDE-DNA binding motifs have been identified [6]. In the intercalative complex, the pyrene ring system of BPDE is "sandwiched" between two adjacent base pairs of DNA, leading to a red shift of the absorption maximum of BPDE from 343 nm to 353-354 nm [7]. Importantly, intercalative BPDE-DNA complexes facilitate the nucleophilic attack by the exocyclic amino group of guanine at the C-10 epoxide position of BPDE and catalyze the 9,10-epoxide ring opening [8, 9]. *Trans* addition of guanine to the C-10 position of (+) and (-)-*anti*-BPDE produces (+)-*trans*-*N*²-BPDE-dG and (-)-*trans*-*N*²-BPDE-dG, while *cis* addition results in (+) and (-)-*cis*-*N*²-BPDE-dG isomers (Scheme 2-1). While *trans*-*N*²-BPDE-dG adducts are the most common diastereomers *in vivo* [10], the *cis* adducts are preferentially generated under high salt conditions [11, 12]. *Cis* and *trans* *N*²-BPDE-dG have distinct conformations in DNA, which

influences their recognition by DNA repair proteins [13, 14]. The BPDE moiety of the *trans* adducts is typically found in an external minor groove conformation, with B-DNA helix undergoing minimal distortion [15, 16]. In contrast, the *cis* adducts assume intercalative conformation by displacing the modified guanine residue and its partner cytosine into the major groove (the (-) *cis* isomer) or into the minor groove of DNA ((+) *cis*) [17]. Adduct conformations can be further influenced by DNA supercoiling and by the local sequence context [18, 19].

5-Methylcytosine (^{Me}C) is an important endogenous DNA modification that plays a central role in epigenetic regulation, chromatin structure, and DNA repair [20]. The majority of ^{Me}C residues are found at 5'-CG-3' dinucleotides, including all 5'-CG-3' sites within the coding sequence of the human *p53* tumor suppressor gene [21]. Interestingly, BPDE and other diol epoxides produced upon bioactivation of PAHs present in tobacco smoke exhibit an enhanced reactivity towards the *N*²-position of guanine in ^{Me}C:G base pairs [22-25]. In particular, *N*²-BPDE-dG adducts are preferentially formed at guanine bases within ^{Me}CG dinucleotides found at the major mutational “hotspots” characteristic for smoking-induced lung cancer, e.g. codons 157, 158, 245, 248, and 273 of the *p53* tumor suppressor gene [22-25]. Partially methylated CG dinucleotides revealed that this reactivity enhancement can be attributed to ^{Me}C that is base paired with target guanine, rather than the methylated cytosine present in the 5'-flanking position [22].

The origins of 5-methylcytosine mediated effects on *N*²-BPDE-dG adduct formation are not well understood. Previous experimental and computational studies with mitomycin C, an antitumor agent that forms pre-covalent intercalative complexes with DNA, suggest that the nucleophilicity of the *N*²-position of guanine is enhanced as a result of the inductive electronic effects of the C-5 methyl group transmitted to the *N*²-amino group of G through ^{Me}C:G hydrogen



Scheme 2-1. Metabolic activation of benzo[a]pyrene to BPDE and the formation of guanine adducts.

bonds [26]. Consistent with this explanation, the presence of electron withdrawing fluoro group on the C-5 of cytosine reduces the reactivity of G:C base pairs towards mitomycin C [26, 27]. These studies suggest that the transmitted electronic effect of the methyl group may be an important factor in determining reactivity of alkylating agents, such as BPDE, towards the N^2 -position of guanine. However, experiments with non-intercalating DNA alkylating agents have shown that cytosine methylation does not affect the formation of N^2 -ethyl-deoxyguanosine adducts of acetaldehyde [28]. Therefore, C-5 cytosine methylation may enhance the reactivity of PAH diolepoxides towards CG dinucleotides by a mechanism that is distinct from its effects on electron density distribution.

Although cytosine methylation does not interfere with the overall DNA structure (the C-5 methyl substituent is readily accommodated in the major groove of DNA) [29-31], ^{Me}C decreases the major groove charge density, stabilizes DNA helix, and enhances base stacking [30, 32]. The introduction of a hydrophobic methyl group at the C-5 position of cytosine may encourage the physical binding of BPDE to DNA grooves. Furthermore, since C-5 methylation increases the molecular polarizability of cytosine [30, 33], it is likely to stabilize intercalative complexes of aromatic carcinogens such as BPDE with DNA *via* increased π - π stacking interactions [34]. Indeed, Geacintov *et al.* have shown that ^{Me}C enhances the intercalative binding of BPDE to poly(dG- ^{Me}C) duplexes [8] and shifts the orientation of (-)-*trans*- N^2 -BPDE-dG adducts from an external minor groove structure to an intercalative conformation [35, 36]. The preferential pre-covalent complex formation at ^{Me}C :G base pairs is expected to increase the yields of N^2 -BPDE-dG adducts at methylated CG dinucleotides.

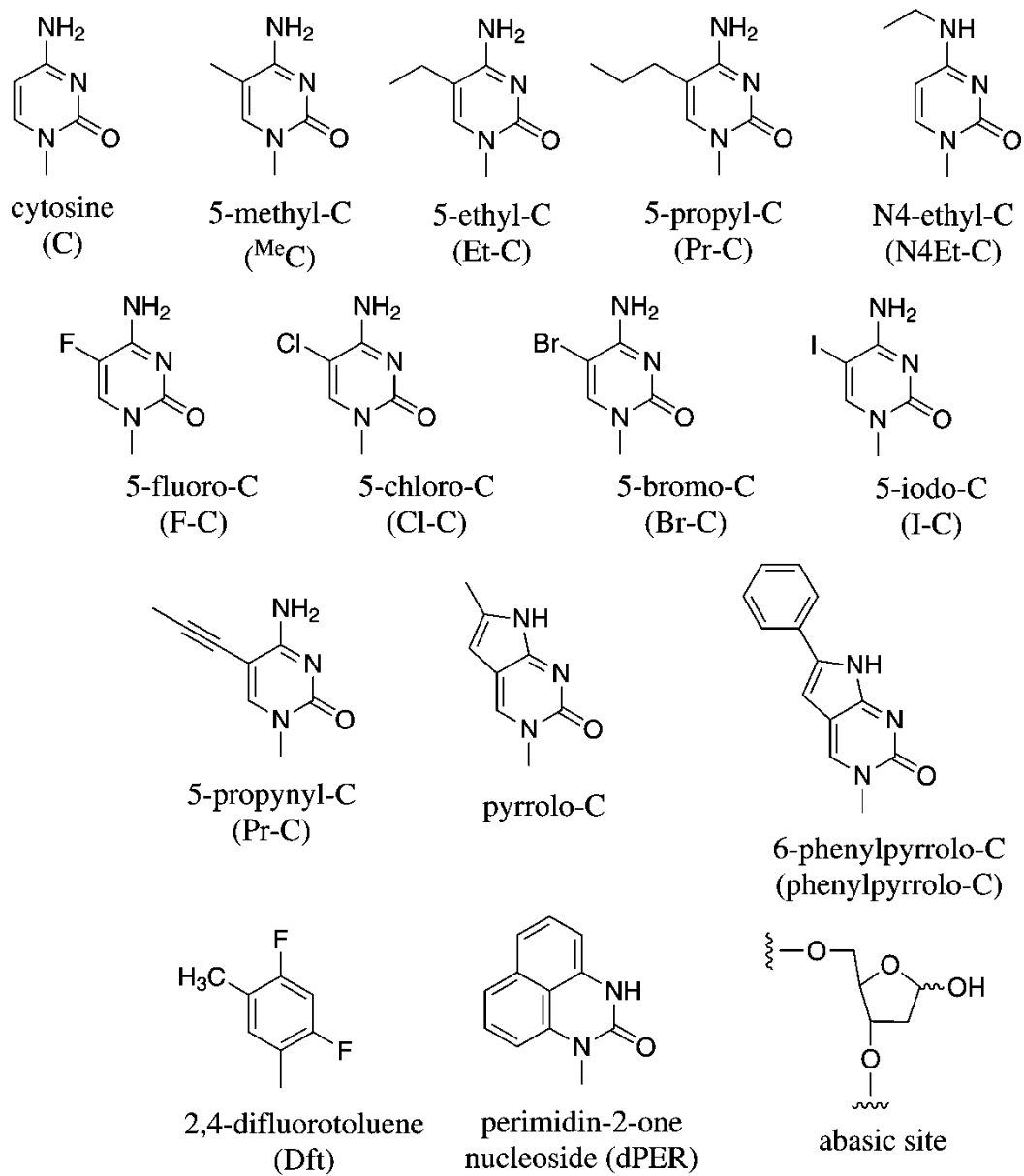
The purpose of this work was to identify the mechanism(s) by which the presence of the C-5 methyl group on cytosine alters the reactivity of endogenously occurring 5'- ^{Me}C G-3' steps in

DNA towards BPDE and other PAH diolepoxides. A series of C-5 substituted cytosines and related structural analogs, including 5-ethyl-C, 5-propyl-C, 4-ethyl-C, 5-fluoro-C, 5-chloro-C [37], 5-bromo-C, 5-iodo-C, difluorotoluene [38], 5-propynyl-C, pyrrolo-C, 6-phenylpyrrolo-C [39], and perimidin-2-one nucleoside (dPER) [40] (Scheme 2-2), were placed into synthetic DNA duplexes opposite target guanine, and the formation of N^2 -guanine adducts at the modified C:G base pairs was quantified by stable isotope labeling mass spectrometry. The pre-covalent BPDE:DNA interactions were evaluated by low temperature laser-excited fluorescence spectroscopy, quantum mechanical calculations, and molecular docking experiments. Spectroscopic study shows that BPT assumes both quasi-external and intercalated geometries in its complexes with DNA, and a greater contribution of intercalated structures is observed in the presence of ^{13}C and dPER as compared to unmodified duplex. A similar trend is expected for DNA complexes with BPDE. This is in agreement with molecular docking studies which revealed that 5-alkylcytosines and unnatural nucleobase analogs with extended aromatic systems facilitate the formation of intercalative BPDE-DNA complexes, placing BPDE in a favourable orientation for nucleophilic attack by the N^2 position of guanine.

2.2 Materials and Methods

Caution: *Benzo[a]pyrene diol epoxide (BPDE) is carcinogenic and should be handled with extreme caution.*

Materials: (\pm)-*anti*-BPDE, (-)-*anti*-BPDE, benzo[a]pyrene-7*S*-*trans*-7,8-dihydrodiol ((+)-BP78D), and benzo[a]pyrene-r-7,t-8,9,10-tetrahydroetraol (*trans-anti* BPT or BPT) were obtained from the NCI Chemical Carcinogen Repository (Midwest Research Institute, Kansas City, MO).



Scheme 2-2. Nucleoside analogs employed in the study.

2.2.1 Low Temperature Fluorescence Spectroscopy

Fluorescence spectra [41] of benzo[*a*]pyrene-r-7,t-8,9,10-tetrahydrotetraol (*trans-anti*-BPT or BPT) and its complexes with DNA were recorded at 77K using excitation wavelengths of 346 or 355 nm. Double stranded DNA 19-mers containing a centrally positioned X:G base pair (5'-CCCGGCACCC GCGTCCGCG-3', + strand; GGG CCG TGG GCG XAG GCG C, - strand, where G is the guanine of mutation hot-spot, and X = cytosine, 5-methylcytosine, or dPER) were dissolved in 50 mM Tris-HCl buffer, pH 7.5, to reach a concentration of 40 μ M. Stock solutions of BPT were prepared in DMSO. An appropriate aliquot of the BPT solution was added to the DNA solution to achieve 8 μ M concentration of BPT, with DMSO making up 10% of the volume. Control samples in the absence of DNA contained 8 μ M BPT dissolved in 50 mM Tris-HCl, pH 7.5 buffer, with DMSO making up 10% of the volume. For all fluorescence measurements, samples were placed into quartz tubes and immediately (within ~5-8 sec) immersed in a liquid nitrogen cryostat with quartz optical windows. Fluorescence spectra were taken at 77 K using laser excitation at 346 nm and 355 nm provided by a Lambda Physik FL 2002 Scanmate tunable dye laser system (operated at the frequency of 10 Hz) pumped by a Lambda Physik Lextra 100 XeCl excimer laser. A 1 m McPherson monochromator (model 2601) and a Princeton Instruments photodiode array were used for the dispersion and the detection of fluorescence. A Princeton Instruments FG-100 pulse generator was used for time-resolved spectroscopy with detector delay times from 60 ns to 100 ns and a gate width of 200 ns. 60-second acquisition time was applied to all spectra. The resolution for the spectra was ± 0.4 nm.

2.3 Results

2.3.1 Selection of Nucleobase Analogs and Oligonucleotide Synthesis

In order to investigate the mechanisms by which endogenous ^{Me}C increases the efficiency of PAH-guanine adduct formation at the base paired guanine, a series of synthetic oligodeoxynucleotide duplexes were prepared representing codons 153-158 of the *p53* tumor suppressor gene. This region of the *p53* gene was selected because it is endogenously methylated in all human tissues [21], and endogenously methylated codon 157 is specifically targeted for BPDE-dG adduct formation as compared with neighboring guanine bases [24]. Furthermore, mutations at the *p53* codon 157 (GTC → TGC) are characteristic for smoking-induced lung cancer [42].

A series of C-5 halogenated cytosines (5-fluorocytosine (F-C), 5-chlorocytosine (Cl-C), 5-bromocytosine (Br-C), and 5-iodocytosine (I-C)) were included to probe the effects of electron withdrawing groups at the C-5 of cytosine on reactivity of C:G pairs towards BPDE. The steric impact of these substituents is complementary to that of σ electron-donating alkyl groups. Furthermore, base analogs with extended aromatic systems (5-propynylcytosine (Pr-C), 6-methylpyrrolo[2,3-d]pyrimidine-2(3H)one deoxyribonucleoside (pyrrolo-C), 6-phenylpyrrolo[2,3-d]pyrimidine-2(3H)one deoxyribonucleoside (phenylpyrrolo-C) and perimidin-2-one deoxyribonucleoside (dPER)) were introduced in order to enhance the π - π stacking interactions of modified base pairs with BPDE. Two additional base analogs, 2,4-difluorotoluene (Dft) [40] and the abasic site, were included to probe the reactivity of guanine towards BPDE in the absence of complementary hydrogen bonding to cytosine.

2.3.2 Spectroscopic Studies of BPT Complexed with Oligonucleotide Duplex Sequence Derived from p53 exon 5 and its C-5 Analogs

Fluorescent spectra of molecules with pyrene moiety are sensitive to solvent effect [43, 44]. Low temperature fluorescence spectroscopy is frequently used to probe interactions between these chromophores and environments through spectral shift and relative peak intensity change. This technique has been applied to study the conformation of BPDE-DNA adduct and BPDE-derivatives/DNA complex [45]. Here studies were conducted in order to evaluate the pre-covalent interactions between (-)-*anti*-BPDE and DNA duplexes containing standard and structurally modified base pairs. The diolepoxide is hydrolytically unstable in the presence of DNA; besides, compared to the hydrolysis product benzo[*a*]pyrene tetraol (BPT), the fluorescence signal from BPDE is negligible, i.e. even when a small percentage of BPDE is hydrolyzed, most fluorescence signal may be contributed by the hydrolyzed product instead of the diolepoxide itself [7]. In addition, the hydrolysis reaction of BPDE is catalyzed by DNA, and the speed of reaction is greatly increased [7]. On the contrary, the experiment requires ~5 to 8 sec to thoroughly mix BPDE with DNA to guarantee the complete formation of BPDE/DNA physical complex before freezing the sample with liquid nitrogen. Thus, BPDE can easily change into BPT in the procedure of sample preparation, and the fluorescence signal of the sample may be mostly from BPT instead of BPDE. Therefore, *trans-anti*-benzo[*a*]pyrene tetraol (*trans-anti*-BPT) was used as a model compound. *Trans-anti*-BPT has the same stereochemistry at the C-7, C-8, C-9, and C-10 of the molecule as (+)-*anti*-BPDE and retains a similar molecular shape. The working hypothesis is that affinity of the above mentioned molecules (*trans-anti*-BPT and (+)-*anti*-BPDE) towards the DNA depends on the modification of the C-5 cytosine substituent.

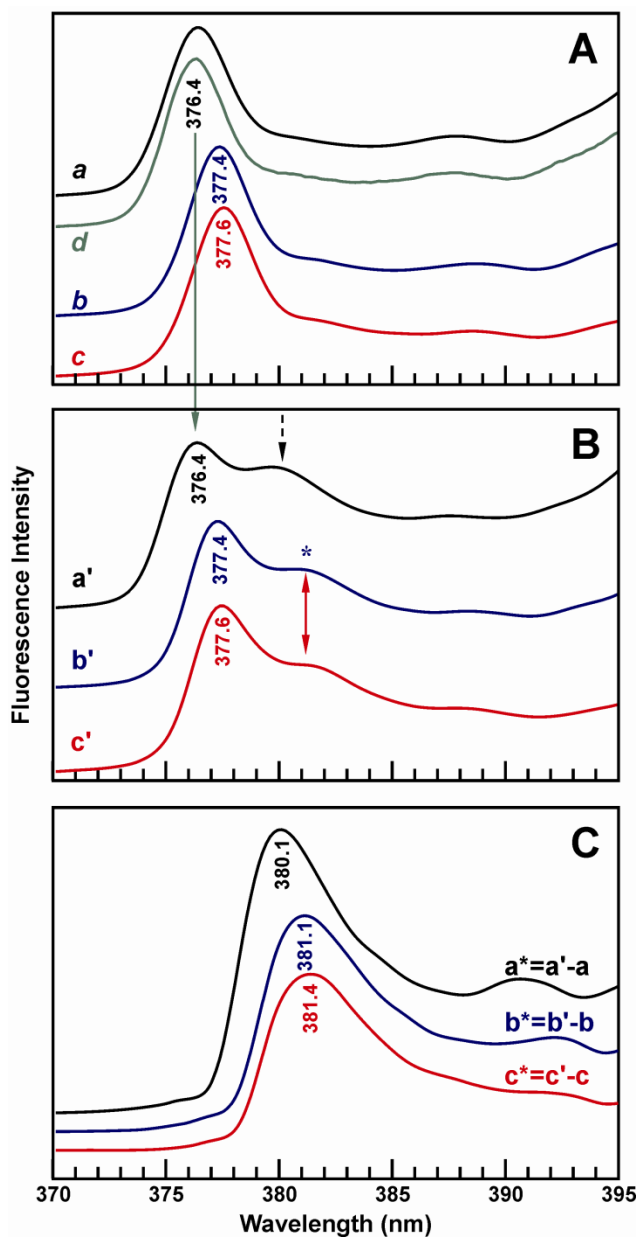


Figure 2-1. Low temperature (77 K) fluorescence origin band spectra of *trans-anti*-BPT obtained in the absence and in the presence of DNA duplexes containing a central C:G, ^{Me}C:G, or dPER:G base pair. Spectra in frame **A** were obtained with a λ_{ex} of 346 nm and a 60 ns delay time of the observation window immediately after mixing BPT with a 5-fold molar excess of DNA. Curves **a-c** correspond to the NLN spectra of BPT mixed with DNA duplexes containing C, ^{Me}C, or dPER, respectively. Spectrum **d** corresponds to BPT alone. Spectra in frame **B** were obtained with λ_{ex} of 355 nm and otherwise identical conditions as in frame **A**. Curves **a'-c'** correspond to the spectra of BPT mixed with DNA duplexes containing C, ^{Me}C, or dPER, respectively. Frame **C** shows the difference between the emission spectra obtained at 346 and 355 nm ($\mathbf{a}^* = \mathbf{a}' - \mathbf{a}$, $\mathbf{b}^* = \mathbf{b}' - \mathbf{b}$, and $\mathbf{c}^* = \mathbf{c}' - \mathbf{c}$).

Positive identification of specific propensity of BPT towards the C-5 modified analogs could provide more insight into possible factors responsible for the enhanced reactivity of ^{Me}C:G dinucleotides observed experimentally.

Figure 2-1 shows low temperature fluorescence spectra of BPT alone and in the presence of DNA duplexes containing a central G:C, ^{Me}C:G, or dPER:G base pair. Two laser wavelengths (346 nm and 355 nm) were chosen to excite different contributions of BPT/DNA physical complex [45]. The origin-band emission spectra shown in Figure 2-1A were obtained with an excitation wavelength λ_{ex} of 346 nm and 60 ns delay time of the observation window following mixing of *trans-anti*-BPT with DNA and freezing the sample with liquid nitrogen. Curves **a-c** in Figure 2-1A were obtained in the presence of DNA duplexes containing a central C:G, ^{Me}C:G, or dPER:G base pair, respectively. Spectrum **d** corresponds to BPT in the absence of DNA. Note that the fluorescence spectra of BPT alone (curve **d**) and BPT mixed with DNA duplex containing a central G:C base pair (curve **a**) are nearly identical, with the (0,0)-band observed at 376.4 nm (Figure 2-1A). In contrast, a 1 nm red shift of the (0,0)-band is observed when BPT is combined with ^{Me}C and dPER containing duplexes (curves **b** and **c** in Figure 2-1A), suggesting that BPT has an increased affinity towards DNA containing modified base pairs. Identical spectra were obtained for other delay times of the observation window (data not shown), suggestive of a well-defined association between BPT and structurally modified DNA duplexes.

Fluorescence spectra **a'**, **b'**, and **c'** in Figure 2-1B were recorded with a different excitation wavelength ($\lambda_{\text{ex}} = 355$ nm), which is selective for intercalated conformations [45]. As a result, curves **a'**, **b'** and **c'** are characterized by an increased emission at $\lambda = 380$ -381 nm (see the dashed arrow and the asterisk in Figure 2-1B). Note that the spectra obtained in the presence of ^{Me}C-containing DNA duplex (curve **b'**) and dPER-containing DNA (curve **c'**) are characterized

by a 1-1.2 nm red shift of the (0,0)-band (i.e., 377.4 nm in the ^{Me}C analog and 377.6 nm in the dPER analog) and the band at 380-381 nm, consistent with increased π - π interactions of BPT with structurally modified duplexes.

Figure 2-1C shows the difference between emission spectra obtained at $\lambda = 346$ and $\lambda = 355$ nm excitation wavelengths. Curves **a***, **b*** and **c*** correspond to BPTs in the presence of DNA duplexes containing unmodified C, ^{Me}C, and dPER respectively. Spectrum **a*** = **a'-a** reveals that the intercalative complex of BPTs with native DNA has an origin band near 380.1 nm. Curve **b*** = **b'-b** reveals a broader origin band (most likely due to stronger electron-phonon coupling) that is more red-shifted than **a***, ~381.1 nm, and shows slightly different frequencies of the vibronic bands near 388-394 nm. Spectrum **c*** obtained for BPT in the presence of dPER-containing DNA is also red shifted with the (0,0)-band near 381.4 nm. This is suggestive of increased π - π interactions between the pyrenyl residue of BPT and ^{Me}C:G or dPER:G containing DNA as compared to unmethylated DNA (Figure 2-1). We conclude that BPT assumes both quasi-external and intercalated geometries in its complexes with DNA. Furthermore, a greater contribution of intercalated structures is observed in the presence of ^{Me}C and dPER as compared to unmodified duplex. A similar trend is expected for DNA complexes with BPDE.

2.4 Discussion and Conclusion

5-Methylcytosine (^{Me}C) is among the most important endogenous modifications found in human genome. The presence of ^{Me}C in gene promoter regions alters chromatin structure, changes histone acetylation status [32, 46], and mediates DNA-protein interactions, allowing for the control of gene expression [46-50]. In mammalian cells, ^{Me}C is produced by enzymatic methylation of the C5 position of cytosine by DNA C-5 cytosine methyltransferases and is found

predominantly at CG dinucleotides [51]. About 80% of all CG sites are endogenously methylated [47].

Healthy tissues have unique cytosine methylation patterns that are carefully maintained upon DNA replication and cell division [51]. However, abnormal cytosine methylation has been observed in aging and in many human diseases, including cancer [48]. These epigenetic changes may be caused by endogenous and exogenous electrophiles that target CG dinucleotides in DNA [52-54]. For example, endogenously methylated CG dinucleotides found within the *p53* tumor suppressor gene are the sites of the major mutational “hotposts” in smoking induced lung cancer, suggesting that tobacco carcinogens preferentially modify ^{Me}CG sequences [55, 56]. Previous studies revealed that C-5 cytosine methylation increases the reactivity of the *N*²-position of guanine in C:G base pairs towards mitomycin C, mitoxantrone, esperamicins A1 and C, and PAH diol epoxides [22-25, 57]. In contrast, the presence of ^{Me}C reduces the yields of *O*⁶-alkylguanine adducts induced by alkyldiazonium ions [58] and has little effect on the reactivity of guanine bases towards formaldehyde [28] and aflatoxin B1-8,9-epoxide [59].

The main goal of the present investigation was to identify the chemical determinants responsible for ^{Me}C-mediated effects on guanine adduct formation by carcinogenic PAH diolepoxides. In theory, ^{Me}C may influence the reactivity of neighboring guanine bases towards electrophiles by modifying DNA structure, mediating pre-covalent binding of carcinogen to DNA, or by affecting the local geometry and electronics of C:G pairs. To distinguish between these possibilities, a series of nucleobase mimics was developed featuring a range of C-5 functionalized cytosines and related structural analogs (Scheme 2-2), and their effects on the reactivity of guanine introduced in the base paired position were investigated.

We found that the introduction of hydrophobic C-5 alkyl groups on cytosine specifically facilitates the formation of N^2 -BPDE-dG adducts at its partner guanine. Furthermore, the relative reactivity of guanine towards BPDE increases as the size of the C-5 alkyl group at the base paired cytosine is increased in the alkyl series. The relative reactivity of guanine base paired to halogen-substituted cytosine indicate that electronic effects alone cannot explain the effects of C-5 cytosine methylation on reactivity of CG base pairs towards BPDE and other electrophiles. The most pronounced reactivity enhancement (up to 8-fold) was observed for structural analogs designed to facilitate the intercalation of BPDE into DNA duplexes (pyrrolo-C, phenyl pyrrolo-C, and dPER) [60]. BPDE intercalation between base pairs of the DNA duplex is a required step for covalent adduct formation [61]. Intercalative BPDE-DNA interactions also significantly accelerate the hydrolysis of BPDE to the corresponding tetraols by stabilizing the transition state for nucleophilic attack by water [7]. Geacintov *et al.* have shown that BPDE prefers to intercalate within oligodeoxynucleotide duplexes of poly(dG-^{Me}C) [8]. Furthermore, the (-) *trans* N^2 -BPDE-dG adducts undergo a shift to an intercalated structure in the presence of neighboring ^{Me}C [35].

Fluorescence studies revealed that *trans-anti*-BPT (that was used as a hydrolytically stable analog of BPDE) preferentially forms intercalative complexes with DNA containing ^{Me}C and dPER as compared to unmodified DNA duplex (Figure 2-1). These results are supported by fluorescence quenching experiments conducted with benzo[*a*]pyrene-7*S-trans*-7,8- dihydrodiol ((+)-BP78D) that was mixed with DNA duplexes containing nucleobase analogs designed to optimize π - π stacking interactions with BPDE (Pr-C, Dft, and dPER). Examination of molecular models of BPDE-DNA complexes suggests that stacking interactions between the pyrene ring system of BPDE and 5-methylcytosine position the epoxy ring of BPDE in a favorable

orientation for nucleophilic attack by the N^2 -amino group of the base paired guanine, leading to increased N^2 -BPDE-dG adduct yields.

Taken together, our results make it possible to propose a likely model of how BPDE-DNA interactions are modified by 5-methylcytosine, an important endogenous base modification that controls gene expression [50] and governs the formation of smoking-induced lung cancer mutational hotspots in the *p53* tumor suppressor gene [24]. The majority of cytosine analogs considered in this study displayed an increased reactivity towards BPDE, which was associated with a facilitated physical complex formation between BPDE and DNA. Spectroscopic studies show that a greater contribution of intercalated structures for BPT:DNA complexes is observed in the presence of ^{Me}C and dPER as compared to unmodified duplex. A similar trend is expected for DNA complexes with BPDE. Density functional calculations reveal that the electronic properties of the modified C:G base pair are affected by the C-5 cytosine substituent, but that these changes alone do not predict reactivity [62]. We conclude that C-5 methylation on cytosine increases the yields of N^2 -BPDE-dG lesions at the base paired guanine mostly by facilitating the formation of pre-covalent intercalative complexes with BPDE.

References

- [1] International Agency for Research on Cancer (IARC) (1983) Polynuclear aromatic compounds, part I, chemical, environmental, and experimental data. *IARC Monographs on the Evaluation of the Carcinogenic Risk of Chemicals to Humans*. IARC, Lyon, France, pp. 33-451.
- [2] Pfeifer, G. P., Denissenko, M. F., Olivier, M., Tretyakova, N., Hecht, S. S., Hainaut, P., *Oncogene* 2002, 21, 7435-7451.
- [3] Yang, S. K., Roller, P. P., Gelboin, H. V., *Biochemistry* 1977, 16, 3680-3687.

- [4] Shimada, T., Fujii-Kuriyama, Y., *Cancer Sci.* 2004, 95, 1-6.
- [5] Mazerska, Z., in: Baer-Dubowska, W., Bartoszek, A., Malejka-Giganti, D. (Eds.), *Carcinogenic and Anticarcinogenic Food Components*, CRC Press, Boca Raton, Florida 2006, pp. 37-67.
- [6] Geacintov, N. E., Yoshida, H., Ibanez, V., Jacobs, S. A., Harvey, R. G., *Biochem. Bioph. Res. Co.* 1984, 122, 33-39.
- [7] Geacintov, N. E., Yoshida, H., Ibanez, V., Harvey, R. G., *Biochemistry* 1982, 21, 1864-1869.
- [8] Geacintov, N. E., Shahbaz, M., Ibanez, V., Moussaoui, K., Harvey, R. G., *Biochemistry* 1988, 27, 8380-8387.
- [9] Meehan, T., Gamper, H., Becker, J. F., *J. Biol. Chem.* 1982, 257, 10479-10485.
- [10] Jeffrey, A. M., Weinstein, I. B., Jennette, K. W., Grzeskowiak, K., Nakanishi, K., Harvey, R. G., Autrup, H., Harris, C., *Nature* 1977, 269, 348-350.
- [11] Wolfe, A. R., Yamamoto, J. A., Meehan, T., *P. Natl. Acad. Sci. USA.* 1994, 91, 1371-1375.
- [12] Meehan, T., Wolfe, A. R., Negrete, G. R., Song, Q., *P. Natl. Acad. Sci. USA.* 1997, 94, 1749-1754.
- [13] Shukla, R., Jelinsky, S., Liu, T. M., Geacintov, N. E., Loechler, E. L., *Biochemistry* 1997, 36, 13263-13269.
- [14] Suh, M., Ariese, F., Small, G. J., Jankowiak, R., Liu, T. M., Geacintov, N. E., *Biophys. Chem.* 1995, 56, 281-296.
- [15] Cosman, M., Delossantos, C., Fiala, R., Hingerty, B. E., Singh, S. B., Ibanez, V., Margulis, L. A., Live, D., Geacintov, N. E., Broyde, S., Patel, D. J., *P. Natl. Acad. Sci. USA.* 1992, 89, 1914-1918.
- [16] Delossantos, C., Cosman, M., Hingerty, B. E., Ibanez, V., Margulis, L. A., Geacintov, N. E., Broyde, S., Patel, D. J., *Biochemistry* 1992, 31, 5245-5252.
- [17] Cosman, M., Hingerty, B. E., Luneva, N., Amin, S., Geacintov, N. E., Broyde, S., Patel, D. J., *Biochemistry* 1996, 35, 9850-9863.

- [18] Jiang, G. H., Jankowiak, R., Grubor, N., Banasiewicz, M., Small, G. J., Skorvaga, M., Van Houten, B., States, J. C., *Chem. Res. Toxicol.* 2004, *17*, 330-339.
- [19] Rodriguez, F. A., Cai, Y., Lin, C., Tang, Y., Kolbanovskiy, A., Amin, S., Patel, D. J., Broyde, S., Geacintov, N. E., *Nucleic Acids Res.* 2007, *35*, 1555-1568.
- [20] Riggs, A. D., *Advances in Cancer Research* 1983, *40*, 1-30.
- [21] Tornaletti, S., Pfeifer, G. P., *Oncogene* 1995, *10*, 1493-1499.
- [22] Matter, B., Wang, G., Jones, R., Tretyakova, N., *Chem. Res. Toxicol.* 2004, *17*, 731-741.
- [23] Denissenko, M. F., Pao, A., Tang, M. S., Pfeifer, G. P., *Science* 1996, *274*, 430-432.
- [24] Denissenko, M. F., Chen, J. X., Tang, M. S., Pfeifer, G. P., *P. Natl. Acad. Sci. USA.* 1997, *94*, 3893-3898.
- [25] Tretyakova, N., Matter, B., Jones, R., Shallop, A., *Biochemistry* 2002, *41*, 9535-9544.
- [26] Das, A., Tang, K. S., Gopalakrishnan, S., Waring, M. J., Tomasz, M., *Chem. Biol.* 1999, *6*, 461-471.
- [27] Dannenberg, J. J., Tomasz, M., *J. Am. Chem. Soc.* 2000, *122*, 2062-2068.
- [28] Matter, B., Guza, R., Zhao, J., Li, Z.-z., Jones, R., Tretyakova, N., *Chem. Res. Toxicol.* 2007, *20*, 1379-1387.
- [29] Rauch, C., Trieb, M., Wellenzohn, B., Loferer, M., Voegelé, A., Wibowo, F. R., Liedl, K. R., *J. Am. Chem. Soc.* 2003, *125*, 14990-14991.
- [30] Norberg, J., Vihinen, M., *J. Mol. Struct. (THEOCHEM)* 2001, *546*, 51-62.
- [31] Hodgesgarcia, Y., Hagerman, P. J., *Biochemistry* 1992, *31*, 7595-7599.
- [32] Hausheer, F. H., Rao, S. N., Gamcsik, M. P., Kollman, P. A., Colvin, O. M., Saxe, J. D., Nelkin, B. D., McLennan, I. J., Barnett, G., Baylin, S. B., *Carcinogenesis* 1989, *10*, 1131-1137.
- [33] Sowers, L. C., Shaw, B. R., Sedwick, W. D., *Biochem. Biophys. Res. Co.* 1987, *148*, 790-794.
- [34] Geacintov, N. E., Cosman, M., Hingerty, B. E., Amin, S., Broyde, S., Patel, D. J., *Chem. Res. Toxicol.* 1997, *10*, 111-146.

- [35] Huang, X. W., Colgate, K. C., Kolbanovskiy, A., Amin, S., Geacintov, N. E., *Chem. Res. Toxicol.* 2002, 15, 438-444.
- [36] Zhang, N., Lin, C., Huang, X. W., Kolbanovskiy, A., Hingerty, B. E., Amin, S., Broyde, S., Geacintov, N. E., Patel, D. J., *J. Mol. Biol.* 2005, 346, 951-965.
- [37] Kang, J. I., Burdzy, A., Liu, P. F., Sowers, L. C., *Chem. Res. Toxicol.* 2004, 17, 1236-1244.
- [38] Kool, E. T., Sintim, H. O., *Chem. Commun.(Camb.)* 2006, 3665-3675.
- [39] Wojciechowski, F., Hudson, R. H. E., *J. Am. Chem. Soc.* 2008, 130, 12574-12575.
- [40] Gong, J., Sturla, S. J., *J. Am. Chem. Soc.* 2007, 129, 4882-4883.
- [41] Miksa, B., Chinnappan, R., Dang, N. C., Reppert, M., Matter, B., Tretyakova, N., Grubor, N. M., Jankowiak, R., *Chem. Res. Toxicol.* 2007, 20, 1192-1199.
- [42] Hainaut, P., Pfeifer, G. P., *Carcinogenesis* 2001, 22, 367-374.
- [43] Nakajima, A., *B. Chem. Soc. JPN.* 1971, 44, 3272-3277.
- [44] Kalyanasundaram, K., Thomas, J. K., *J. Am. Chem. Soc.* 1977, 99, 2039-2044.
- [45] Jankowiak, R., Lu, P. Q., Small, G. J., Geacintov, N. E., *Chem. Res. Toxicol.* 1990, 3, 39-46.
- [46] Newell-Price, J., Clark, A. J. L., King, P., *Trends Endocrinol. Metab.* 2000, 11, 142-148.
- [47] Ehrlich, M., Gamasosa, M. A., Huang, L. H., Midgett, R. M., Kuo, K. C., McCune, R. A., Gehrke, C., *Nucleic Acids Res.* 1982, 10, 2709-2721.
- [48] Millar, D. S., Holliday, R., Grigg, G. W., in: Beck, S., Olek, A. (Eds.), *the Epigenome, Molecular Hide and Seek*, Wiley-VCH GmbH Co. KGaA, Weinheim, Germany 2003, pp.3-20.
- [49] Widschwendter, M., *Dis. Markers* 2007, 23, 1-3.
- [50] Bird, A. P., *Nature* 1986, 321, 209-213.
- [51] Cedar, H., Razin, A., *Biochim. Biophys. Acta* 1990, 1049, 1-8.
- [52] Valinluck, V., Liu, P., Kang, J. I., Burdzy, A., Sowers, L. C., *Nucleic Acids Res.* 2005, 33, 3057-3064.

- [53] Valinluck, V., Tsai, H. H., Rogstad, D. K., Burdzy, A., Bird, A., Sowers, L. C., *Nucleic Acids Res.* 2004, 32, 4100-4108.
- [54] Baskunov, V. B., Subach, F. V., Kolbanovskiy, A., Kolbanovskiy, M., Eremin, S. A., Johnson, F., Bonala, R., Geacintov, N. E., Gromova, E. S., *Biochemistry* 2005, 44, 1054-1066.
- [55] Pfeifer, G. P., Tang, M. S., Denissenko, M. F., *Curr. Top. Microbiol. Immunol.* 2000, 249, 1-19.
- [56] Pfeifer, G. P., *Mutat. Res.* 2000, 450, 155-166.
- [57] Mathur, P., Xu, J., Dedon, P. C., *Biochemistry* 1997, 36, 14868-14873.
- [58] Ziegel, R., Shallop, A., Upadhyaya, P., Jones, R., Tretyakova, N., *Biochemistry* 2004, 43, 540-549.
- [59] Ross, M. K., Mathison, B. H., Said, B., Shank, R. C., *Biochem. Biophys. Res. Co.* 1999, 254, 114-119.
- [60] Guza, R., Kotandeniya, D., Murphy, K., Dissanayake, T., Lin, C., Giambasu, G., Lad, R., Wojciechowski, F., Amin, S., Sturla, S., York, D., Jankowiak, R., Jones, R., Tretyakova, N., *Nucleic Acids Res.* 2011, 39, 3988-4006.
- [61] Becker, J. F., Strunk, S. J., Martinez, K. G., Waltman, T., Meehan, T., *Cancer Biochem. Biophys.* 1986, 9, 67-73
- [62] Moser, A., Guza, R., Tretyakova, N., York, D. M., *Theor. Chem. Acc.* 2009, 122, 179-188.

Chapter 3

On Stabilization of a Neutral Aromatic Ligand by π -Cation Interactions in Monoclonal Antibodies

Chen Lin^{1,#}, Raja Chinnappan^{1,#}, Khem Acharya¹, Jean-Luc Pellequer², and Ryszard Jankowiak¹
(published in *Biophysical Chemistry* 2011, 154, 35-40)

¹Department of Chemistry, Kansas State University, Manhattan, KS 66506, USA

²CEA, iBEB, Department of Biochemistry and Nuclear Toxicology, F-30207 Bagnols sur Cèze, France

[#]Chen Lin and Raja Chinnappan are co-first authors.

Abstract

It has been shown that *anti*-PAH mAb can bind a particular cross-reactant by adopting two distinct “red” and “blue” conformations of its binding sites [N.M. Grubor et al. *PNAS* 2005, *102*, 7453-7458]. In the case of red conformation of pyrene (Py)/*anti*-PAH mAb (with a broad fluorescence (0,0)-band with FWHM $\sim 140\text{ cm}^{-1}$), the central role in complex formation was played by π - π interactions. The nature of the blue-shifted conformation with very narrow fluorescence (0,0)-band (FWHM $\sim 75\text{ cm}^{-1}$) was left unclear due to the lack of suitable data for comparison. In this work, we suggest spectroscopic and modeling results obtained for the blue conformation of Py in several mAb (including 4D5 mAb) are consistent with π -cation interactions, underscoring the importance of π -cation interaction in ligand binding and stabilization in agreement with earlier modeling studies [J-L. Pellequer, et al. *J. Mol. Biol.* 2000, *302*, 691-699]. We propose considerable narrowing of the fluorescence origin band of ligand in the protein environment could be regarded as a simple indicator of π -cation interactions. Since 4D5 mAb forms only the blue-shifted conformation, while *anti*-PAH and 8E11 mAbs form both blue- and red-shifted conformations, we suggest mAb interactions, with Py molecules lacking H-bonding functionality, may induce distinct conformations of mAb binding sites that allow binding by π - π and/or π -cation interactions.

List of Abbreviations

Ab, antibody; Arg, arginine; mAb, monoclonal antibody; BP, benzo[*a*]pyrene; BPDE, benzo[*a*]pyrene dilepoxide; BPT, benzo[*a*]pyrene tetrol; CE, capillary electrophoresis; FLNS, fluorescence line-narrowing spectroscopy; FWHM, full width at half maximum; Glu, glutamine; LIF, laser-induced fluorescence; Lys, lysine; NLN, non line-narrowed; PAH, polycyclic aromatic hydrocarbon; PBS, phosphate-buffered saline buffer; Py, pyrene; ZPL, zero-phonon lines; Γ_{inh} , inhomogeneous broadening; PDB, protein data bank; CDR, complementarity determining region.

3.1 Introduction

Antibodies (Ab) possess exceptional capability to selectively recognize and reversibly bind target molecules against which they are raised, as they exhibit a marked ability to acquire new functions [1]. Binding strength and binding selectivity in Ab-ligand interactions are mainly the consequence of salt bridges, hydrogen bonds, and van der Waals contacts [2]. It is believed antigen-binding promiscuity of a monoclonal antibody (mAb) is largely due to structural flexibility and conformational multiplicity of its binding sites. There are many examples in the literature of non-specific (cross-reactive) Ab [3, 4] with their cross-reactivity ranging from broad promiscuity (where mAb binds molecules that are not structurally related), sometimes even with several orders of magnitude in size difference [5] to so-called group specificity (where an antibody recognizes a family of molecules with similar structural features but ignores structurally unrelated molecules) [6-8]. Unfortunately, the relationship between mAb structure and function, including the mode of interaction, is often unknown and therefore studies in this area continue to be of interest in biochemical and bioanalytical sciences.

One particularly large group of biologically important molecules of interest is polycyclic aromatic hydrocarbons (PAH), their metabolites, and PAH-derived DNA-adducts. Among them, special attention has been paid to benzo[*a*]pyrene (BP) and its derivatives due to their ubiquitous

potency toward cellular DNA damage and the subsequent carcinogenicity of these processes [9]. Depending on the metabolic activation pathway, BP-derived DNA adducts may possess a pyrene (Py) moiety that could reveal different modes of interaction with various mAb binding pockets. For example, our recent work has established the applicability of cross-reactive mAbs for highly specific analyses of complex stereoisomeric mixtures using fluorescence line-narrowing spectroscopy (FLNS) [10, 11]. The highly promiscuous *anti*-PAH mAb can be used for capturing and analysis (detection, differentiation, and structural analysis) of not only structurally related PAHs (i.e., fluoranthene, Py, BP) but also their metabolic derivatives (i.e., diastereomeric BP-tetrols, BPTs) [11]. We have also shown that FLNS can identify various haptens cross-reacted with mAb [11], and that mAb can bind a particular cross-reactant by adopting two distinct conformations of its binding sites. We argued that, in the case of the “red-shifted” conformation of Py/*anti*-PAH mAb (with a broad (0,0)-band at 373.7 nm; full width at half maximum (FWHM) of $\sim 140\text{ cm}^{-1}$), the central role in complex formation was played by π - π interactions [10]. However, the nature of the “blue-shifted” conformation of Py/*anti*-PAH mAb with the narrow fluorescence (0,0)-band at 372.3 nm (FWHM $\sim 75\text{ cm}^{-1}$) was not discussed in detail due to lack of suitable data for comparison.

In this work, we investigate the nature of the blue-shifted conformation of the Py/*anti*-PAH mAb complex by comparison with the conformation of pyrene in 4D5 and 8E11 mAb complexes. The 4D5 mAb has been selected as previous modeling studies [12] revealed π -cation interactions as an important factor in ligand binding; in fact, it has been suggested that proteins may use neutral, aromatic side chains to stabilize bound ligands through π -cation interactions [13]. Though not confirmed experimentally for PAHs, it is well known that cation- π interactions are among the strongest of noncovalent forces [14]. For example, these interactions

are important in horseradish peroxidase, where it was shown that an active site arginine (Arg) was essential to aromatic donor binding [15].

We explore the importance of π -cation and amino-aromatic interactions in biological molecular recognition using low-temperature, laser-induced fluorescence spectroscopy in both low- and high-resolution (FLNS) modes [9, 16-18] and modeling studies. We confirm the presence of π - π interaction in the previously studied *anti*-PAH mAb [10, 11] and suggest that a neutral aromatic ligand can also be stabilized by the π -cation interactions in the protein aromatic ligand/mAb complex. We argue the latter mode of interaction leads to very small inhomogeneous broadening (Γ_{inh}) and different energy of the origin-band than that expected for π - π interactions. We propose differences observed in Γ_{inh} and position of the (0,0)-bands could be used to provide information on the binding mode between various haptens and mAb.

3.2 Materials and Methods

3.2.1 Low-temperature Fluorescence Spectroscopy

For laser-induced fluorescence (LIF)-based spectroscopic measurements (under non-line-narrowing (NLN) conditions), laser excitation at 308 nm was provided by a Lambda Physik Lextra 100 XeCl excimer laser. For FLNS measurements, the same laser was used as a pump source for a Lambda Physik FL 2002 Scanmate tunable dye laser system (10 Hz). A 1-m McPherson monochromator (model 2601) and a Princeton Instruments photodiode array were used for dispersion and detection of fluorescence. A Princeton Instruments FG-100 pulse generator was used for time-resolved spectroscopy with detector delay times from 0 ns to 160 ns and a gate width of 200 ns. For all spectroscopic measurements, 30 μ L volumes of sample free pyrene (Py) and/or Py/mAb complexes were placed in quartz tubes and immersed in a helium

cryostat with quartz optical windows. To ensure quantitative binding of haptens, immunocomplexes were formed by incubation of a 10-fold excess of mAb relative to the concentration of haptens ($2\text{-}5\times 10^{-7}$ M) in the phosphate-buffered saline (PBS) buffer. All fluorescence spectra are the average of 10 one-second acquisitions unless stated differently. The resolution for FLN and NLN spectra was ± 0.05 nm and 0.2 nm, respectively. Thus, corresponding accuracy in vibrational frequencies for FLNS measurements is about ± 3 cm^{-1} .

3.3.2 Monoclonal Antibodies (mAbs)

The purified *anti*-PAH mAb was purchased from Strategic Biosolutions, Newark, DE, USA. The 4D5 and 8E11 mAbs were obtained from Prof. Regina M. Santella (Columbia University, New York); the 4D5 hybridoma line was raised against a PAH-protein conjugate[19]; and the 8E11 mAb was raised against a BP-DNA conjugate [20]. The IgG type 8E11 and 4D5 mAbs were further purified in our laboratory from immobilized protein G resin (obtained from Pierce Inc. Rockford, IL). All buffers and the protein G resin were equilibrated to room temperature before use. (Protein G has strong binding affinity with IgG type mAbs). The immobilized protein G resin was packed in a 2-mL polypropylene column. The column was equilibrated by adding 5 mL of PBS buffer; the buffer was drained through the column. The sample was added to the column and allowed to flow completely into the resin (total content of the antibody was less than 80% of column capacity). Non-IgG components, if present, were washed from the resin using 15 mL of the PBS buffer. The bound IgG mAb was eluted by 5-mL of elution buffer (pH = 2-3; Pierce Inc.). The 0.5 mL fractions were collected and immediately neutralized using a 1 M Tris buffer (pH = 8.0). The IgG mAb-containing solution was dialyzed using a Slide-A-Lyzer Dialysis cassette (Pierce Inc.) against the PBS buffer. The final concentration of the mAb was measured from the UV absorption at 280 nm using a Nanodrop

spectrophotometer, and mAbs were stored at -80 °C before use. Methanol and glycerol (Aldrich, Milwaukee, WI) were used as received. PBS buffer (0.1 M sodium phosphate and 0.15 M sodium chloride) was purchased from Pierce and prepared according to the procedure supplied by the manufacturer.

3.2.3 Haptens

The selection of Py for these studies was intentional for several reasons: i) its fluorescence spectra are sensitive to small changes in their microenvironment [21-23]; ii) spectral properties of Py under high-resolution fluorescence conditions are well understood and described [9-11, 17, 18, 24]; and iii) Py and related molecules are among the most important environmental contaminants. BPDE-dG diastereomers ((-)-*trans*-BPDE-dG, (+)-*cis*-BPDE-dG, (-)-*cis*-BPDE-dG, and (+)-*trans*-BPDE-dG) were prepared by treating calf thymus DNA with (±)-*anti*-BPDE as described in ref. [25].

3.2.4 Computational Methodologies

Docking of Py in mAb. The molecular model of the 4D5 mAb variable region was based on the structural template of antibody 17/9 (Protein Data Bank (PDB) code 1HIL) as described in ref. [12]. As before, the third complementarity determining region (CDR) of the light chain (L3) was built using the corresponding region in antibody HyHEL5 (PDB code 3HFL), whereas the short third CDR of the heavy chain (H3) was built by computer graphics. The final model was energy-minimized in X-PLOR using the CHARM22 force field as described previously [12]. Py has been docked into the binding pocket of 4D5 using AUTODOCK. The computation was set using a 64x64x64 cubic grid with a spacing of 0.5 Å centered on the N ζ atom of LysL89.

Docking was performed using the simulated annealing procedure of AUTODOCK as described previously [26].

UV transitions. The stabilization of Py by a cationic, protein side chain in the 4D5 mAb binding pocket was further studied by quantum mechanical calculations. Energies of the (0,0)-transitions of Py in the nine lowest-energy conformations of Py in 4D5 mAb were calculated using the HyperChem (Hypercube, Inc.) ZINDO/S method with configurational interaction. The overlap weighting factor for σ - σ and π - π were 1.267 and 0.585, respectively. (0,0)-transitions were also calculated for Py in water and mutated 4D5 mAb, where the cationic side chain Arg was replaced by glutamine (Glu). For Py in water the AMBER program was used to optimize geometry of Py and water molecules; a periodic box of $18.7 \times 18.7 \times 18.7 \text{ \AA}^3$ was used with the electrostatic and van der Waals scale factors of 0.833 and 0.5, respectively.

3.3 Results

3.3.1 Conformation of Py/4D5 mAb complex.

It has been confirmed the binding site of the 4D5 mAb has an exceptionally deep antigen-binding pocket with two positively charged residues, LysL89 and ArgH95 (the nomenclature is from ref. [12], where L stands for the light chain and H for the heavy chain), which create substantial positive electrostatic potential in the binding pocket. Presence of LysL89 and ArgH95 in the binding pocket seems unusual given the hydrophobic nature of the PAHs; yet, these side-chain conformations could be reliably predicted. The role of these side chains has been studied before using site-directed mutagenesis *in silico* [12]. For example, LysL89 was replaced by methionine, a neutral, linear side chain; and ArgH95 was replaced by glutamine, a polar but uncharged side chain. Neither the ArgH95Gln mutant nor the LysL89Met/

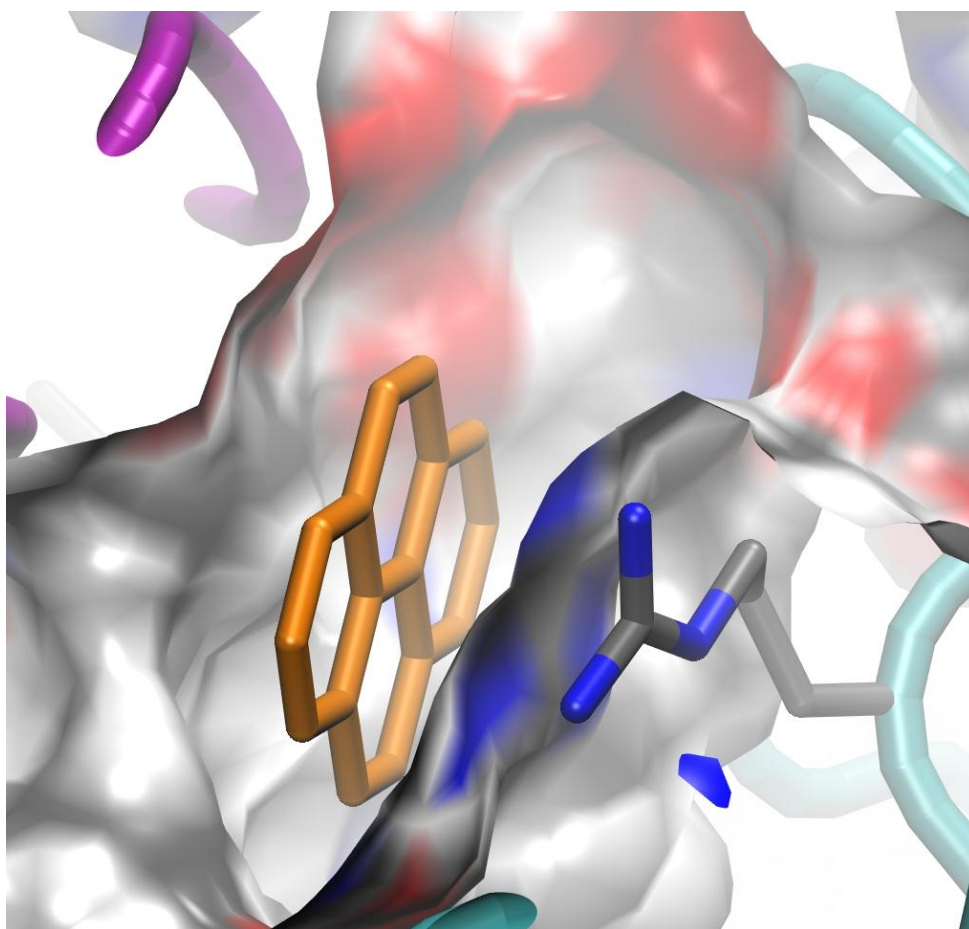


Figure 3-1. Model of the 4D5 mAb fragment with Py (orange sticks) docked in the lowest binding energy conformation in the mAb binding pocket represented by its molecular surface. The tube in cyan is the heavy chain; tube in magenta corresponds to light chain. Only the ArgH95 and Py are displayed for clarity. The molecular surface is colored by atom type. Graphics was made using VMD [27].

ArgH95Gln double mutant showed detectable binding of Py to 4D5 using indirect enzyme-linked immunosorbent assays [12]. This was consistent with a surprisingly highly polar binding pocket, considering the hydrophobicity of the antigen. The π -cation interaction of Py with Arg in 4D5 mAb is illustrated in Figure 3-1, which shows the guanidino group of Arg has parallel position in respect to the Py plane. The distance between the Py plane and the guanidino group is around 3-4 Å. Thus, the Arg side chain that flanks one side of the binding pocket is essential for Py binding, suggesting an π -cation interaction stabilizes the bound PAH. It should be emphasized that no aromatic side chain is located in the deep binding pocket of 4D5 mAb. Lowest energy conformations of Py in the protein environment were further investigated by modeling studies to reveal whether the relative (calculated) shift of the (0,0) transition of Py inside the binding pocket is consistent with the experimental data.

3.3.2 NLN Fluorescence Spectra of Py Complexed with anti-PAH and 4D5 mAbs

In Figure 3-2, we compare binding of Py to *anti*-PAH and 4D5 mAb. The *anti*-PAH mAb is known to involve π - π [10, 11], while 4D5 mAb (*vide supra*) should invoke the π -cation interactions in ligand binding. The 4.2 K NLN fluorescence origin bands obtained for both Py/*anti*-PAH mAb and Py/4D5 mAb complexes are shown in frames A and B of Figure 3-2, respectively. These NLN spectra were obtained with an excitation wavelength (λ_{ex}) of 308 nm in a PBS buffer (PBS) (spectra a, c) and glycerol/PBS (G/PBS; 1/1) buffer mixture (spectra b, d). The position of Py fluorescence emission maxima in PBS buffer (371.6 nm) and G/PBS (371.1 nm) glass are shown by the dashed and dotted vertical lines, respectively. Significant spectral differences are clearly observed with the 4D5 mAb, showing only one, i.e. the “blue”-shifted conformation (labeled as conformation I). NLN spectra for Py/8E11 (not shown for simplicity)

are close to those for Py/ *anti*-PAH mAb. However, we could observe conformation similar to conformation I shown in Py/4D5 NLN spectra (see FLN spectra d and e in Figure 3-4 for further proof that conformation I exists in 8E11 mAb). As in the case of the Py/*anti*-PAH mAb complex studied previously [10], one of the conformations observed in this work (as shown in Figure 3-2A) also possesses a significantly narrower fluorescence origin band (band I). To guide the eye, and for simplicity, the bands assigned to conformations I and II are indicated by dotted blue and dashed red Gaussians, respectively. The FWHM of conformations I (“blue” conformation) and II (“red” conformation) are 75 cm^{-1} and 125 cm^{-1} , respectively. Spectral parameters for Py/mAbs complexes in different matrices are summarized in Table I. Results shown in Figure 3-2A (spectrum b) are in agreement with Ref. [10] and confirm the existence of two populations of Py in *anti*-PAH mAb that are trapped at low temperature. However, in this case, the G/PBS glass reveals relatively larger contribution from conformation I. The most striking difference between Py/*anti*-PAH (Figure 3-2A) and Py/4D5 mAb (Figure 3-2B) is that the Py/4D5 mAb complex shows only conformation I. Its FWHM is similar to conformation I of Py/*anti*-PAH mAb, i.e. $75 \pm 5\text{ cm}^{-1}$, with a weakly matrix-dependent, blue-shifted origin band. The very narrow fluorescence origin band of conformation I (and smaller red-shift) in comparison with conformation II suggests that different modes of interaction between the Py moiety and the mAb binding pocket are present.

We have also found the relative intensity ratio of band I to band II in *anti*-PAH mAb is matrix-dependent, as was clearly visible by comparison of spectra a and b in Figure 3-2A. In the case of the Py/*anti*-PAH mAb complex, this ratio slightly depends on the relative amount of glycerol, i.e. the glass (matrix) composition, and on the cooling rate (data not shown). For example, fluorescence spectrum b shown in Figure 3-2A has a relatively larger contribution from

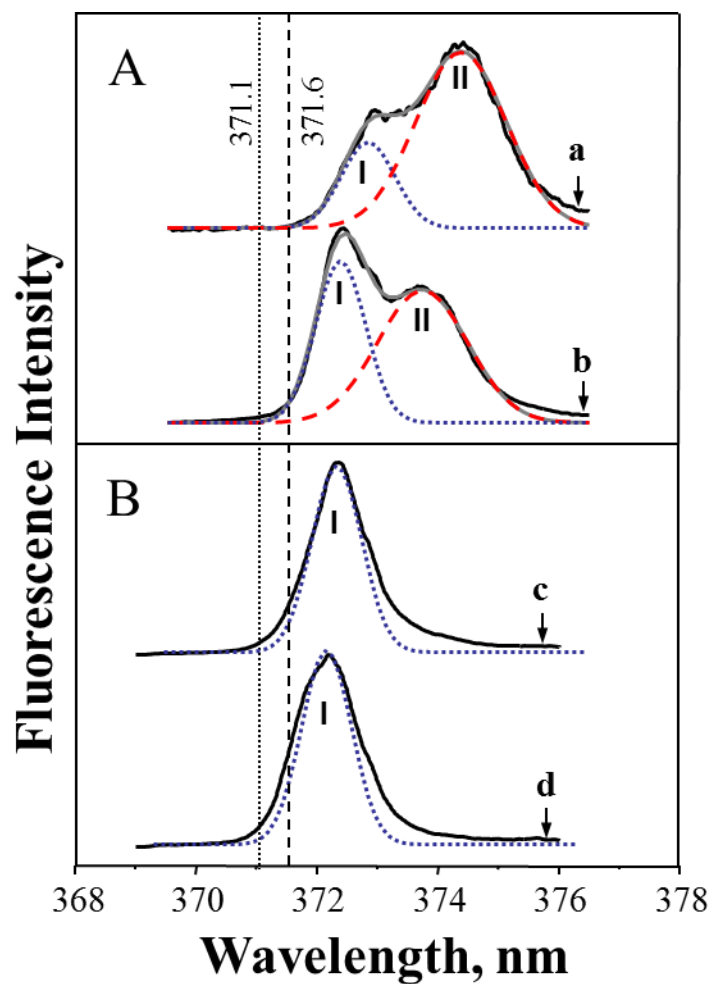


Figure 3-2. Low temperature NLN fluorescence spectra of immunocomplexed Py in *anti*-PAH mAb (frame A) and 4D5 mAb (frame B). Spectra a, c and b, d were obtained in PBS and G/PBS (1/1) matrices, respectively. The dotted and dashed vertical lines indicate the position of the (0,0)-band of free Py in G/PBS (371.1 nm) and PBS (371.6 nm) matrices. To guide an eye, the bands assigned to conformations I and II are indicated by the dotted and dashed Gaussians respectively. T = 4.2 K; gate width, 200 ns; delay time, 40 ns; $\lambda_{\text{ex}} = 308$ nm.

Table 3-1. Spectral characteristics of Py/*anti*-PAH mAb and Py/4D5 mAb complexes in PBS and G/PBS (1:1) matrices at 4.2 K. Conformation I and II correspond to the “blue” and “red” conformations, respectively.

Matrix	Py/<i>anti</i>-PAH mAb complex				Py/4D5 mAb complex ^{a)}				Py	
	Conformation I		Conformation II		Conformation I		Conformation II		(0,0) ±0.2 nm	FWHM ±5 cm ⁻¹
	(0,0) ^b ±0.2 nm	FWHM ±5 cm ⁻¹	(0,0) ±0.2 nm	FWHM ±5 cm ⁻¹	(0,0) ±0.2 nm	FWHM ±5 cm ⁻¹	(0,0) ±0.2 nm	FWHM ±5 cm ⁻¹		
PBS buffer	372.9	75	374.4	125	372.3	75	—	—	371.6	160
G/PBS matrix	372.4	75	373.6	125	372.1	75	—	—	371.1	160

^a Py/8E11 mAb complex (non-line narrowed spectra not shown) showed also conformation I (major) and conformation II (minor) as discussed in text.

^b Maximum of fluorescence (0,0)-band (in nm).

conformation I in comparison with data reported in Ref. [10], due to slightly different glass composition. This in turn suggests that the energy landscape can change due to conformational flexibility of protein. (Note, the heterogeneity of configurations in the binding pocket is responsible for the observed Γ_{inh} ; the latter, however, has nothing to do with the presence of two different subpopulations of Py). Thus, it appears the pre-existing equilibrium may also play a role in the binding process. The finding that only one conformation (i.e. blue-shifted conformation I) is observed in 4D5 mAb is consistent with the modeling studies that revealed a very deep and narrow binding pocket [12], suggesting less configurational diversity.

3.3.3 Calculated (0,0) bands

The experimentally observed shift of the (0,0)-band for conformation I of Py in 4D5 mAb, in comparison to solvated Py in both PBS buffer and PBS/G matrices, was about 1.3 nm. In contrast, our calculations showed the relative shift of the (0,0)-transition for the Py/4D5 mAb complex (for the nine calculated lowest-energy conformations, see Figure 3-3 and Table 3-2), when compared with water-solvated Py, was about 4 nm. We anticipated the calculated red-shift of the (0,0)-transition due to π - π interaction inside the binding pocket would lead to an even larger red-shift than observed experimentally; for example, calculated shift of the (0,0)-band for intercalated BPDE-DNA adducts (where π - π interaction plays a major role) are about 8 – 10 nm (data not shown), while experimentally the red-shift is about 3 nm [17, 28].

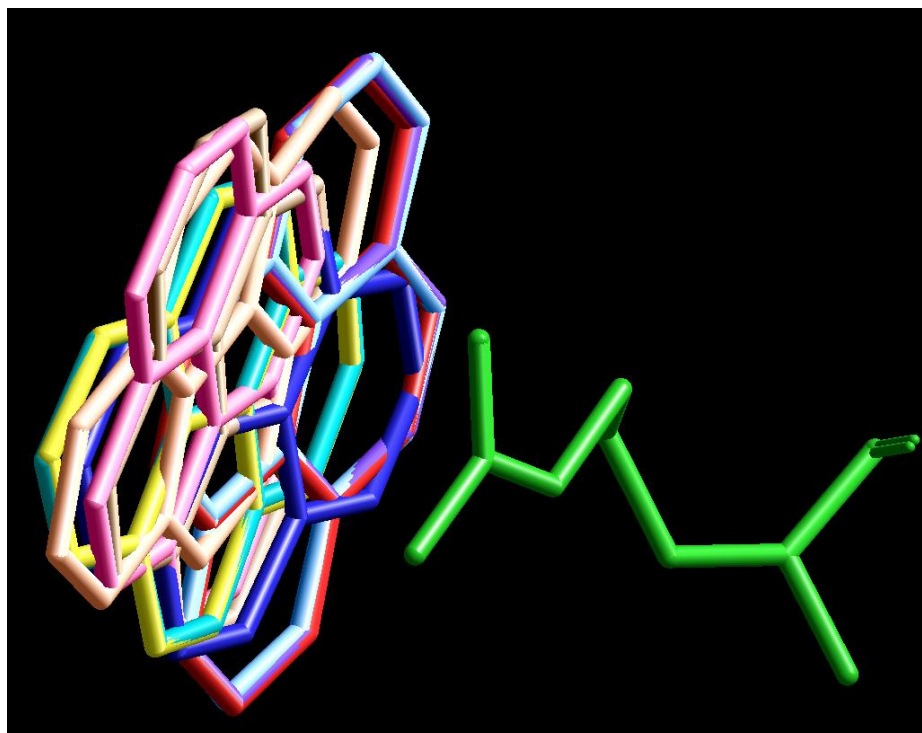


Figure 3-3. Py of nine calculated lowest-energy conformations inside the binding pocket of 4D5 mAb, and only ArgH95 (green) is shown for the spatial relationship. Different colors indicate different conformations, referred to Table 3-2. The (0,0) transition for water-solvated Py is 352.36 nm.

Table 3-2 Calculated (0,0) Transition of Py in Py/4D5

Conformation	4D5	
	(0,0)/nm	Oscillator Strength
1—cyan	355.62	0.6137
2—violet	357.08	0.6222
3—blue	357.87	0.6086
4—yellow	355.93	0.6122
5—light blue	356.74	0.6222
6—orange	358.89	0.5783
7—red	357.68	0.6149
8—brown	355.98	0.6351
9—pink	355.35	0.6523

Unfortunately, mAb with a known structure and well-defined aromatic residues inside the binding pocket (to the best of our knowledge) is not available for calculations and direct comparison. Nevertheless, we suggest the trend observed in modeling studies is consistent with the experimental data. For example, the measured (0,0)-transition of the Py-like molecules (e.g. BPDE-DNA adducts) [17, 28] intercalated between DNA bases undergoes a large (~3 nm) shift towards lower energies (due to π - π interaction) in agreement with the 2.5-3.0 nm red-shift observed in this work for conformation II (see Figure 3-2), where π - π interaction plays a major role [10].

3.3.4 FLN spectra obtained for free Py and various Py/mAb complexes

Narrowness of the (0,0)-band of conformation I is clearly visible in the FLN spectra shown in Figures 3-4 to 3-5, where the sharp peaks correspond to the resonant fluorescence zero-phonon lines (ZPL) emitting within the inhomogeneously broadened absorption profile [16, 17]. Since all spectra reported in this work were obtained using vibronic excitation, numbers above the sharp peaks in the main frames of Figures 3-4 to 3-6 correspond to the excited state vibrational frequencies. The 4.2 K spectra a-c in Figure 3-4 correspond to free Py, Py/4D5 mAb complex, and Py/*anti*-PAH mAb complex, respectively, and were obtained with λ_{ex} of 364 nm. Spectra e and d in the inset show FLN spectra of Py obtained for a different mAb (i.e. for Py/8E11 mAb complex) in PBS and glycerol/PBS matrices respectively, and are nearly identical to spectrum b in the main frame of Figure 3-4 obtained for the Py/4D5 mAb complex. This clearly indicates that Py in 8E11 mAb also adopts conformation I.

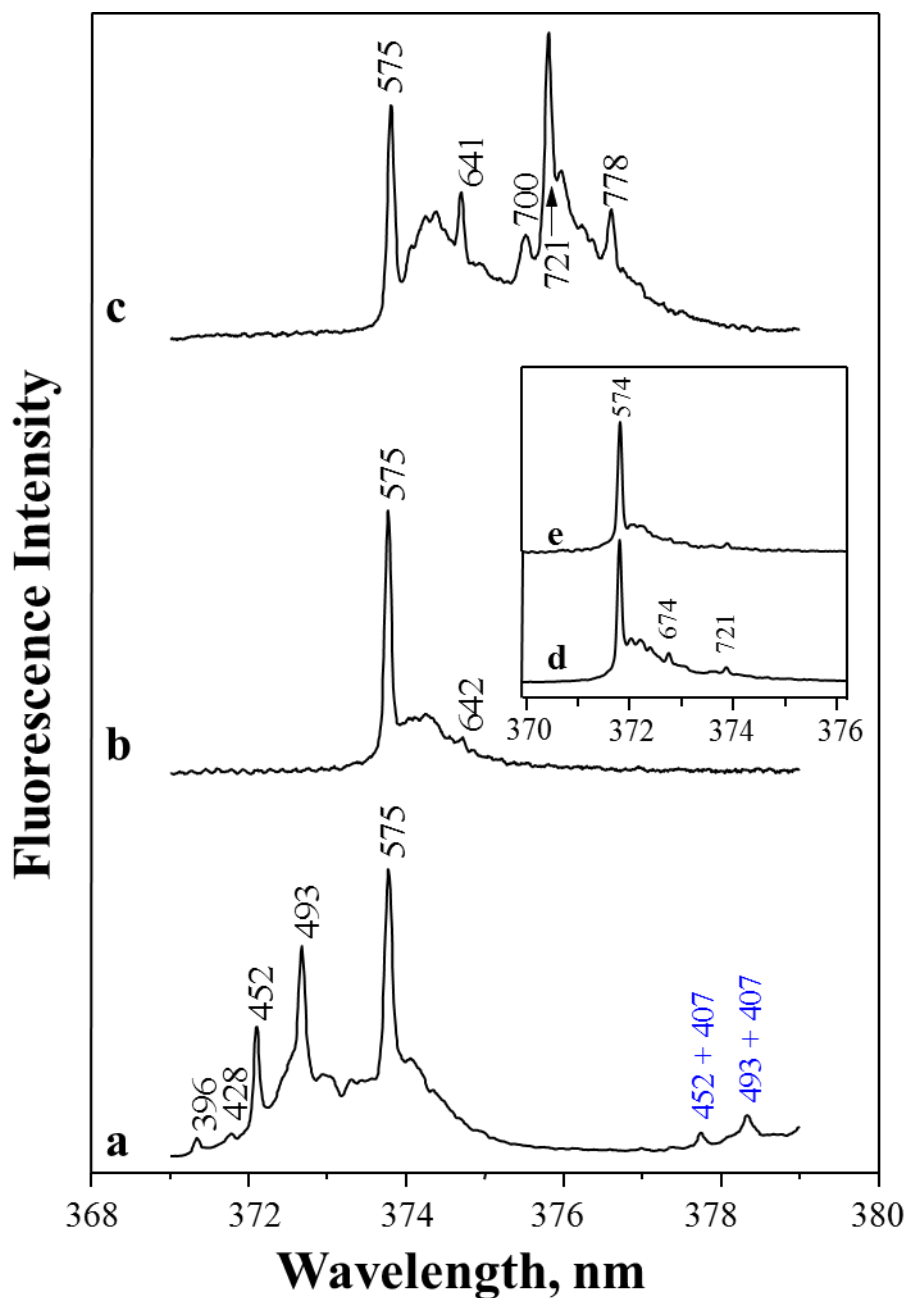


Figure 3-4. FLN spectra of Py in various mAbs at $T = 4.2$ K obtained with λ_{ex} of 364 nm (vibronic excitation). Spectra a, b, and c correspond to free Py, Py/4D5 mAb complex, and Py/*anti*-PAH complex in G/PBS (1/1) matrices, respectively. Spectra e and d in the inset show FLN spectra obtained for Py/8E11 mAb complex in PBS and G/PBS matrices, respectively; see text for details. The numbers above the peaks (i.e. the ZPL) correspond to the excited state vibrational frequencies in cm^{-1} . The 407 cm^{-1} mode corresponds to the ground state vibrational frequency of Py building on the zero-phonon lines at 452 and 493 cm^{-1} , respectively. Gate width = 200 ns, delay time = 40 ns.

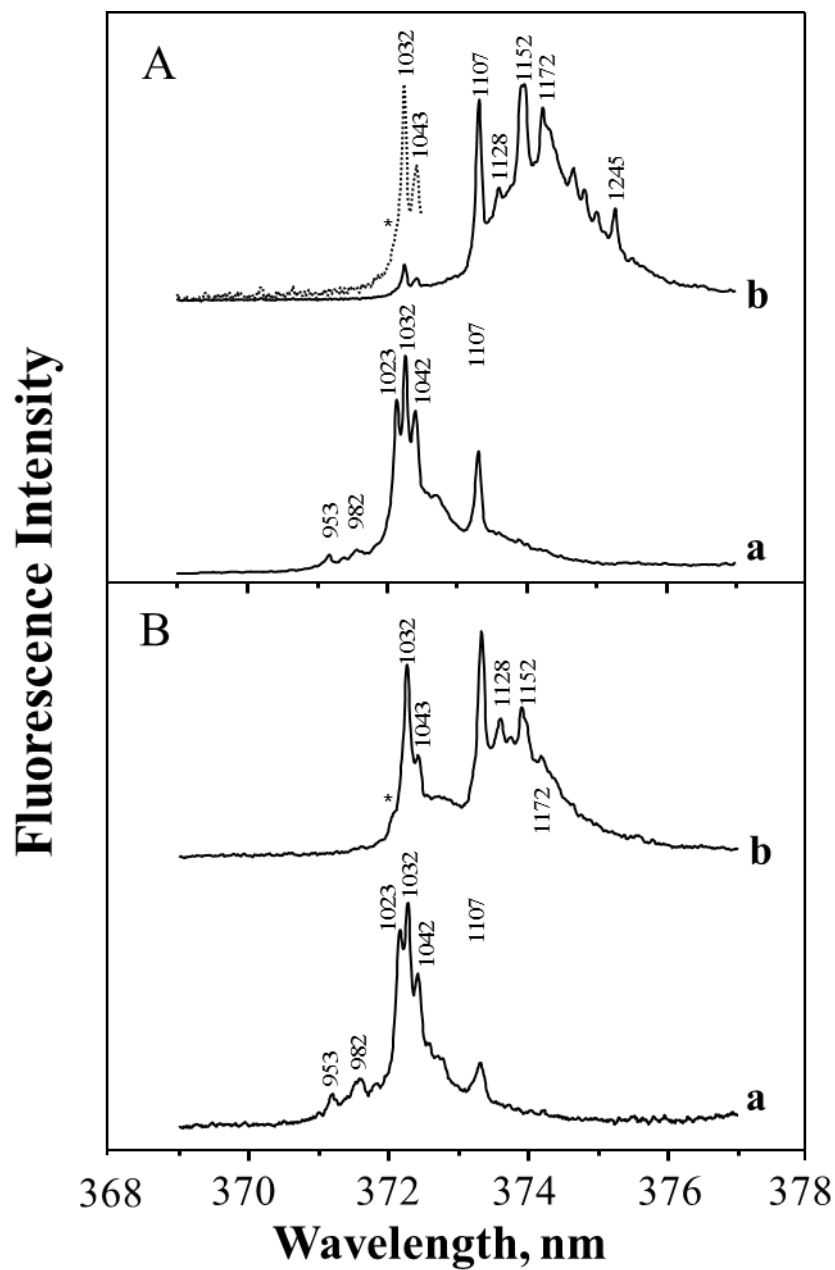


Figure 3-5. *Frame A:* Spectra a and b show FLN spectra of Py/4D5 mAb and Py/*anti*-PAH complexes in PBS buffer, respectively, obtained with $\lambda_{\text{ex}} = 358.5$ nm. The dotted line shows an expanded part of curve (a) to reveal the 1032 and 1043 cm^{-1} vibronic modes. *Frame B:* FLN spectra of Py/4D5 mAb (curve a) and Py/*anti*-PAH (curve b) complexes in G/PBS (1:1), respectively. $T = 4.2$ K, gate width = 200 ns, delay time = 40 ns. Asterisks labeled the position of 1023 cm^{-1} mode which is not resolved in FLN spectra of Py/4D5 mAb.

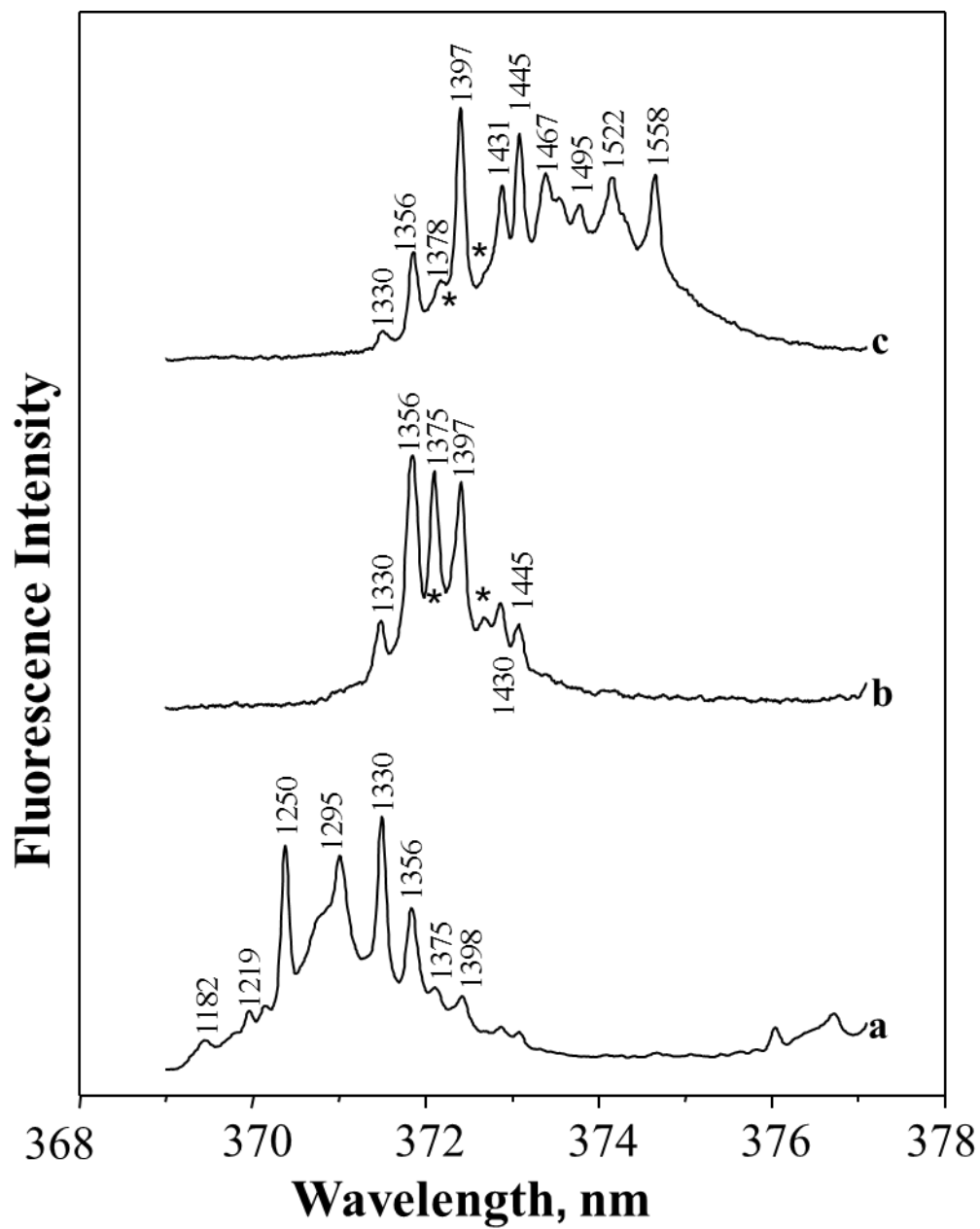


Figure 3-6. FLN spectra (4.2 K) of free Py (curve a), Py/4D5 mAb complex (curve b), and Py/*anti*-PAH mAb complex (curve c) in G/PBS glass obtained at 4.2 K. $\lambda_{\text{ex}} = 354$ nm; gate width, 200 ns; delay time, 40 ns. A different distribution of several vibrational modes is labeled by stars.

Spectra a, b, and c are distinctly different due to different band maxima; due to contribution from two conformations, the Py/*anti*-PAH mAb complex (spectrum c) shows vibrations over a broader energy range than spectrum b obtained for the Py/4D5 mAb complex. Spectra b, d, and e are consistent with a very narrow Γ_{inh} for conformation I as already indicated by the NLN spectra shown in Figure 3-2. Though the shapes of these three spectra look similar, d and e showed more intense 721 cm^{-1} mode than line b, which indicates that minor conformation II is contributed to the NLN spectra of Py/8E11 (not shown for simplicity). Note the FLN spectrum of Py (curve a of Figure 3-4) also reveals several vibrational modes within its (0,0)-band due to a larger Γ_{inh} of about 160 cm^{-1} . Comparison of curves b and d in Figure 3-2 with spectra c and b of Figure 3-4 (for $\lambda_{\text{ex}} = 364\text{ nm}$) clearly indicates the 575 cm^{-1} mode observed in curve c corresponds to Py/*anti*-PAH mAb in conformation I. Higher frequency modes at 641 cm^{-1} (at least in part) and modes at 700 , 721 , and 778 cm^{-1} correspond to conformation II. Modes in this energy range correspond to the Py C-C-C and C-C-H out-of-plane vibrations [29].

Spectra shown in frames A and B of Figure 3-5 were obtained with $\lambda_{\text{ex}} = 358.5\text{ nm}$ and correspond to the FLN spectra of pyrene/4D5 mAb (curves a) and pyrene/*anti*-PAH complexes (curves b) in PBS and G/PBS glasses, respectively. The dotted line above curve b in frame A shows an expanded part of curve b to show more clearly 1032 and 1043 cm^{-1} vibrational modes. The latter two modes (1032 cm^{-1} and 1043 cm^{-1} in curve b, frame A) can be assigned to conformation I. Note these two modes, 1032 and 1042 cm^{-1} , are more intense in the G/PBS

matrix (see curve b in frame B). The mode near 1023 cm^{-1} (indicated by a star in curves b of frames A and B, respectively) is not well resolved in Py/anti-PAH mAb independent of matrix composition. This mode, however, is well resolved for the Py/4D5 mAb complex in the G/PBS matrix (see curves a of frames A and B in Figure 3-5). Comparison of mode frequencies for conformation I (e.g. modes at $950\text{-}1107\text{ cm}^{-1}$) in spectra for two different mAbs (see Figure 3-5) reveals the binding pocket (due to slightly different interactions) can also influence some of the vibrational frequencies, i.e. the relative mode intensity of conformation I varies depending on mAb. Note the Py modes in the range of $1020\text{-}1180\text{ cm}^{-1}$ correspond to C-C stretching modes and C-C-H in-plane bending modes [29].

Figure 3-6 shows FLN spectra ($T = 4.2\text{ K}$, $\lambda_{\text{ex}} = 354\text{ nm}$) of free Py (curve a), immunocomplexed Py/4D5 mAb (curve b), and Py/*anti*-PAH (curve c) in G/PBS glass. These spectra, along with data shown in Figure 3-4, are consistent with our conclusion that Py adopts two conformations in *anti*-PAH mAb. Selective excitation of 354 nm (see curve c) reveals the minor contribution from conformation II (see modes at $1467\text{-}1558\text{ cm}^{-1}$). However, independent of excitation, Py in 4D5 mAb shows only the blue-shifted conformation I. As discussed above, these two conformations are associated with a different mode of binding. Finally, note a different distribution of several vibrational modes in Figure 3-6 labeled by stars. As mentioned in last paragraph, such changes in the intensity of various vibrational modes are most likely due to differences in the composition and shape of the binding pocket. For example, a smaller binding pocket of 4D5 mAb (without aromatic side chains) differently affects the vibrational frequencies of Py in comparison to those in *anti*-PAH and 8E11 mAbs.

3.4 Discussion

3.4.1 Comments on Control Experiments – Specificity of Binding

We hasten to add our control experiments (data not shown for simplicity; see also ref. [10]) with bovine serum albumin (BSA), bovine IgG, and 2E9 mAb (for 4-hydroxyestrone (4-OHE₁)-derived N-acetylcysteine conjugates [30]). Spectra of Py did not reveal any changes upon incubation of any of these proteins; that is, Py did not form any complex with BSA, bovine IgG, or 2E9 mAb. This clearly indicates that the different red shifts observed for Py in this work, as shown in Figures 3-2 and Table 3-1, arise from specific interactions of Py with unique binding pockets of 4D5, *anti*-PAH, and 8E11 mAbs. A negligibly small non-specific binding of Py molecule was only observed in the case of 8E11 mAb. However, selective excitation of 364.0 nm used to generate FLN spectra shown in the inset of Figure 3-4 (for the Py/8E11 mAb) did not reveal this contribution. Nevertheless, our NLN and FLN spectra did not reveal any non-specific binding of Py to the 4D5 and *anti*-PAH mAbs that are the focus of this work. This also proves that bovine IgG, 2E9 mAb, goat *anti*-horse polyclonal antibody preparation, and hydrophobic protein sites (like those of BSA) do not bind Py molecules. The latter indicates the aromatic character of the protein binding pocket is not a sufficient prerequisite to bind PAHs. Apparently, the protein-binding site has to complement the hapten with respect to other means of recognition and strong affinity binding (e.g. steric complementarity, sequence specificity, and possibly a suitable conformational diversity).

3.4.2 the Origin of Conformations I and II

The presence of two different Py populations in *anti*-PAH mAbs and only one population in 4D5 and 8E11 mAbs raises a very important question, namely, what is the origin of these two (0,0)-bands? Based on the above observations, we suggest the underlying mechanism that distinguishes these populations is the mode of binding. We propose that *anti*-PAH and 8E11 mAbs use π - π interactions (i.e. the binding to aromatic side chains from antibodies) and a π -cation interaction, whereas 4D5 mAb uses only π -cation interaction. The latter is consistent with the absence of aromatic side chains near the planar face of Py in 4D5 mAb. Since two modes of binding are possible in *anti*-PAH mAb, and the distribution of conformations I and II is slightly matrix dependent, one could suggest that at least in these two cases the pre-existing equilibrium model could contribute to their binding capabilities. However, all three mAbs must contain Arg and/or Lys that allow the unique locking of Py in conformation I. Thus it is feasible that in some mAbs, preexisting conformations could provide proteins the ability to acquire a new function and structure as recently suggested by Tokuriki and Tawfik [1]. The π -cation interaction must be caused by maintaining the orientation of the aromatic ring (the large π -plane of the Py ring) with respect to Arg and/or Lys present within the mAb binding pocket, thus leading to very small Γ_{inh} .

We hasten to add that very narrow ($\sim 75 \text{ cm}^{-1}$) origin bands were also observed for the (+)-*trans-anti*- and (-)-*trans-anti*-BPDE-dG adducts complexed with 8E11 mAb [23]. This significant reduction in spectral bandwidth suggested these two adducts are also bound tightly in

well-defined conformations within the binding pocket, so that molecular motion is restricted (as indicated by the reduced Γ_{inh} , i.e. a narrower distribution of the transition energies). In contrast, the narrowing effect was much less pronounced (i.e. FWHM of $\sim 115\text{-}125\text{ cm}^{-1}$) for the (+)-*cis-anti*- and (-)-*cis-anti*-BPDE-dG adducts [25]. Since the latter two adducts, based on molecular modeling, are more bulky [31], in this case, the binding most likely involves π - π interactions. This assignment was supported by observed variations in the frequencies of vibrational modes [23]. Finally, we note that π -cation interaction was also suggested to be important in the mAb B[a]P-13 (raised against B[a]P-butric acid) [32]. These authors suggested high susceptibility of the ELISA, with regard to inorganic ions, could indicate a more hydrophilic binding pocket, e.g. involving a π -cation interaction.

3.5 Conclusions

Our results support the findings of Pellequer *et al.* [12] who, based on original modeling studies, reported the first example of a π -cation interaction in which a bound neutral aromatic ligand (Py) was stabilized by a positively charged Arg side chain located in the deep binding pocket of a 4D5 mAb. Comparative studies of *anti*-PAH, 8E11, and 4D5 mAbs suggest the binding mode involves only π -cation interaction when the aromatic side chains are not available for antigen stabilization in antibody binding pockets. That is, in the case of conformation I, mAb must contain protons of Arg (and/or Lys) that are close to Py moiety, stabilizing its relative orientation and modifying Py vibrational frequencies. These data suggest simple spectroscopic measurements can be used to provide more insight into the mAb/hapten geometry and

operational mode(s) of binding. Further insight into the mode of binding could be provided by studying mAbs for which crystal structures are available, or via mutagenesis studies where the Lys and Arg side groups are eliminated from the Py binding site.

Acknowledgement

Our thanks are due to Professor Regina M. Santella (Columbia University, New York) for providing 8E11 mAbs and 4D5 mAb. We also acknowledge Dr. Nhan Dang and Mike Reppert for experimental help during the early stage of this project. This research was supported by the Johnson Center for Basic Cancer Research at K-State (Manhattan, KS).

References

- [1] Tokuriki, N., Tawfik, D. S., *Science* 2009, *324*, 203-207.
- [2] Webster, D. M., Henry, A. H., Rees, A. R., *Curr. Opin. Struc. Biol.* 1994, *4*, 123-129.
- [3] James, L. C., Tawfik, D. S., *Protein Sci.* 2003, *12*, 2183-2193.
- [4] Arevalo, J. H., Taussig, M. J., Wilson, I. A., *Nature* 1993, *365*, 859-863.
- [5] Chen, S. W. W., Van Regenmortel, M. H. V., Pellequer, J. L., *Curr. Med. Chem.* 2009, *16*, 953-964.
- [6] James, L. C., Roversi, P., Tawfik, D. S., *Science* 2003, *299*, 1362-1367.

- [7] Foote, J., Milstein, C., *Proc. Natl. Acad. Sci. U.S.A.* 1994, *91*, 10370-10374.
- [8] Pellequer, J. L., Chen, S. W. W., Keum, Y. S., Karu, A. E., Li, Q. X., Roberts, V. A., *J. Mol. Recognit.* 2005, *18*, 282-294.
- [9] Jankowiak, R., Rogan, E. G., Cavalieri, E. L., *J. Phys. Chem. B* 2004, *108*, 10266-10283.
- [10] Grubor, N. M., Hayes, J., Small, G. J., Jankowiak, R., *Proc. Natl. Acad. Sci. U.S.A.* 2005, *102*, 7453-7458.
- [11] Grubor, N. M., Liu, Y., Han, X. X., Armstrong, D. W., Jankowiak, R., *J. Am. Chem. Soc.* 2006, *128*, 6409-6413.
- [12] Pellequer, J. L., Zhao, B. T., Kao, H. I., Bell, C. W., Li, K., Li, Q. X., Karu, A. E., Roberts, V. A., *J. Mol. Biol.* 2000, *302*, 691-699.
- [13] Dougherty, D. A., Stauffer, D. A., *Science* 1990, *250*, 1558-1560.
- [14] Ma, J. C., Dougherty, D. A., *Chem. Rev.* 1997, *97*, 1303-1324.
- [15] Adak, S., Mazumder, A., Banerjee, R. K., *Biochem. J.* 1996, *314*, 985-991.
- [16] Jankowiak, R., Fundamental aspects of fluorescence line-narrowing spectroscopy, in: Gooijer, C., Ariese, F., Hofstraat, J. W. (Ed.), *Shpol'skii Spectroscopy and Other Site-Selection Methods*, John Wiley and Sons, Inc., New York 2000, pp. 235-271.
- [17] Ariese, F., Jankowiak, R., High-resolution fluorescence analysis of polycyclic aromatic hydrocarbon derived adducts to DNA and protein, in: Gooijer, C., Ariese, F., Hofstraat, J. W. (Ed.), *Shpol'skii Spectroscopy and Other Site-Selection Methods*, John Wiley and Sons, Inc., New York 2000, pp. 333-362.
- [18] Bader, A. N., Grubor, N. M., Ariese, F., Gooijer, C., Jankowiak, R., Small, G. J., *Anal. Chem.* 2004, *76*, 761-766.
- [19] Gomes, M., Santella, R. M., *Chem. Res. Toxic.* 1990, *3*, 307-310.

- [20] Santella, R. M., Lin, C. D., Cleveland, W. L., Weinstein, I. B., *Carcinogenesis* 1984, 5, 373-377.
- [21] Nakajima, A., *B. Chem. Soc. JPN.* 1971, 44, 3272-3277.
- [22] Kalyanasundaram, K., Thomas, J. K., *J. Am. Chem. Soc.* 1977, 99, 2039-2044.
- [23] Glushko, V., Thaler, M. S. R., Karp, C. D., *Arch. Biochem. Biophys.* 1981, 210, 33-42.
- [24] Jankowiak, R., Roberts, K. P., Small, G. J., *Electrophoresis* 2000, 21, 1251-1266.
- [25] Miksa, B., Chinnappan, R., Dang, N. C., Reppert, M., Matter, B., Tretyakova, N., Grubor, N. M., Jankowiak, R., *Chem. Res. Toxic.* 2007, 20, 1192-1199.
- [26] Chen, S. W. W., Pellequer, J. L., *Curr. Med. Chem.* 2004, 11, 595-605.
- [27] Humphrey, W., Dalke, A., Schulten, K., *J. Mol. Graph.* 1996, 14, 33-38.
- [28] Suh, M., Ariese, F., Small, G. J., Jankowiak, R., Liu, T. M., Geacintov, N. E., *Biophys. Chem.* 1995, 56, 281-296.
- [29] Wang, Y., Szczepanski, J., Vala, M., *Chem. Phys.* 2007, 342, 107-118.
- [30] Markushin, Y., Kapke, P., Saeed, M., Zhang, H., Dawoud, A., Rogan, E. G., Cavalieri, E. L., Jankowiak, R., *Chem. Res. Toxic.* 2005, 18, 1520-1527.
- [31] Xie, X. M., Geacintov, N. E., Broyde, S., *Biochemistry* 1999, 38, 2956-2968.
- [32] Scharnweber, T., Fisher, M., Suchanek, M., Knopp, D., Niessner, R., *Fresenius J. Anal. Chem.* 2001, 371, 578-585.

Chapter 4

Fluorescence line-narrowing difference spectra: dependence of Huang-Rhys factor on excitation wavelength

Chen Lin¹, Indrek Renge², and Ryszard Jankowiak^{1,3,*}

¹Department of Chemistry and ³Department of Physics, Kansas State University, Manhattan, KS 66506, USA

²Institute of Physics, University of Tartu, 142 Riia Street, EE51014 Tartu, ESTONIA

*On a sabbatical leave from K-State, Manhattan, KS 66506 (present address: Faculty of Applied Physics and Mathematics, Gdańsk University of Technology, Gdańsk, POLAND)
(submitted)

Abstract

It has been demonstrated theoretically that fluorescence line narrowing (FLN) difference spectra (Δ FLN spectra) reduce to single-site fluorescence line shape function in the low-fluence limit (M. Reppert, et al., *J. Chem. Phys.* 2010, 133, 014506). This finding is confirmed by the observation of different line shapes of FLN and Δ FLN spectra obtained for pyrene (Py) in ethanol glass at various excitation wavelengths using time-resolved fluorescence measurements. A peculiar dependence of the Huang-Rhys factor (S) on excitation wavelength was discovered, and discussed in terms of the solute-solvent, intermolecular Lennard-Jones potential. A V-shaped frequency dependence of the S -factor, also observed earlier for chlorin-doped 1-propanol glass (M. Rääsep, et al., *Chem. Phys. Lett.* 2009, 479, 140) suggests that the repulsive-dispersive potential is not sufficient to account for a complex “color effect”. At the high frequency edge the electron-phonon coupling is strongly enhanced by electrostatic interactions.

List of abbreviations

Δ FLN (Δ FLNS), delta/difference fluorescence line-narrowed (spectrum); BChl, bacteriochlorophyll; fwhm, full-width at half-maximum; EET, excitation/excitonic energy transfer; el-ph, electron-phonon; EtOH, ethanol; IDF, inhomogeneous distribution function; L-J, Lennard-Jones; PSB, phonon side band; Py, pyrene; S , Huang-Rhys factor; SHB, spectral hole-burning; ZPL, zero phonon line

4.1 Introduction

A delta fluorescence line-narrowed (Δ FLN) spectrum is the difference between two consecutive FLN measurements separated by a certain period of spectral hole-burning (SHB) [1-4]. In many cases [5-13], the localized exciton model introduced by Hayes et al. [14] is used to analyze the experimental fluorescence line-narrowing spectra. In this model, FLN and Δ FLN spectra can be expressed with one formula, i.e. the spectra are taken to be proportional to the same infinite sum:

$$FLN(\omega) \propto \Delta FLN(\omega) \propto \sum_{R=0}^{\infty} \sum_{P=0}^{\infty} \left(S^R \frac{e^{-S}}{R!} \right) \left(S^P \frac{e^{-S}}{P!} \right) \times \int_{-\infty}^{\infty} d\omega_{ZPL} N(\omega_{ZPL} - \omega_c) l_R(\omega - \omega_{ZPL} + R\omega_m) l_P(\omega_{exc} - \omega_{ZPL} - P\omega_m) \quad (4-1)$$

In the above equation, S is the Huang-Rhys factor measuring linear electron-phonon (el-ph) coupling strength; $N(\omega_{ZPL} - \omega_c)$ stands for the inhomogeneous site-distribution function (IDF) of the pigment zero-phonon line (ZPL) frequencies; $l_0(\omega)$ is a Lorentzian function representing the ZPL, while $l_{R(P)}(\omega)$ is the R - (P -) phonon profile for $R, P > 0$. This formula is widely used, as the

Δ FLN signal corresponds to the FLN spectra of pigments burned away during the hole-burning (HB) process. Therefore, the authors argued [5-13] that Eq. (4-1) for FLN spectra can also be applied to Δ FLN measurement. However, this could be questioned when comparing Eq. (4-1) to the theory developed by Fünfschilling, et al. [4]. According to Fünfschilling's analysis, the contribution from pseudo- and multi-PSB (terms with $R > 0$ in formula (4-1)) should be negligible at low-burn fluence (hole depth less than 10% of ZPL absorbance; burn fluence measures light dose on unit area used for HB process of the sample in the unit of $\text{J}\cdot\text{cm}^{-2}$). However, Eq. (4-1) clearly indicates that the terms with $R > 0$ are significant at any burn fluence.

To better understand this contradiction, Reppert, et al. [15] derived the lineshape function of Δ FLN spectra. Under the assumption that the system is excited by a laser with an infinitely narrow line width, a Δ FLN spectrum can be described as

$$\begin{aligned} \Delta FLNS(\omega) &\propto F * [A_B \cdot (N - N_o - N_1)] \\ &\propto F * (k \cdot N \cdot A_B^2 - N_1 \cdot A_B) \end{aligned} \quad (4-2)$$

In this formula, F stands for a single-site fluorescence spectrum; $*$ means convolution; N is the IDF of pigments before burning as above; N_1 and N_o are IDFs of burned and unburned pigments after HB has taken place, respectively; A_B is the reflection of the single-site absorption line shape function around burn frequency ω_B ; k is a constant that depends on the properties of the system, burn fluence, and average HB quantum yield. (For detailed derivation of Eq. (4-2) see Ref. [15]). Numerical calculations shown in Ref. [15] demonstrated that the term inside the brackets in Eq. (4-2) resembles delta function, resulting in a Δ FLN spectrum similar to the fluorescence line shape function, with ZPL centered at the excitation wavelength, as shown by Eq. (4-3):

$$\Delta FLNS(\omega) \approx F(\omega) * \hat{\delta}(\omega - \omega_B) = F(\omega - \omega_B). \quad (4-3)$$

Fitting the ΔFLN spectrum with formula (4-1) will underestimate the contribution of real PSB, as well as the value of the Huang-Rhys factor.

In order to experimentally test the conclusions (Eq. (4-3)) drawn in Ref. [15], ΔFLN spectra were measured for a simple system (i.e., pyrene embedded in the ethanol glass; concentration $\sim 10^{-5}$ M). We show that S varies across the inhomogeneously broadened absorption band. The frequency-dependent S -factor is discussed in terms of the model developed by Lennard-Jones (L-J) model of intermolecular, repulsive-dispersive potential [16-19]. Although the frequency dependence of linear electron-phonon (el-ph) coupling strength follows from the L-J model [18,19], the observed color effect behaves differently, as compared to the prediction. Data obtained for pyrene (Py) in ethanol glass in this work and chlorin-doped 1-propanol reported in [10] show an increase of S at smaller vacuum-to-matrix shifts that is not compatible with repulsive-dispersive potential [19]. Electrostatic interactions between the polar solvent and the chromophore, which could lead to enhanced electron phonon coupling strength at the edges of IDF, are not included in the simple L-J model.

4.2 Experiments

For FLN measurements, a Lambda Physik Lextra 100 XeCl excimer laser was used as a pump source for a Lambda Physik FL 2002 Scanmate tunable dye laser system (10 Hz). The resolution for FLN was ± 0.02 nm (dye laser line width 5 GHz). A 1-m McPherson monochromator (model 2601, slit width 50 μ m) with 2400/mm grating and a Princeton

Instruments photodiode array were used for dispersion and detection of fluorescence. The corresponding accuracy in frequencies for FLN measurements was about $\pm 2 \text{ cm}^{-1}$. In order to minimize scattered light from the laser, a Princeton Instruments FG-100 pulse generator was used for time-resolved spectroscopy, with a detector delay time of 40 ns and a gate width of 200 ns. For all spectroscopic measurements, 30 μL of Py in ethanol (concentration 10^{-5} M , $\sim 0.86 \text{ O.D.}$ at 334 nm and $< 0.1 \text{ O.D.}$ at (0,0)-transition) was placed in a quartz capillary tube with $\sim 2.5 \text{ mm}$ inner diameter and immersed in a helium cryostat with quartz optical windows. All fluorescence spectra were collected with 30 s acquisition time (equals to burn fluence $\sim 12.5 \text{ J}\cdot\text{cm}^{-2}$).

4.3 Results

Results of the experiment are shown in Figures 4-1 and 4-2. The fluorescence origin band (thick gray line) and FLN spectra (colored curves) of Py in ethanol glass at temperature $T = 5 \text{ K}$ were obtained for five laser excitations within the 0-0 origin band (see figure caption for details). To ensure that scattered-light intensity does not contribute to resonant ZPLs, the spectra were obtained using time-resolved measurements. The FLN spectra shown in the main frame of Figure 4-1 show the same trend as the calculation in Figure 3 of Ref. [15]. That is, at the high-energy side across IDF, FLN spectra have significant contributions from non-resonant excitation, as broad and intense “wings”. The inset shows pre-burn (black), and post-burn (blue) FLN spectra, and the resulted ΔFLN spectrum (red), which is obtained as a difference.

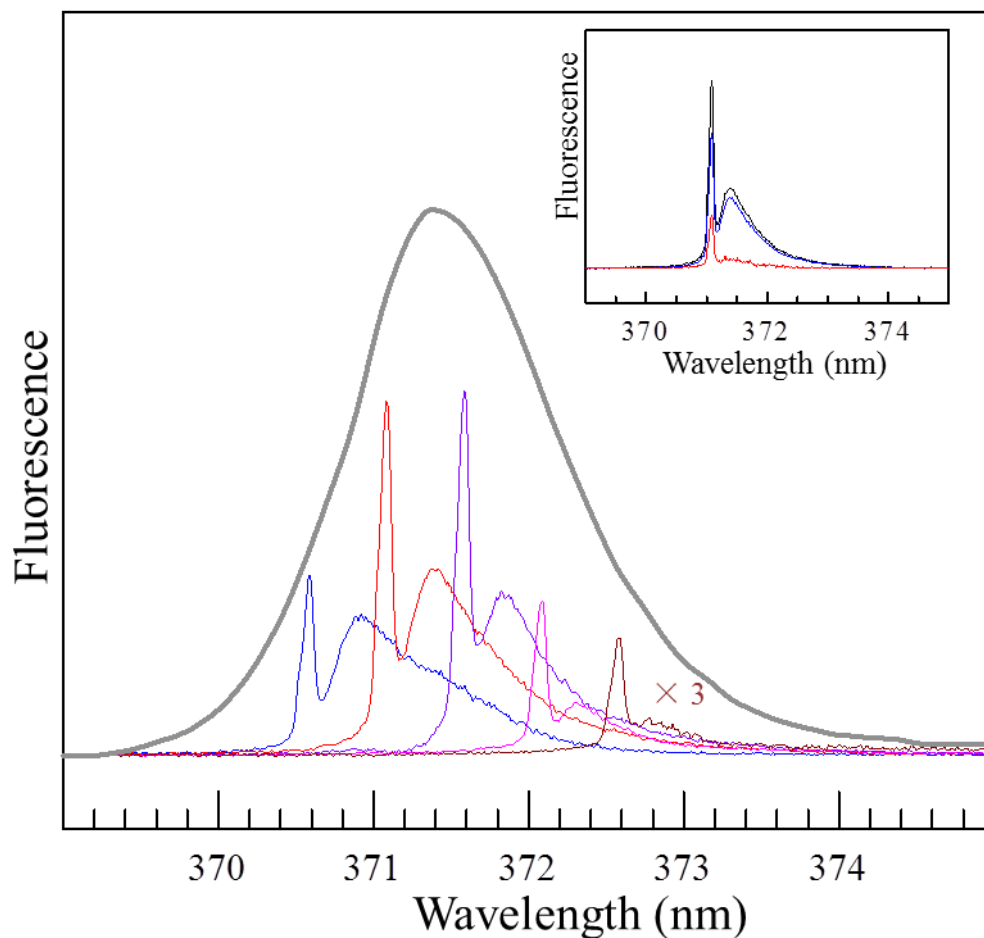


Figure 4-1. FLN spectra of Py in ethanol glass at $T = 5$ K. Colored lines are spectra collected with excitation wavelengths at 370.58, 371.08, 371.58, 372.08, and 372.58 nm, respectively. The thick gray curve is bulk emission, excited non-selectively at λ_{ex} of 308 nm. In the inset, black line stands for the pre-burn FLN spectrum, and the blue curve is the post-burn FLN measurement. The red curve is the difference between the two. The gate width is 200 ns, and delay time is 40 ns.

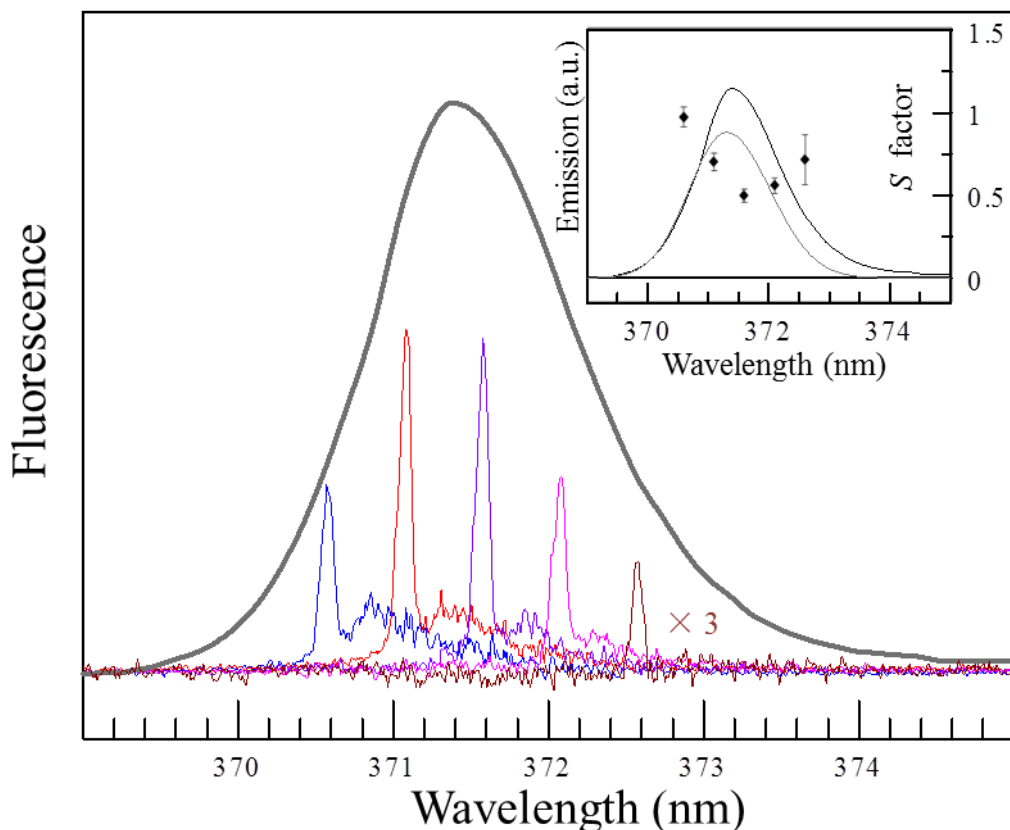


Figure 4-2. Fluorescence origin ($\lambda_{\text{ex}} = 308$ nm, thick gray line) and resonantly excited Δ FLN spectra (colored curves) of Py in ethanol glass at $T = 5$ K, obtained at various excitation wavelengths (see Figure 4-1) using time-resolved measurements. The inset compares the 0-0 emission band (black) with a Gaussian fit of the IDF, shown in gray. The frequency-dependent S factor is plotted as a function of excitation wavelength (filled diamonds).

Table 4-1. Apparent Huang-Rhys factor values at different wavelengths for pyrene in EtOH glass at 5 K.

Wavelength (nm)	Solvent shift $\Delta\nu$ (cm^{-1}) ^a	Huang-Rhys factor S	Debye-Waller factor α ($\alpha = \exp(-S)$)
370.58	-225 ± 5	0.96 ± 0.06	0.38
371.08	-260 ± 5	0.69 ± 0.05	0.50
371.58	-295 ± 5	0.49 ± 0.04	0.61
372.08	-330 ± 5	0.55 ± 0.04	0.58
372.58	-370 ± 5	0.70 ± 0.15	0.50

^aRelative to 0-0 origin of Py in the cold jet at 27208 cm^{-1} from Ref. [20].

The corresponding Δ FLN spectra are displayed in Figure 4-2. Frequency-dependent S factors (see Table 4-1) are plotted as a function of excitation wavelength (diamonds in the insert of Figure 4-2). It is obvious that the line shape of Δ FLN spectra significantly differ from corresponding FLN spectra, i.e. FLN signals and Δ FLN signals collected under the same conditions are not proportional to each other. This strongly suggests that formula (1) is not applicable to Δ FLN signals. Therefore, collected Δ FLN spectra may be similar to the single-site emission line shape, which is suggested by Ref. [15]. The apparent values of S factors calculated from Δ FLN spectra in Figure 4-2 are shown in Table 4-1. The S factor reaches a minimum value (0.49) close to the band maximum at $\lambda_{\text{ex}} = 371.58$ nm, and increases when the excitation wavelengths are shifted towards the edges of IDF. The S values are reproducible, and a similar dependence on wavelength was collected when repeating the measurement (data not shown). The Δ FLN signal is usually much weaker than corresponding FLN spectrum due to the subtracting process. In particular, the Δ FLN signal recorded on the red edge at 372.58 nm is very weak with a low signal-to-noise ratio, leading to a much larger uncertainty in the S factor at the long-wavelength side of the band.

4.4 Discussion

4.4.1 Challenges in Measuring the S -Factor

In order to determine the real shape of resonant FLN spectra, one has to eliminate a strong background of scattered exciting light, which overlaps with ZPL. For systems with long

luminescence lifetimes, a continuous-wave (CW) laser with a chopper, or a pulsed laser, can be used, along with a time-gated detection, which can collect emission signals after termination of the excitation pulse. If the fluorescence lifetime is short (e.g., for many photosynthetic complexes, the fluorescence lifetime of chlorophylls or bacteriochlorophylls is in the order of a few nanoseconds), the time-delay measurement using a 10-ns pulse laser is not applicable. In this case, Δ FLN measurement is necessary to remove the scattered light (which is extremely difficult in experiments) for correct determination of ZPLs, e.g. as shown in [5-13,19]. This method requires the fluctuation of laser intensity in FLN measurements be negligible compared to the Δ FLN signal, i.e., the scattering contribution must be much smaller than the real signal in the total spectrum. In addition, for better determination of system parameters in Δ FLN measurement, burn fraction should be less than 10% [15]. This is why we selected a system (i.e., Py molecules in ethanol glass) with a large fluorescence quantum yield ($\phi_{fl} = 0.65-0.92$) and relatively long fluorescence lifetime ($\tau_{fl} = 515$ ns) [21]. In this case, time-resolved detection is possible and Δ FLN spectra can be easily measured without light-scattering contributions at ZPLs.

4.4.2 Effect from Line Width of ZPL and Excitation Laser

Formula (4-2) only describes the line shape of Δ FLN with infinitely narrow line width of the excitation light source [15]. For finite laser line width, A_B in Eq. (4-2) should be replaced by convolution $l(\omega)*A_B$, where $l(\omega)$ is an arbitrary laser line shape function. However, it was demonstrated that for laser line width ≤ 0.1 cm^{-1} , Eq. (4-3) is still a good approximation [15]. Reppert, et al. [15] also indicated that excitation line width of ~ 0.5 cm^{-1} , often used in

experimental studies [5-13,19] does not affect the shape of recorded Δ FLN spectra, though some aberrations may appear, in particular for high-frequency excitations. However, when laser line width is larger than $\sim 1 \text{ cm}^{-1}$, the approximation to Eq. (4-3) breaks down, especially on the high-energy side of IDF, where pseudo-PSB terms have larger contributions to the total fluorescence spectrum. The laser used in this experiment has a line width of 5 GHz, and meets the requirement from Ref. [15]. Though the experiment in this part has limited instrument resolution ($\sim 2 \text{ cm}^{-1}$), this only results in a broader and less-intense ZPL, which has the same integrated intensity as the real ZPL (which should be sharper with relatively larger intensity than ZPLs shown in Figures 4-1 and 4-2). The latter, however, does not affect the determination of the S factor.

4.4.3 On Spectroscopy of Pyrene

Besides the Py/EtOH system, frequency dependent zero phonon transition probabilities have been reported for chlorin in *n*-propanol [10], and chlorophylls in different matrices [7,10,19], including proteins [5-9,11,13]. Other “color effects” are well documented in HB spectroscopy, when persistent spectral holes were subject to external electric field [22], pressure [16], and temperature [16,23], but remain incompletely understood. The frequency dependence of S is in a sense more subtle, since variability in the homogeneous spectral shape is revealed. The key to color effects is hidden in the solute-solvent interactions in the ground and excited states of impurity, causing microscopic solvent shifts on a single molecule level, leading finally to broad inhomogeneous band shapes.

The pure electronic transition energy of free, non-solvated molecule can serve as a reference state to solvent shifts. The 0-0 origin of Py in cold, supersonic jet is known to occur at 27208 cm^{-1} [20] or 27216 cm^{-1} [24]. The difference is close to refractive index (n) correction of air [25]. Our fluorescence band maximum in EtOH is red shifted by -280 cm^{-1} and has a full-width at half-maximum (fwhm) of 120 cm^{-1} . The maximum position is in accordance with dispersive shift coefficient p of -1160 cm^{-1} [26] and the Lorenz-Lorentz function $((n^2 - 1)/(n^2 + 2))$ of ethanol glass (~ 0.3). The polarizability difference between the ground and the excited state $\Delta\alpha$ has been estimated from p as $4.7 \pm 2\text{ \AA}^3$ [26].

The lowest singlet transition (S_1) in Py is weak, α -type (1L_b), in contrast to much more intense p (1L_a) bands occurring in anthracene, terylene, etc. Because of relatively small dispersive solvent shift, the absorption bands (more correctly, the IDFs) of α -type transitions are not expected to be symmetric Gaussians. A steeply rising short-wavelength slope is already visible in the room temperature spectra of Py (also benzene, naphthalene and phenanthrene, etc.), particularly for less polar liquids. The lack of symmetry of the non-selectively excited, broad fluorescence band shown in Figures 4-1 and 4-2 may, in part, be due to el-ph coupling, but there is no *a priori* reason to assume a Gaussian distribution. Asymmetric IDF and its transformation under pressure has been dealt with in terms of Lennard-Jones potentials (L-J) that take into account exchange repulsion and dispersive attraction between the molecules [17].

Because of inversion symmetry, Py is devoid of dipole moments in any electronic state that appear to preclude electrostatic interactions (except for polarization by matrix dipoles that we consider separately from electrostatics). However, aromatic molecules possess quadrupole

moments, and upon excitation charges will be redistributed [27]. For example, anthracene and Py were compared in two solvent glasses with the same refractive index, apolar 1,3-dimethylcyclohexane and propylene carbonate [28]. In Py, a moderate red shift of about -20 cm^{-1} and broadening of IDF of similar magnitude occurs in the latter highly polar glass. The matrix sensitivity of strong p band in anthracene is five times higher. The shift of IDF can be due to polarization (that causes a red shift, since $\Delta\alpha > 0$) or the reaction field of dye. In our view, the reaction field is a fictitious field characterizing electrostatic stabilization of solute particle in polar surroundings. Depending on the sign of the change in dipole (multipole) moments on excitation, either a red or a blue shift can arise [27]. Finally, stochastic distribution of charges in the environment (the random “cavity field”) produces both red and blue shifts with equal probability that solely results in broadening. The capability of solvent dipoles to broaden the IDF is very conspicuous even in case of centrosymmetric chromophores [28].

Another useful comparison can be made between broad fluorescence band of Py, peaking at 371.4 nm in EtOH (Figures 4-1 and 4-2) and sharp Shpol’skii multiplet lines at 371.7 and 372.6 nm in crystalline n -hexane matrix at 5 K [29]. There is negligible fluorescence (and absorption) below 371 nm in the Shpol’skii crystal. Therefore, the extension of spectrum in EtOH to the blue must either be due to Coulomb interactions and/or a decreased solvent packing density that reduces dispersive red shift. Notice that average refractive index of EtOH glass and n -hexane crystal is very similar [30].

In a glass, every Py molecule has a unique solvent surrounding and solvent shift. Moreover, individual molecules may have different transition probability that correlates with

positions of atomic charges in the matrix. Because of forbidden character, the intensity of the 0-0 band is strongly modulated by the environment that has been utilized for definition of a “polarity” scale of liquids (the Py scale) [31]. Obviously, every impurity center in a glass can be coupled to a different set of local phonons.

Finally, each Py molecule has its own hole-burning characteristics. Protic matrix is necessary in order to enable HB in polyarenes [16]. Photophysical HB is a highly dispersive process, associated with proton tunneling (strong isotope effect) in hydrogen bonding networks of the solvent [32]. When recording Δ FLN spectra, the most facile burning Py centers are addressed that may not have the same S as the more passive ones left unburned. Nevertheless, the V-shaped frequency dependence constitutes a color effect requiring explanation.

4.4.4 Intermolecular Repulsive-Dispersive Potentials: Variation of S within IDF

A simple rationalization of frequency dependent Huang-Rhys factor within IDF has been proposed recently [18,19]. As compared to crystals, glasses possess high potential energy, emerging as a result of unfilled space. The Boltzmann equation would describe the distribution of ground-state potential energy of a chromophore and its closest solvent layer:

$$\Phi(r) = e^{(-U_g/k_B T_g)}. \quad (4-4)$$

In Eq. (4-4), $\Phi(r)$ is a function of intermolecular coordinate r ; U_g (or $U_g(r)$) stands for the potential curve; $k_B T_g$ is thermal energy at the glass transition temperature (T_g). In Refs. [16-19], U_g obeyed a Lennard-Jones (L-J) 6-12 function, instead of a harmonic potential. Thus, for the

ground state, with a potential curve whose well depth is $-\varepsilon_g$ and equilibrium distance is σ_g , U_g can be expressed as

$$U_g = \varepsilon_g \left[\left(\sigma_g / r \right)^{12} - 2 \left(\sigma_g / r \right)^6 \right]. \quad (4-5)$$

Potential curve U^* for excited state has the same form:

$$U^* = \varepsilon^* \left[\left(\sigma^* / r \right)^{12} - 2 \left(\sigma^* / r \right)^6 \right]. \quad (4-6)$$

In Eq. (4-6), $-\varepsilon^*$ and σ^* are well depth and equilibrium distance for the excited state, respectively. The difference between U_g and U^* is the solvent shift of optical transition energy $\Delta v(r)$.

The Franck-Condon principle suggests that linear el-ph coupling strength would be proportional to the potential minima shift between ground and excited states. Meanwhile, according to Hooke's law, the hypothetic force (first derivative of potential curve with respect to r , U_g' and U^{*}' for ground and excited state, respectively), which drives the guest-host system toward the equilibrium position, is directly related to the value $(r - \sigma)$. Therefore, neglecting quadratic el-ph coupling, the S factor can be correlated with the difference of U_g' and U^{*}' as

$$S \propto \left| U_g' - U^{*}' \right|. \quad (4-7)$$

The IDF is simply obtained by plotting $\Phi(r)$ versus solvent shift $\Delta v(r)$, and thereafter the frequency dependence of the S -factor can be built as a function of $\Delta v(r)$. Almost proportional dependence between S and Δv has been calculated [18,19], in contrast to the present experiment. In L-J model, properties of functions $|U_g' - U^{*}'|$ and $\Delta v(r)$ strongly depend on the relative values of ε_g and ε^* , and, especially on equilibrium distances σ_g and σ^* . In a realistic system, the pressure and thermal shift behavior suggests that excited state has a smaller radius in case of

π -transitions in large molecules. In addition, solvent shift studies reveal that fluorescence has slightly larger dispersive shift coefficients than absorption (when measured in liquid *n*-alkanes [26], unpublished), which means that the solute-solvent interaction distance has decreased. In other words, σ^* should be smaller than σ_g .

The well depth is related to polarizabilities, according to London formula for dispersive interactions. From the polarizability of Py $\alpha_g = 28 \text{ \AA}^3$ [25] and its change on excitation $\Delta\alpha$ of $4.7 \pm 2 \text{ \AA}^3$ [26], we obtain that $\varepsilon^*/\varepsilon_g \sim 1.1$. Because of repulsive branch in Eq. (5), the well depth is only a half of dispersive attraction energy. As for the relative shift of potential minima σ^*/σ_g , three physically meaningful intervals are discussed, defined as $\sigma^*/\sigma_g = (\varepsilon^*/\varepsilon_g)^{-1/6} = 0.984$, $(\varepsilon^*/\varepsilon_g)^{-1/6} < \sigma^*/\sigma_g = 0.988 < (\varepsilon^*/\varepsilon_g)^{-1/12}$, and $\sigma^*/\sigma_g = (\varepsilon^*/\varepsilon_g)^{-1/12} = 0.992$ (in case of $\varepsilon^*/\varepsilon_g \sim 1.1$ in Py/EtOH system). Notice that for σ^*/σ_g equal to $(\varepsilon^*/\varepsilon_g)^{-1/6}$ (Figure 4-3B) or $(\varepsilon^*/\varepsilon_g)^{-1/12}$ (Figure 4-3D), several expressions derived from L-J potentials are simplified [16]. For a more general case in less polar systems shown in Figure 4-3C ($\sigma^*/\sigma_g = 0.988$), σ^*/σ_g should meet the requirements that $(\varepsilon^*/\varepsilon_g)^{-1/6} < \sigma^*/\sigma_g < (\varepsilon^*/\varepsilon_g)^{-1/12} < 1$ (This is derived from equation (14) in [16] under the following three criterions: i). in many less-polar systems, the experimental a values lie between $2\beta_T$ and $4\beta_T$; ii). $\varepsilon^*/\varepsilon_g \sim 1.1$; iii). $\sigma^* < \sigma_g$) [16]. The well depth, estimated from the enthalpy of sublimation, is about 50 kJ/mol [33], and organic solvents have glass points at several hundred K. Therefore, in molecular glasses ε_g exceeds $k_B T_g$ by a factor of ~ 20 . Insert in Figure 4-3A shows the $\Phi(r)$:

$$\Phi(r) = \exp(-20((1/r)^{12} - 2(1/r)^6 + 1)) \quad (4-8).$$

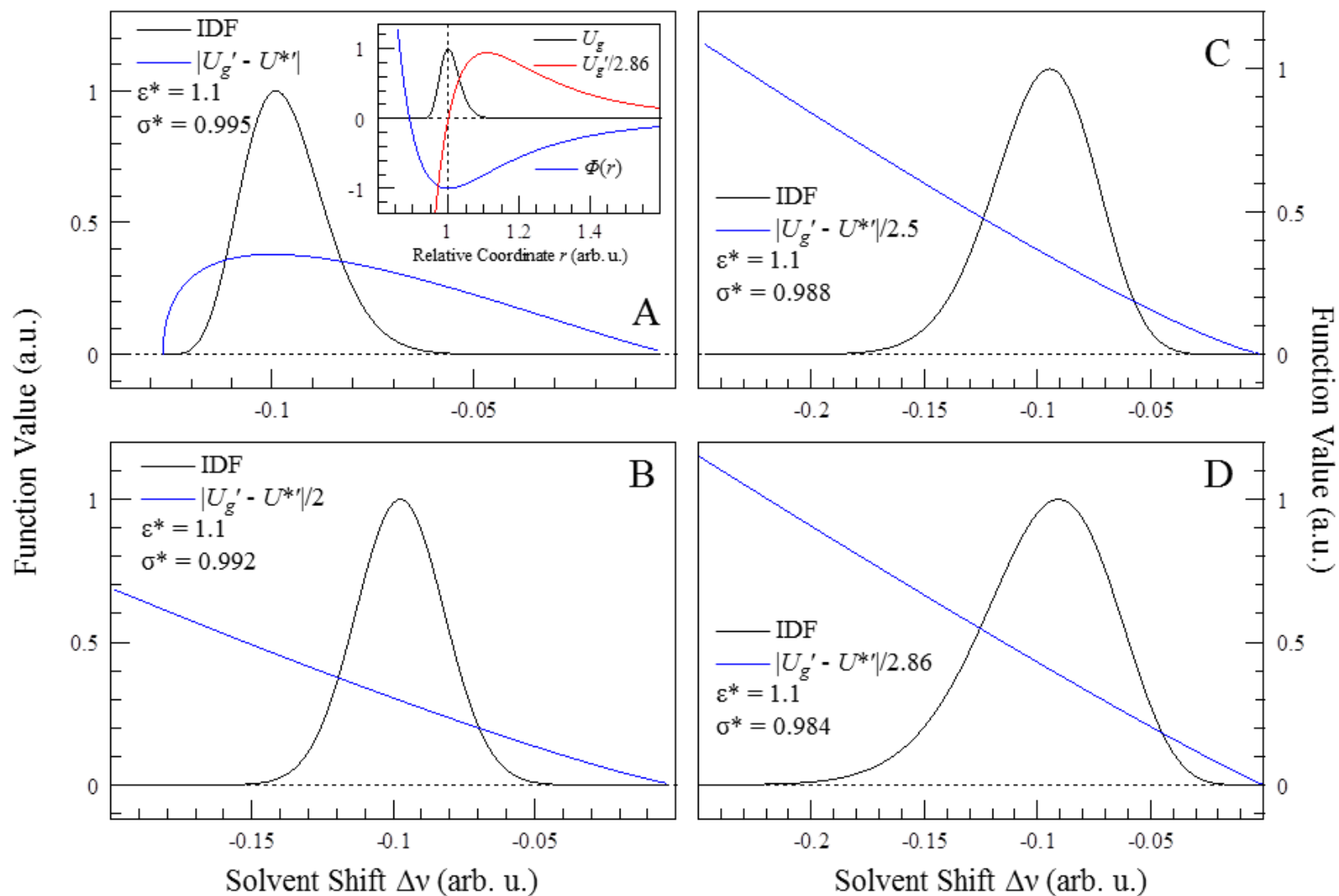


Figure 4-3. Calculated inhomogeneous band (IDF) and the dependence of absolute difference between the first derivatives U_g' and U^{*} vs the solvent shift; $\epsilon_g = \sigma_g = 1$, $\epsilon^* = 1.1$, and $\sigma^* = 0.995$ (A), 0.992 (B), 0.988(C), and 0.984 (D). Inset shows the Lennard-Jones 6-12 function U_g (Eq. (4-5); $\epsilon_g = \sigma_g = 1$), U_g' , and the Boltzmann distribution $\Phi(r)$ (Eq. (4-8)).

In order to obtain the IDF, $\Phi(r)$ is plotted versus $\Delta v(r)$ ($= U^* - U_g$) for different relative shifts of minima as indicated in Figure 4-3 A-D. The solvent shift is negative (to the red), as expected from a deeper well in the excited state. At the largest displacement (panel D), desirable asymmetry of IDF is reproduced, characteristic for α -type transitions. The calculated fwhm to solvent shift ratio (0.68) exceeds fwhm/ Δv of Py fluorescence (0.40), but it can be adjusted by compressing $\Phi(r)$, e. g. when lowering the well depth against thermal energy at the glass point $\varepsilon_g/k_B T_g$. The difference of returning forces (Eq. (4-7)), assumed proportional to linear el-ph coupling constant are approximately proportional to solvent shifts in Figure 4-3 B to D, in contrast to the observed behavior of S -factor. Indeed, mathematical calculations show that in less polar system with $(\sigma^*/\sigma_g)^{12} \leq (\varepsilon^*/\varepsilon_g)^{-1} \leq (\sigma^*/\sigma_g)^6 < 1$, $\Delta v(r)$ ($= U^* - U_g$) is no larger than 0, and $|U_g' - U^{*'}|$ decreases with increasing $\Delta v(r)$, as shown by Figure 4-3B to 4-3D. However, Py-doped EtOH glass cannot be simply categorized into “less polar system”, i.e., σ^*/σ_g values which don't meet the criteria mentioned above can be chosen. For example, if the excited potential shift is very small ($\sigma^*/\sigma_g = 0.995$), S is no longer a monotonic function of $\Delta v(r)$. Weak coupling is expected on the band edges that is just the opposite to V-shaped experimental dependence of S over the inhomogeneous band. Also the band shape with a shallow slope towards high frequencies is unrealistic (Figure 4-3A).

Therefore, the model should be extended beyond (isotropic) repulsive-dispersive interactions. Consideration of electrostatic interactions may seem straightforward. The el-ph coupling strength should depend on the change of Coulomb forces upon excitation of the solute, similar to that of L-J case. Stockmayer potential, containing the dipole-dipole interaction [34,35],

is not directly applicable to of Py, devoid of dipole moment. A quantum mechanical investigation of charge redistribution of Py in the S_1 state, in conjunction with molecular mechanics modeling of solute-solvent interactions is required. In this report we restrict ourselves to a qualitative reasoning.

As demonstrated in [15], the S factors calculated by fitting Δ FLN spectra with Eq. (4-1) are artificially lowered [5-13], in particular on the high-energy side of the IDF. This is illustrated in Figure 4-4B, which includes an additional example taken from Ref. [10]. Blue triangles stand for the S factor directly from Δ FLN spectra, while red squares show the S factor calculated by fitting Δ FLN spectra with Eq. (4-1). It is obvious from this frame that the S value is artificially lowered. This also leads to misinterpretation of the dependence of S on excitation energy. Besides, the behavior of S across the IDF is also affected by delocalized exciton and inter-pigment excitation energy transfer. For example, decreasing S with increasing excitation frequency was observed in Fenna-Mathews-Olson (FMO) photosynthetic protein with bacteriochlorophylls a (BChl a) [8], and it was assumed that the L-J model is not applicable to this system behavior due to the presence of excitation energy transfer [19]. However, other chlorophyll a [9,10] or BChl a [13,19] containing solvent glasses [10,19] or proteins [9,13] show approximate proportionality between the el-ph coupling strength and absolute solvent shift, as expected from the L-J model. Remarkably, the dispersive shift coefficients, $-p$ are larger for S_1 transitions of chlorophylls ($1300 - 1500 \text{ cm}^{-1}$) [36], as compared to parent chlorin (660 cm^{-1}) and Py (1160 cm^{-1}) [26].

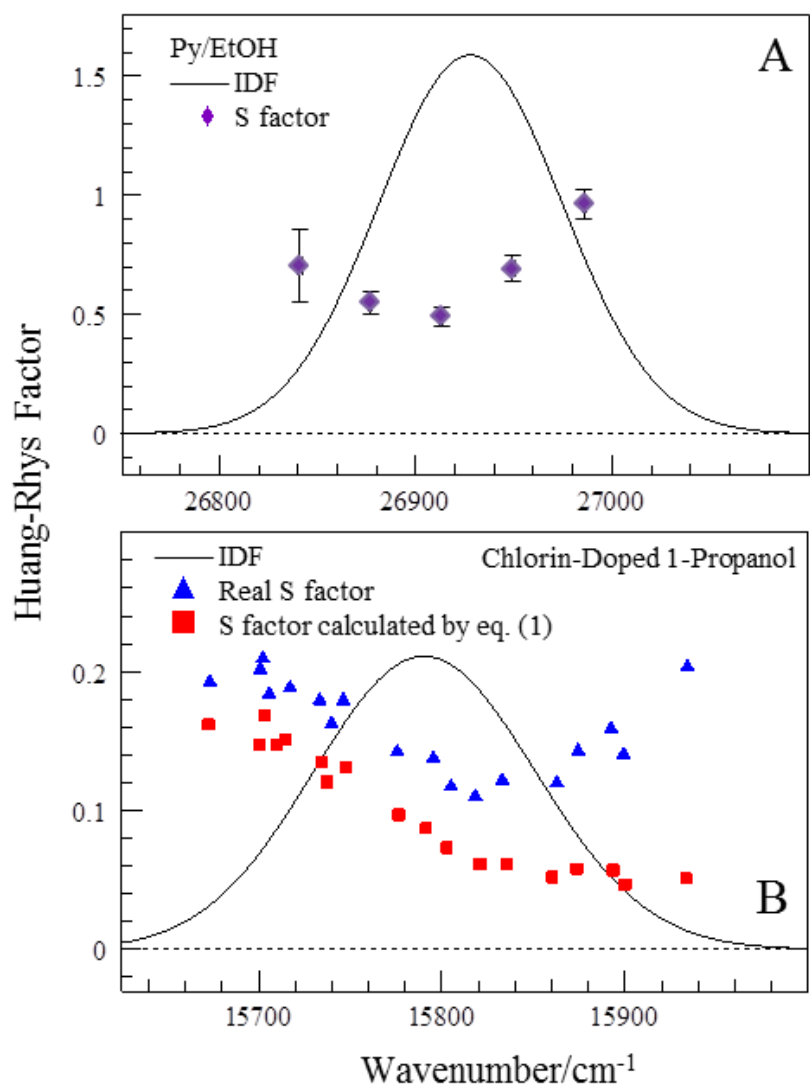


Figure 4-4. Frame A: S -dependence on frequency of Py in EtOH. Frame B: S -dependence on frequency of chlorin-doped 1-propanol (adopted from Ref. [10]). Note that frequency increases from left to right.

In order to better understand the experimental results shown in Figure 4-4A (Py/EtOH in this work) and 4-4B (chlorin-doped 1-propanol glass from Ref. [10]), note that highly polar solvents were used in these two cases. Electrostatic interactions in this kind of matrix may contribute to solvent shift, and particularly strongly, to broadening [28]. More generally, molecules absorbing at the very edges of IDF are subject to high fields or extreme (internal) pressures. In addition, because of additive effects of strong field and compression (packing density), strong increase of S factor on the red edge of IDF can be expected. Thus, the interplay between electrostatic and dispersion interactions may lead to a V-shaped S dependence within IDF.

4.5 Conclusions

Every individual molecule in a glass has its own spectral, photophysical and photochemical properties, because of unique microenvironment. This is particularly true in case of forbidden S_1 transition in pyrene embedded in polar and protic EtOH glass. As a first approximation, the homogeneous spectrum has been assumed to be independent on the 0-0 frequency [1-4,15]. Actually, the linear el-ph coupling strength S is variable and correlated with absolute vacuum to matrix shift $\Delta\nu$. The Py/EtOH system has a weak el-ph coupling, with average number of excited modes S varying from 0.5 to 1. The shape of Δ FLN spectrum is very similar to single-site fluorescence line shape function with ZPL centered at the excitation wavelength, in accordance to Refs. [1-4,15]. The Lennard-Jones model, describing purely repulsive-dispersive potential [16-19], cannot explain a V-shaped frequency dependence of the

el-ph coupling in polar glasses, such as Py in ethanol and chlorine-doped 1-propanol glass [10]. Strong electrostatic interaction that is not included in the L-J model can affect the solute molecules absorbing at the wings of IDF, enhancing the strength of el-ph coupling.

Acknowledgments

This work was supported by the Chemical Sciences, Geosciences and Biosciences Division, Office of Basic Energy Sciences, Office of Science, U.S. Department of Energy (grant EC9987 to RJ). Dr. Indrek Renge was supported by the Estonian Science Foundation Grant no. 8369. We are grateful to Dr. Margus R äsep and Mike Reppert (MIT) for discussions.

Reference

- [1] Bogner, U., Schwarz, R., *Phys. Rev. B* 1981, *24*, 2846-2849.
- [2] Yaaniso, R. V., *Proc. Acad. Sci. Estonian SSR Phys. Math.* 1985, *34*, 277-283 (in Russian).
- [3] Yaaniso, R. V., *J. Appl. Spectrosc.* 1986, *44*, 365-370.
- [4] Fünfschilling, J., Glatz, D., Zschokkegranacher, I., *J. Lum.* 1986, *36*, 85-92.
- [5] R äsep, M., Freiberg, A., *Chem. Phys. Lett.* 2003, *377*, 371-376.
- [6] Timpmann, K., R äsep, M., Hunter, C. N., Freiberg, A., *J. Phys. Chem. B.* 2004, *108*, 10581-10588.

- [7] R äsep, M., Hunter, C. N., Olsen, J. D., Freiberg, A., *Photosynth. Res.* 2005, 86, 37-48.
- [8] R äsep, M., Freiberg, A., *J. Lum.* 2007, 127, 251-259.
- [9] R äsep, M., Pieper, J., Irrgang, K.-D., Freiberg, A., *J. Phys. Chem. B.* 2008, 112, 110-118.
- [10] R äsep, M., Pajusalu, M., Freiberg, A., *Chem. Phys. Lett.* 2009, 479, 140-143.
- [11] Pieper, J., R äsep, M., Irrgang, K.-D., Freiberg, A., *J. Phys. Chem. B* 2009, 113, 10870-10880.
- [12] R äsep, M., Linnanto, J., Freiberg, A., *J. Chem. Phys.* 2009, 130, 194501-194501.
- [13] Freiberg, A., R äsep, M., Timpmann, K., Trinkunas, G., *Chem. Phys.* 2009, 357, 102-112.
- [14] Hayes, J. M., Gillie, J. K., Tang, D., Small, G. J., *Biochim. Biophys. Acta* 1988, 932, 287-305.
- [15] Reppert, M., Naibo, V., Jankowiak, R., *J. Chem. Phys.* 2010, 133, 014506-1-9.
- [16] Renge, I., *J. Phys. Chem. B* 2004, 108, 10596-10606.
- [17] Renge, I., van Grondelle, R. J., Dekker, P., *Biophys. J.* 2007, 93, 2491-2503.
- [18] Renge, I., *J. Lum.* 2008, 128, 413-420.
- [19] Renge, I., R äsep, M., Freiberg, A., *J. Lum.* 2011, 131, 262-265.
- [20] Ohta, N., Baba, H., Marconi, G., *Chem. Phys. Lett.* 1987, 133, 222-229.
- [21] Murov, S. L., Carmichael, I., Hug, G. L., *Handbook of Photochemistry*, 2nd ed., Marcel Dekker, New York 1993.
- [22] Kador, L., Jahn, S., Haarer, D., Silbey, R., *Phys. Rev. B* 1990, 41, 12215-12226.
- [23] Renge, I., *Phys. Rev. B* 2003, 68, 064205-1-9.
- [24] Mangle, E. A., Topp, M. R., *J. Phys. Chem.* 1986, 90, 802-807.

- [25] Lide, D. R. (Ed.), *CRC Handbook of Chemistry and Physics, 89th ed.*, CRC Press, Boca Raton, 2008.
- [26] Renge, I., *Chem. Phys.* 1992, *167*, 173-184.
- [27] Renge, I., *J. Photochem. Photobiol. A.: Chem.* 2012, *239*, 7-16.
- [28] Renge, I., Wild, U. P., *J. Lum.* 1996, *66&67*, 305-309.
- [29] Nakhimovsky, L. A., Lamotte, M., Jussot-Dubien, J., *Handbook of Low Temperature Electronic Spectra of Polycyclic Aromatic Hydrocarbons*, Elsevier, 1989, p. 317.
- [30] Renge, I., Wild, U. P., in Ariese, F., Gooijer, C., Hofstraat, J. W. (Eds.), *Shpol'skii Spectroscopy and Other Site Selection Methods*, Vol. 156, John Wiley, New York, 2000, pp. 19-71.
- [31] Dong, D. C., Winnik, M. A., *Can. J. Chem.* 1984, *62*, 2560-2565.
- [32] Fearey, B. L., Stout, R. P., Hayes, J. M., Small, G. J., *J. Chem. Phys.* 1983, *78*, 7013-7015.
- [33] Pedley, J. B., Naylor, R. D., Kirby, S. P., *Thermochemical Data of Organic Compounds*, Chapman and Hall, New York, 1986.
- [34] Bartke, J., Hentschke, R., *Phys. Rev. E* 2007, *75*, 061503-1-11.
- [35] Stenhammar, J., Linse, P., Karlström, G., *J. Chem. Phys.* 2010, *132*, 104507-1-10.
- [36] Renge, I., Mauring, K., *Spectrochim. Acta A* 2013, *102*, 301-313.

Chapter 5

Modeling of Fluorescence Line-Narrowed Spectra in Weakly Coupled Dimers

Chen Lin¹, Mike Reppert³, Ximao Feng¹, and Ryszard Jankowiak^{1,2,*}

¹Department of Chemistry and ²Department of Physics, Kansas State University, Manhattan, KS 66506;

³Department of Chemistry, MIT, Cambridge, MA 02139 (to be submitted)

*On a sabbatical leave from K-State, Manhattan, KS 66506 (present address: Faculty of Applied
Physics and Mathematics, Gdańsk University of Technology, Gdańsk, POLAND)
(to be submitted)

Abstract

This work describes simple analytical formulas to describe the fluorescence line-narrowed (FLN) spectra of weakly coupled dimers in the presence of excitation energy transfer (EET). This model can be extended to multiple chromophores. Modeling studies (assuming low fluence and weak coupling) show that the FLN spectra (including absorption and emission spectra) calculated for various dimers using our model are in good agreement with spectra calculated by: *i*) the simple convolution method (SCM) and *ii*) the more rigorous treatment using the Redfield approach (RA) (Renger, *et al.*, *J. Chem. Phys.* 2002, *116*, 9997). The calculated FLN spectra in the presence of EET of all three approaches are very similar. We argue that our approach provides a computationally efficient description of FLN spectra in the presence of EET. This method also has been applied to FLN spectra obtained for the CP47 antenna complex of Photosystem II reported in ref. (Neupane, *et al.* *JACS* 2010, *132*, 4214), which indicated the presence of uncorrelated EET between pigments contributing to the two lowest energy (overlapping) exciton states, each mostly localized on a single chromophore. Calculated and experimental and FLN spectra for CP47 complex show very good qualitative agreement.

List of Abbreviations

Δ FLN, delta fluorescence line-narrowed; Chl, chlorophyll; E_{λ} , reorganization energy; EET, excitation energy transfer; el-ph, electron-phonon; FLNS, fluorescence line-narrowing spectroscopy; HB, hole-burning; HG-HL, half-Gaussian half-Lorentzian; NPHB, nonphotochemical hole-burning; RA, Redfield approach; S , Huang- Rhys factor; SCM, simple convolution method; SDF, site-distribution function; V_{nm} , coupling matrix element; Γ_{inh} , width of inhomogeneous broadening.

5.1 Introduction

Fluorescence line-narrowing spectroscopy (FLNS) is a low-temperature spectroscopic technique which has been successfully employed over the years in detection/characterization of a wide variety of systems, e.g. organic molecules [1-3], inorganic systems [4], DNA and protein adducts ([5] and references therein). This technique also provides considerable insight into the electronic structure and excitation energy-transfer (EET) dynamics of excitonically coupled systems such as photosynthetic complexes [6]. One characteristic of photosynthetic systems is fast EET, thus FLN spectroscopic technique can provide information about the nature of low-energy states, excitonic interactions between coupled high- and low-energy pigments, and basic physical parameters of the system, such as spectral density and electron-phonon (el-ph) coupling strength. However, many modeling studies of FLN spectra followed a traditional approach to treat systems as dilute glasses [7-10], i.e., completely neglecting the effects of energy transfer and excitonic delocalization, which are present in complex biological systems (e.g. in various photosynthetic antenna pigment complexes). Only in computational studies based on experimental data in Jankowiak's group [11] and theoretical modeling by Renger *et al.* using the Redfield theory [12], these two effects have been taken into account.

In our recent modeling studies [11], Monte Carlo simulation was used to take care of random disorder of pigments site energies, and each set of site-energies was treated by a Hamiltonian with coupling strength between pigments reflected by the non-diagonal elements. A pure electronic spectrum is an average over disorder in site energies, and transition lineshapes are

obtained by simply convoluting pure electronic spectra with single site lineshape function [11]. In Renger and Marcus approach [12] using the Redfield theory [13-15], a density matrix description of transition lineshapes replaces the simple convolution method (SCM) in order to more accurately reflect the effects of electron-phonon coupling and energy-transfer lifetime broadening on the calculated optical spectra. The importance of lifetime broadening was also illustrated by modeling of resonant hole-burned (HB) spectra for various model dimers [16]. Though for stronger el-ph coupling strength ($S > 1$), different lineshape theories must be employed, as suggested in refs [17-19], the Redfield approach (RA) is an appropriate approximation for systems with low el-ph coupling strength.

However, in order to achieve reasonable signal-to-noise ratio in calculated FLN spectra using the RA, calculations are time-consuming and require the use of supercomputers. One possible way to ease the calculation processes of FLN spectra (in the presence of EET) is to develop analytical formulas to express lineshape functions and contributions from different exciton states (or pigments) instead of considering all possible site-energy combinations of chromophores, as used in Monte Carlo simulation and the Redfield approach. Under weak inter-pigment coupling and weak el-ph coupling conditions, where uncorrelated EET and efficient Förster energy transfer between pigments can take place, Reppert *et al.* [20] developed analytical formulas to describe the process of uncorrelated EET and to model nonphotochemical hole-burned (NPHB) spectra. In this work, the latter model [20] is extended to simulate resonant FLN spectra in the presence of EET. We show below that the analytical formulas developed to describe FLN spectra provide a very good approximation of both SCM and RA type calculations,

assuming that both excitonic and el-ph couplings are weak. That is, the coupling matrix element (V_{nm}) must be smaller than the reorganization energy (E_λ) and $S \leq 1$. We show below that our method provides very smooth spectra with a very short computation time (a few seconds) for a single FLN spectrum. That is, the computing time using our analytical formulas has been decreased by many orders of magnitude in comparison with the RA simulations. This work will also show that our model is applicable to describe the main features of the experimental FLN spectra obtained for the CP47 antenna of Photosystem II (PSII) [11] in which the lowest-energy Q_y-bands were mostly contributed to by two weakly coupled Chls [11]. The shapes of FLN spectra clearly suggested the presence of EET within the two low-energy absorption bands.

5.2 Derivation of Analytical Formulas to Calculate FLN Spectra in the presence of EET

A multi-chromophore system, which consists of N pigments, pigment i ($1 \leq i \leq N$) has SDF $f(\omega)$ with a Gaussian line shape centered at ϵ_i [20]. There are two components for pigment i . One component is a trap state $L_i(\omega)$, which is already at the lowest energy and is not capable to transfer energy; the other component allows EET to other pigments, and is labeled with $U_i(\omega)$.

$L_i(\omega)$ and $U_i(\omega)$ can be expressed as:

$$L_i(\omega) = P(\omega_i \approx \omega) \cdot \prod_{\substack{j=1 \\ j \neq i}}^N P(\omega_j > \omega) = f_i(\omega) \cdot \prod_{\substack{j=1 \\ j \neq i}}^N \left(1 - \int_{-\infty}^{\omega} f_j(t) dt \right), \quad (5-1)$$

and

$$U_i(\omega) = f_i(\omega) - U_i(\omega) = f_i(\omega) \cdot \left(1 - \prod_{\substack{j=1 \\ j \neq i}}^N \left(1 - \int_{-\infty}^{\omega} f_j(t) dt \right) \right), \quad (5-2)$$

where $P(\omega_i \approx \omega) \cdot \prod_{\substack{j=1 \\ j \neq i}}^N P(\omega_j > \omega)$ stands for the joint probability for $\omega_i \approx \omega$ in pigment i and $\omega_j > \omega$ in all other pigments.

Single-site spectra for all pigments are $\sigma(\omega - \omega_{ZPL})$ in absorption and $\sigma(\omega_{ZPL} - \omega)$ in fluorescence. The probability that a *trap-state* molecule of type i having ZPL frequency ω will be excited resonantly by the laser is given by

$$F_{R,i}(\omega) = L_i(\omega) \cdot \sigma(\omega_{exc} - \omega), \quad (5-3)$$

where ω_{exc} stands for the excitation frequency. Similarly, the probability that a non-trap state molecule of type i will be excited is given by $U_i(\omega) \cdot \sigma(\omega_{exc} - \omega)$. The fluorescence signal originating from resonant excitation of trap-state pigments is given (as in the absence of energy transfer) as the convolution of the $F_R(\omega)$ expression with the single-site fluorescence spectrum.

In the case of the emission spectrum originating from excitation of a non-trap state pigment of type i , after such an excitation has occurred, emission will occur not from pigment i but from the lowest energy trap in the complex. The probability density function for trap state pigments of types *other* than i is given by

$$\sum_{\substack{j=1 \\ j \neq i}}^N L_j(\omega). \quad (5-4)$$

However, if excitation occurs at some frequency ω_0 , it is clear that the lowest-energy trap state must have ZPL frequency lower than ω_0 ; so the distribution function for potential emitting states

becomes

$$\chi_{(-\infty, \omega_o)}(\omega) \cdot \sum_{\substack{j=1 \\ j \neq i}}^N L_j(\omega). \quad (5-5)$$

The probability of such an excitation occurring is given by $U_i(\omega_o) \cdot \sigma(\omega_{exc} - \omega_o)$, so that the probability density function for molecules emitting at frequency ω after absorption by a higher-energy pigment i at frequency ω_o becomes

$$U_i(\omega_o) \cdot \sigma(\omega_{exc} - \omega_o) \cdot \chi_{(-\infty, \omega_o)}(\omega) \cdot \sum_{\substack{j=1 \\ j \neq i}}^N L_j(\omega). \quad (5-6)$$

Integral over all possible values removes the dependence on ω_o :

$$\begin{aligned} & \int_{-\infty}^{\infty} U_i(\omega_o) \cdot \sigma(\omega_{exc} - \omega_o) \cdot \chi_{(-\infty, \omega_o)}(\omega) \cdot \sum_{\substack{j=1 \\ j \neq i}}^N L_j(\omega) d\omega_o \\ &= \left[\int_{-\infty}^{\infty} U_i(\omega_o) \cdot \sigma(\omega_{exc} - \omega_o) \cdot \chi_{(-\infty, \omega_o)}(\omega) d\omega_o \right] \cdot \sum_{\substack{j=1 \\ j \neq i}}^N L_j(\omega). \end{aligned} \quad (5-7)$$

Assuming for a moment ω as a fixed value, the function $\chi_{(-\infty, \omega_o)}(\omega)$ is zero when $\omega > \omega_o$ and is equal to one when $\omega \leq \omega_o$. The integrand $U_i(\omega_o) \cdot \sigma(\omega_{exc} - \omega_o) \cdot \chi_{(-\infty, \omega_o)}(\omega)$ is thus also zero when $\omega > \omega_o$ and is equal to $U_i(\omega_o) \cdot \sigma(\omega_{exc} - \omega_o)$ when $\omega \leq \omega_o$. The integral can thus also be expressed as

$$\left[\int_{\omega}^{\infty} U_i(\omega_o) \cdot \sigma(\omega_{exc} - \omega_o) d\omega_o \right] \cdot \sum_{\substack{j=1 \\ j \neq i}}^N L_j(\omega). \quad (5-8)$$

There will be N such probability density functions, reflecting excitation of the non-trap distributions of each of the N pigments in the complex. The total non-resonant emission spectrum is given by

$$\begin{aligned}
F_{NR}(\omega) &= \sum_{i=1}^N \left[\left(\int_{\omega}^{\infty} U_i(\omega_o) \cdot \sigma(\omega_{exc} - \omega_o) d\omega_o \right) \cdot \sum_{\substack{j=1 \\ j \neq i}}^N L_j(\omega) \right] \\
&= \sum_{i=1}^N \sum_{\substack{j=1 \\ j \neq i}}^N \left[L_j(\omega) \cdot \int_{\omega}^{\infty} U_i(\omega_o) \cdot \sigma(\omega_{exc} - \omega_o) d\omega_o \right] \quad . \quad (5-9) \\
&= \sum_{\substack{i,j=1 \\ i \neq j}}^N L_j(\omega) \cdot \int_{\omega}^{\infty} U_i(\omega_o) \cdot \sigma(\omega_{exc} - \omega_o) d\omega_o
\end{aligned}$$

The total fluorescence distribution function is

$$F(\omega) = F_{NR}(\omega) + F_R(\omega). \quad (5-10)$$

The actual fluorescence spectrum can be calculated as the convolution of this function with the single-site fluorescence spectrum F_{Flu} :

$$\begin{aligned}
FLNS(\omega) &= \left[\sum_{i=1}^N L_i(\omega) \cdot F_{Abs,i}(\omega_{exc} - \omega) \right. \\
&\quad \left. + \sum_{\substack{i,j=1 \\ i \neq j}}^N L_j(\omega) \cdot \int_{\omega}^{\infty} U_i(\omega_o) \cdot F_{Abs,i}(\omega_{exc} - \omega_o) d\omega_o \right] * F_{Flu} \quad . \quad (5-11)
\end{aligned}$$

In this equation, $F_{abs,i}(\omega_{exc} - \omega)$ is the reflection of single-site absorption spectrum with respect to excitation frequency for pigment i . In this method, assuming all pigments have the same transition dipole moment, bulk absorption spectrum is obtained by convoluting the sum of SDFs for all pigments with single-site absorption, while bulk emission is calculated by convoluting the sum of trap state from all pigments $\sum_{i=1}^N L_i(\omega)$ with single-site fluorescence.

Though the method developed in this work does not include pigments' coupling constant under the assumption of weak coupling, this parameter is involved in the calculation of Monte Carlo simulation and the Redfield approach. Thus, in the model calculations for a weakly

coupled dimer, using our analytical formulas, we consider effects of three parameters: i) site energy differences, ii) the strength of the el-ph coupling (Huang-Rhys factor S), and iii) inter-pigment coupling constant.

5.3 Results and Discussion

5.3.1 Spectral Density

Spectral density $J(\omega)$ provides information about the reservoir and its interaction with the relevant system; it is important to describe bath relaxation dynamics associated with the exciton transfer process [12]. Coupling to the bath reveals which frequencies are available in the bath to relax. At $T = 0$ K, the Huang-Rhys factor (S) is given by [21]

$$S = \int_0^{\infty} d\omega J(\omega). \quad (5-12)$$

At the same time, reorganization energy (E_λ) is defined as

$$E_\lambda = \hbar \int_0^{\infty} \omega J(\omega) d\omega . \quad (5-13)$$

This parameter is the energy cost due to geometry modifications [12]. The profile of spectral density can be obtained by fitting the experimental shape of the phonon sideband in the (delta) fluorescence line-narrowed (Δ FLN) spectrum excited in the low-energy wing of the SDF. (We emphasize that the proper shape of $J(\omega)$ cannot be obtained from simple FLN spectra, as often reported in the literature [12, 22, 23].)

Various empirical functional forms for $J(\omega)$ are used in simulations, and one frequently used function for spectral density in the HB community is half-Gaussian half-Lorentzian

(HG-HL) shape ([6, 24] and references therein), as its shape is similar to the experimental one-phonon profile. This form, however, cannot be used in Redfield calculation as it leads to infinitely large E_λ and cannot be used in energy transfer expressions; therefore, a lognormal distribution function is used in this work to describe the shape of spectral density [20], i.e.,

$$J(\omega) = \frac{S}{\omega\sigma\sqrt{2\pi}} e^{-\frac{[\ln(\omega/\omega_c)]^2}{2\sigma^2}}. \quad (5-14)$$

which also provided excellent fits of experimental spectra densities [20]. In Eq. (5-14), S is the integrated area of spectral density, and equals the value of Huang-Rhys factor. Parameters σ and ω_c are standard deviation and mean of the lognormal distribution. Substituting Eq. (5-14) into the integral in Eq. (5-13) yields a well-defined E_λ .

To calculate $J(\omega)$ we use $\sigma = 0.764$ and $\omega_c = 52.0 \text{ cm}^{-1}$. This spectral density resembles HG-HL shape of the one-phonon profile with the mean phonon frequency ω_m of 26 cm^{-1} and the FWHM = 26 cm^{-1} (for Gaussian part) and 85 cm^{-1} (for Lorentzian part) of $J(\omega)$. The parameters used in our modeling studies are reasonable, as similar parameters were observed in many photosynthetic antenna pigment complexes [25-28].

5.3.2 Building Single-Site Spectrum for the Analytical Formula Method

According to [6], within the Franck-Condon approximation and low-temperature limit ($T \rightarrow 0 \text{ K}$), single-site absorption (SSA) and single-site emission (SSE) spectra can be expressed as

$$L_{A/F}(\omega) = e^{-S} l_0(\omega - \Omega_0) + \sum_{R=1}^{\infty} S^R \frac{e^{-S}}{R!} l_R(\omega - \Omega_0 \mp R\omega_m). \quad (5-15)$$

In this equation, $L_{A/F}(\omega)$ is single-site spectrum for absorption/emission; $l_0(\omega - \Omega_0)$ is the

Lorentzian line shape of the ZPL peaking at Ω_0 ; $l_R(\omega - \Omega_0 \pm R\omega_m)$ stands for the normalized line-shape function of the R -phonon transition ($R = 1, 2, \dots$) with peak position at $\Omega_0 \pm R\omega_m$ (+ for emission and – for absorption). A Poisson weighting factor for every R determines the intensity distribution of the PSB. The profile l_R is obtained by folding with itself for R times. l_1 is one-phonon profile and equals the normalized spectral density. Thus, in this work, for absorption, $l_1(\omega - \Omega_0 - R\omega_m)$ can be described by equation (5-14).

5.3.3 Comparison of Three Calculation Methods to Obtain FLN Spectra

As an instructive example, we consider a weakly coupled dimer composed of A- and B-pigments. Thus, equation (5-11) can be rewritten as:

$$\begin{aligned}
 FLNS(\omega) = & \left[L_A(\omega) \cdot F_{Abs,A}(\omega_{exc} - \omega) + L_B(\omega) \cdot F_{Abs,B}(\omega_{exc} - \omega) \right. \\
 & + L_A(\omega) \cdot \int_{\omega}^{\infty} U_B(\omega_o) \cdot F_{Abs,B}(\omega_{exc} - \omega_o) d\omega_o \\
 & \left. + L_B(\omega) \cdot \int_{\omega}^{\infty} U_A(\omega_o) \cdot F_{Abs,A}(\omega_{exc} - \omega_o) d\omega_o \right] * F_{Flu}
 \end{aligned} \quad (5-16)$$

We assume that both pigments have Gaussian shape of the SDF with a FWHM of 200 cm^{-1} . Two categories of pigment interaction are considered in our calculations: extremely weak coupling (coupling constant V_{AB} is set to 0.1 cm^{-1}), and moderately weak coupling (with $V_{AB} = 25 \text{ cm}^{-1}$). Very small coupling matrix elements (i.e. $V_{AB} \sim 0-2 \text{ cm}^{-1}$) are observed between very weakly interacting pigments in various antenna pigment complexes. For example, the coupling constant between chlorophyll 514 and chlorophyll 526 in CP47 antenna system [11] is close to zero, while the coupling constant between Chl523 and Chl 526 is 2 cm^{-1} . However, this is not a general case

for weakly coupled dimers. Thus, in the calculation, we also investigate situations when systems have moderately weak coupling constant ($V_{AB} = 25 \text{ cm}^{-1}$).

Extremely Weak Coupling ($V_{AB} = 0.1 \text{ cm}^{-1}$)

Figure 5-1 shows a degenerate case where the site energies of both pigments (A and B) are set at 15000 cm^{-1} , with the Huang-Rhys factor of 0.2 and coupling constant $V_{AB} = 0.1 \text{ cm}^{-1}$. For simplicity, we refer to the calculation method developed in this work as the analytical expression method. Calculated spectra shown in Figure 5-2 and 5-3 follow the same format as that in Figure 5-1, unless otherwise stated.

It is clear that under this parameter set, all three calculation methods show almost identical spectra obtained for the bulk absorption and emission spectra. The only difference is that the peak positions of the absorption and emission spectra calculated by the RA must be corrected (i.e., red-shifted) by the value of reorganization energy, i.e. in this case by about 14 cm^{-1} when $S = 0.2$. Column 3 shows the calculated FLN spectra at various excitation frequencies with three different methods (see figure caption for details). Note that in order to match the relative position of the excitation on the bulk absorption spectrum, the excitation frequencies chosen for FLN calculation in the RA methodology are 14 cm^{-1} lower in energy. When the excitation frequency is at the low-energy side of the SDF (and $S < 1$), FLN signal has significantly larger contribution from resonant emission than non-resonant emission, resulting in FLN spectra with very intense zero-phonon lines (ZPLs) and weak phonon side-bands (PSBs); see black curves in column 3 ($\omega_{\text{exc}} = 14800 \text{ cm}^{-1}$) of Figure 5-1. In order to better resolve the shape of PSBs, black spectra are zoomed by the factor showed in each corresponding frame.

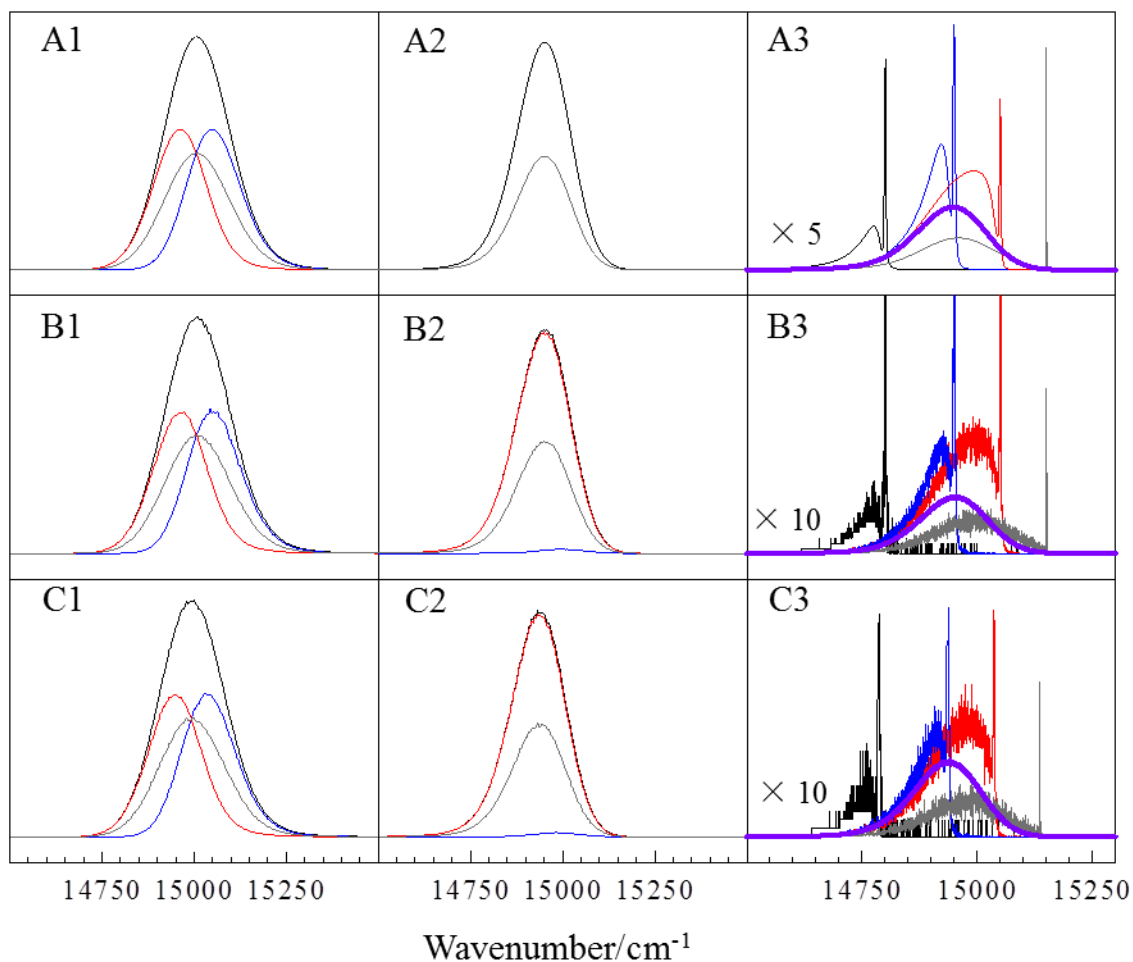


Figure 5-1. Calculated spectra of weakly coupled dimer with degenerate site energies at 15000 cm^{-1} ($V_{AB} = 0.1 \text{ cm}^{-1}$); inhomogeneous broadening ($\Gamma_{\text{inh}} = 200 \text{ cm}^{-1}$; Huang-Rhys factor $S = 0.2$; and mean phonon frequency $\omega_m = 26 \text{ cm}^{-1}$). Rows A1-3, B1-3, and C1-3 are calculation results using our analytical expressions, SCM, and the RA, respectively. Columns 1, 2, and 3 correspond to calculated absorption, emission, and FLN spectra. In the first two columns, black lines are calculated bulk spectra; red and blue curves stand for contributions from the pigments from trap-state and EET component, respectively; gray lines are contributions from each pigment. In the third column, black, blue, red, and gray spectra are collected with excitation wavenumber at 14800 cm^{-1} , 14950 cm^{-1} , 15050 cm^{-1} , and 15150 cm^{-1} , respectively (excitation frequencies are red-shifted by 14 cm^{-1} in RA methodology to correct the shift due to reorganization energy); thick purple lines are calculated emission spectra (same as black curves in column 2 in each corresponding row).

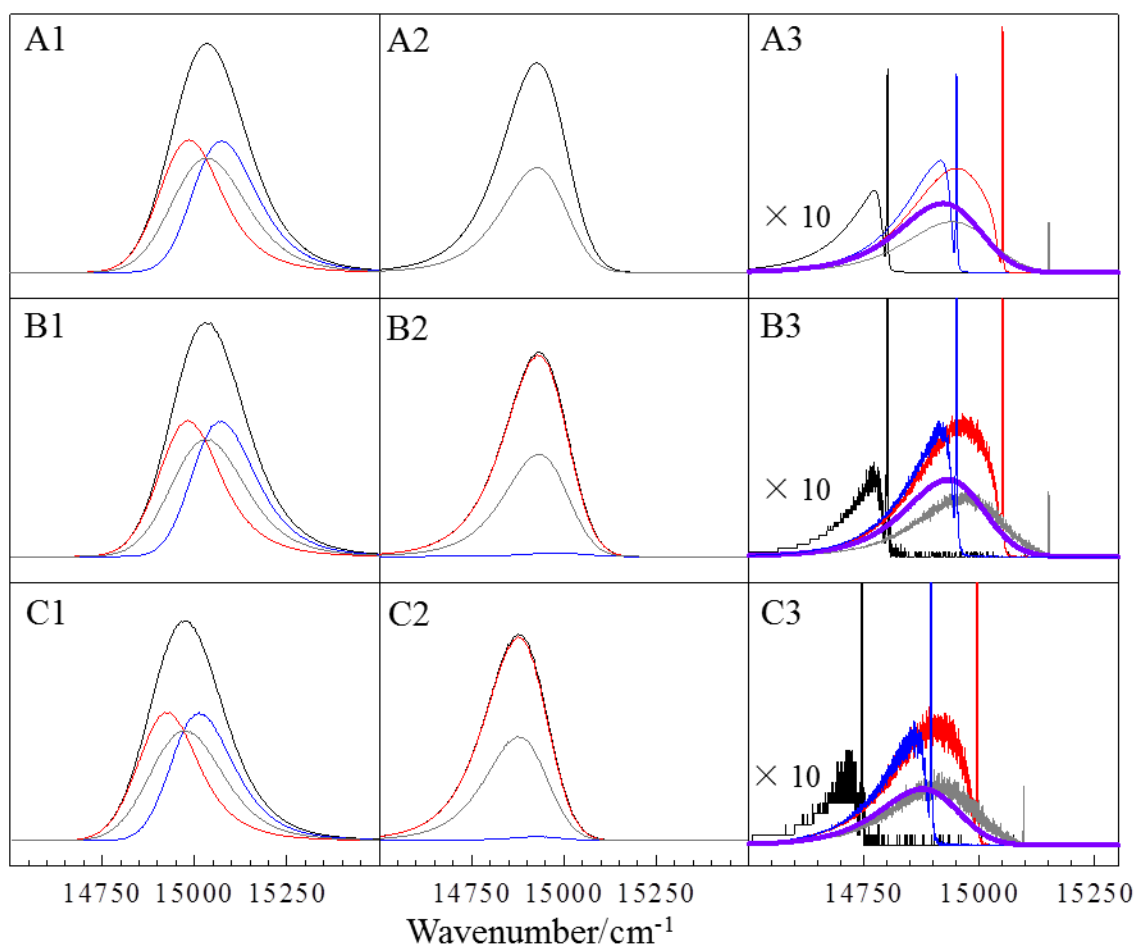


Figure 5-2. Calculated spectra of weakly coupled dimer with degenerate site energies at 15000 cm^{-1} . Coupling constant is $V_{AB} = 0.1 \text{ cm}^{-1}$; inhomogeneous broadening is $\Gamma_{\text{inh}} = 200 \text{ cm}^{-1}$; Huang-Rhys factor $S = 0.8$. In the third column, black, blue, red, and gray spectra are collected with excitation wavenumber at 14800 cm^{-1} , 14950 cm^{-1} , 15050 cm^{-1} , and 15150 cm^{-1} , respectively. Note, excitation frequencies to generate data shown in frame C3 (RA methodology) are red-shifted by 55 cm^{-1} to correct for the shift due to reorganization energy.

All three methods (i.e., analytical formulas, SCM, and RA) show the same trend of the change of FLN spectra with different excitation frequencies; that is, the larger the excitation energy, the more contribution from non-resonant emission (due to a fast EET process from higher energy pigment to the low energy pigment) is observed, and FLN spectra resemble the bulk emission spectra (compare the purple curves in frames A3, B3 and C3).

Figure 5-2 shows calculated spectra for larger S value ($S = 0.8$). Note that for $V_{AB} = 0.1 \text{ cm}^{-1}$ and $\Gamma_{inh} = 200 \text{ cm}^{-1}$ the absorption and emission maxima, calculated by the R-approach are (as expected) red-shifted by $\sim 55 \text{ cm}^{-1}$ in comparison with spectra obtained via our analytical expressions and SCM. Therefore, as the same in Figure 5-1, the excitation frequencies chosen for FLN calculation in the RA methodology are 55 cm^{-1} lower in energy. Recall that a direct comparison of FLN spectra using the three methods described above can be only made as long as the bulk absorption spectra match. Note that the FLN spectra calculated with all three methodologies for larger S -value ($S = 0.8$) are also very similar.

The same methodologies discussed above, were also used to perform calculation for the *non-degenerated* dimers with site energies at 14950 cm^{-1} and 15050 cm^{-1} and the coupling constant $V_{AB} = 0.1 \text{ cm}^{-1}$ as shown in figures A-1 and A-2 in the Supporting Information (SI) in Appendix A of the thesis. Unlike in the case of degenerated dimers, where both type of pigments contribute equally to trap- and/or energy transfer state, in the case of *non-degenerated* dimer the trap state is mainly localized on pigments with lower site-energy, while the state which allows EET is mostly localized on pigments with higher site-energy. Therefore, the two pigments have different contribution to the bulk emission spectra. Except for this difference, same conclusions,

as those obtained based on data presented in Figures 5-1 and 5-2, can be drawn. Thus, we conclude that in the presence of EET, when pigments have extremely weak intermolecular coupling constants, our analytical formula provides a perfect approximation for SCM and the RA calculations. Regarding calculation time, our new and simple method only takes several seconds to calculate FLN spectra; while to obtain calculated FLN spectra with similar quality, both SCM and RA simulations require the calculation program to be run on super computers for at least a couple of hours. Therefore, the calculating method with analytical expression is preferred in simulating spectra for systems with extremely weak coupling constants in the presence of EET.

Moderately Weak Coupling ($V_{AB} = 25 \text{ cm}^{-1}$)

Figure 5-3 shows calculated optical spectra for $V = 25 \text{ cm}^{-1}$ and $S = 0.8$. Note that under this condition, V_{AB} is smaller than reorganization energy (55 cm^{-1}), and this also falls into the regime of weak coupling. Unlike in frame A1 of Figure 5-3, where upper and lower excitonic states contribute equivalently to the total absorption spectrum (due to the fact that coupling constant is not involved in the calculation by analytical expression method), both SCM and RA-type simulations show larger contribution from lower excitonic state (trap state), resulting in narrower bandwidths of absorption spectra shown in frames B1 and C1. This is due to the fact that excitonic delocalization is taken into account in Redfield calculation, and the width of the distribution of excitonic energies experiences a narrowing that scales with the square root of the delocalization number [29, 30]. Recall that the Redfield theory takes energy-transfer lifetime into account, thus the higher excitonic state (blue line in Figure 5-3 C1) is slightly broader and less intense than that calculated by SCM (blue line in frame B1 of Figure 5-3).

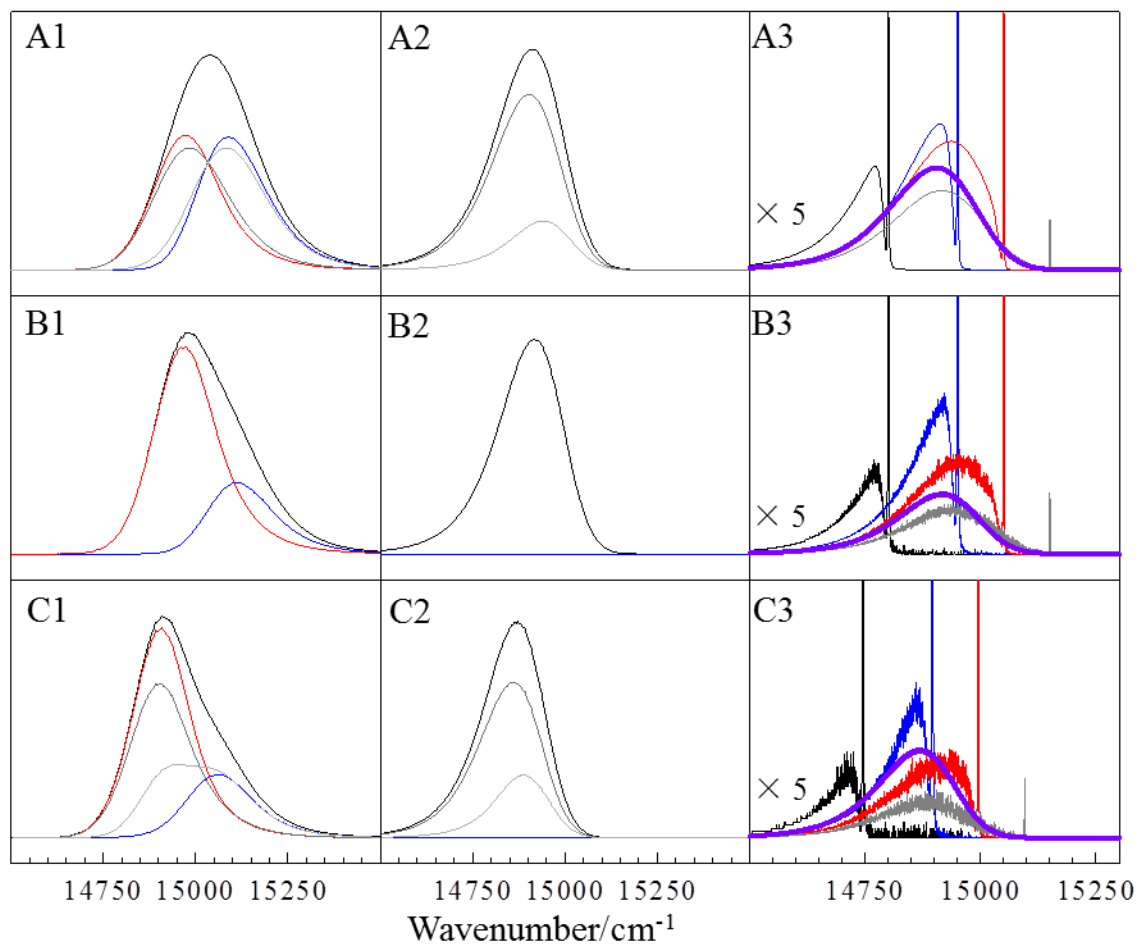


Figure 5-3. Calculated spectra of a weakly coupled dimer with degenerate site energies of 15000 cm^{-1} . Coupling constant is 25 cm^{-1} ; $\Gamma_{\text{inh}} = 200 \text{ cm}^{-1}$; $S = 0.8$. In the third column, black, blue, red, and gray spectra are collected with excitation wavenumber at 14800 , 14950 , 15050 , and 15150 cm^{-1} , respectively (excitation frequencies are red-shifted by 55 cm^{-1} in RA calculations to correct for the shift due to E_{λ}).

On the contrary, emission spectra calculated by three methods (black curves in column 2 of Figure 5-3) do not reveal large changes. Emission spectra in frame A2 and B2 are similar, suggesting that under the calculation condition ($V_{AB} = 25 \text{ cm}^{-1}$), our derived formulas are still a good approximation for SCM in calculating emission spectra. Hence, a negligible difference should be observed in the FLN spectra calculated by our derived analytical formulas and SCM simulation, in agreement with our modeling results shown in Figure 5-3.

In the Redfield calculations (RA; row 3 of Figure 5-3), emission spectrum is narrowed by $\sim 5\%$ comparing to black curves in frames A2 and B2. This is because the effective S factor involved in RA for a spectral profile is smaller than the input Huang-Rhys factor (apparent S factor). When a smaller apparent S factor is chosen, this narrowing effect becomes negligible. For example, Figure A-3 in SI (Appendix A of the thesis) shows calculated spectra for $S = 0.2$ and $V_{AB} = 25 \text{ cm}^{-1}$. Though in Figure A-3, conditions for calculations no longer meet the criteria for a weak coupling limit, which requires coupling constant smaller than E_λ (E_λ is $\sim 14 \text{ cm}^{-1}$ when $S = 0.2$), the expected narrowing of the emission spectrum becomes negligibly small. The small amount of narrowing in emission spectra calculated by Redfield theory is also observed in the case of a non-degenerated dimer (when $V_{AB} = 25 \text{ cm}^{-1}$); see Figures A-4 and A-5 in the SI. Therefore, our derived formulas are not applicable for absorption spectra when pigments of the system have moderately weak coupling constants ($10 \text{ cm}^{-1} \leq V_{AB} \leq E_\lambda$). Nevertheless, our model is still a good approximation for SCM and RA in calculating emission and FLN spectra when required percentage error is no larger than 5%.

5.3.4 Fluorescence Line-Narrowing Spectra of CP47 Antenna Complex

CP47 is one of the core antenna protein complexes of PSII, which binds 16 Chls [31, 32]. By simulating CP47 absorption, emission, and nonresonant HB spectra, Reppert *et al.* reported [11] that the two lowest energy Q_y -absorption bands (partly degenerate) are mostly localized on two weakly coupled pigments, i.e. pigment A = Chl 523 and pigment B = Chl 526, with the coupling constant V_{AB} of 2 cm^{-1} [11]. It was suggested the shape FLN spectra excited within the low energy Q_y -band were affected by an uncorrelated EET between pigments contributing to the two lowest-energy absorption bands. Below we use the analytical formulas (derived in this work for *weakly* coupled dimers), and apply them to describe the experimental FLN spectra reported in ref. [33], which are re-plotted in Figure 5-4B for comparison. The relative intensities of ZPLs for experimental data is not available, as the spectra were measured with continuous mode (CW) laser [33]. In our modeling studies of the CP47 FLN spectra, in contrast to the calculations discussed above, we use the parameters from ref. [11]. That is, we assume that the site energies for Chl 523 and Chl 526 are 14420 cm^{-1} and 14562 cm^{-1} , respectively. The FWHM of the corresponding Gaussian distributions are 150 and 190 cm^{-1} , with the integrated band areas of 0.44 and 1.0 , respectively. The inset in Figure 5-4A shows relative intensities of the calculated ZPLs that were cut off to more clearly reveal the shapes of PSBs in the main frame.

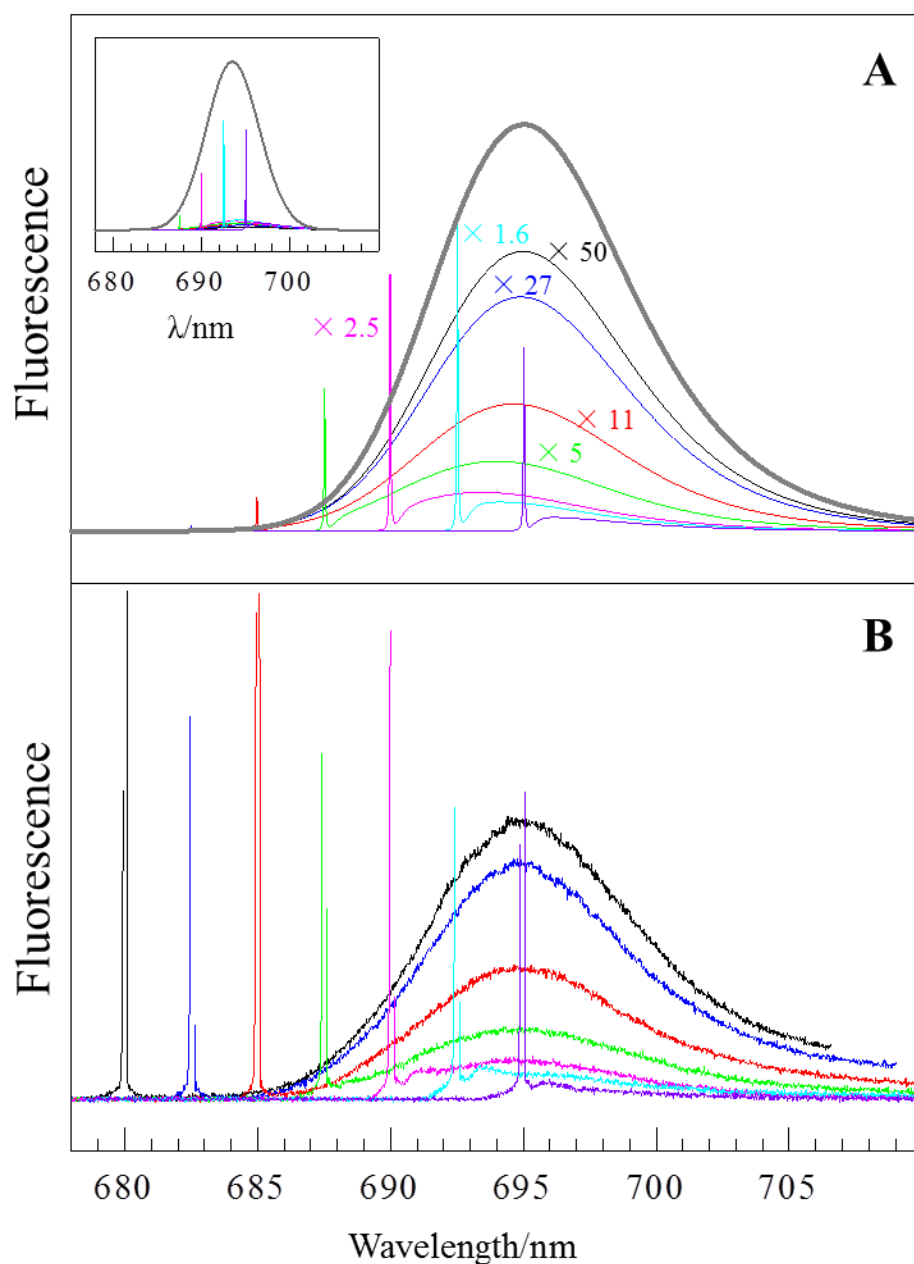


Figure 5-4. Calculated (frame A) and experimental (frame B) FLN spectra of CP47. Analytical expression method is used for calculation, and only the two pigments with lowest site-energies are considered in the model (Chl 523 with site energy at 14420 cm^{-1} and 150 cm^{-1} FWHM; Chl 526 with site energy at 14562 cm^{-1} and 190 cm^{-1} FWHM). Mean phonon frequency is 26 cm^{-1} . In each frame, black, blue, red, green, magenta, cyan and purple curves stand for excitation wavelengths at 680.0, 682.5, 685.0, 687.5, 690.0, 692.5, and 695.0 nm, respectively. Thick gray line in frame A is the calculated bulk emission. Inset in frame A shows the relative intensities of ZPLs for calculated FLN spectra with respect to SDF of the lowest energy state.

Both calculated and experimental FLN spectra are qualitatively similar, that is, decreasing excitation wavelength (i.e. increasing frequency/energy) makes the shape of FLN spectra very similar to the non-resonantly excited emission (see the gray thick and black curves in frames A and B, respectively). The latter is caused by the uncorrelated EET from the second (higher-energy band) to the lowest energy trap from which emission occurs. Note that calculated emission spectrum is somewhat narrower than the experimental one, as only the two lowest energy Chls were taken into account in our simulations. That is, contributions from other chlorophylls in CP47 weakly contributing to the two lowest excitonic energy bands, as well as vibration-phonon coupling, were neglected here for simplicity. Nevertheless, the calculated FLN spectra for the CP47 complex using our analytical expressions developed in this work provide a good fit to the experimental FLN spectra obtained for the CP47 antenna protein complex, and support our previous suggestion that some of the FLN spectra reported in Ref. [33] were affected by uncorrelated EET. This agreement further supports our earlier findings that Chl 526 does not contribute solely to the lowest energy state, since it is too weakly coupled to other pigments to produce either the low oscillator strength needed to fit the absorption and red-shifted emission spectra or the excitonic features of the persistent HB spectrum described in ref. [11].

5.4 Conclusions

This work describes simple analytical formulas for the absorption, emission, and fluorescence line-narrowed (FLN) spectra for *weakly* coupled dimers in the presence of uncorrelated EET between pigments contributing to the low energy absorption bands. This

approach can be extended to describe FLN spectra for systems with more than two pigments, for example, antenna pigment complexes with multiple chromophores. We showed that in the weak el-ph coupling limit the derived formulas provide a good approximation to computationally expensive SCM simulations and, in particular, to the Redfield-approach calculated FLN spectra. Importantly, the analytical expressions provide significantly shorter computation time and smoother spectra than those obtained with the Redfield-type calculations. Application of the derived expressions to the FLN spectra obtained for the CP47 antenna protein complex [33] (assuming an uncorrelated EET between two pigments contributing to the two nearly degenerated low-energy absorption bands) also yielded good qualitative agreement. Calculated and experimental and FLN spectra for CP47 complex show very good qualitative agreement. Finally, our data do not support earlier Raszewski and Renger [22, 34] assignment that the red tail of the absorption spectrum of CP47 is localized on Chl 526 (or Chl 29 based on the numbering according to the nomenclature of Loll et al. [35]), which is responsible for the 695 nm emission [11]. In contrast, the shapes of the FLN spectra, which clearly indicate the presence of uncorrelated EET between pigments contributing to the two lowest-energy (overlapping) Q_y -absorption bands, are mostly contributed to by two Chls, i.e. Chl523 (lowest energy state) and Chl526 (second lowest-energy state).

Acknowledgments

This work was supported by the Chemical Sciences, Geosciences and Biosciences Division, Office of Basic Energy Sciences, Office of Science, U.S. Department of Energy (grant EC9987 to RJ).

Supporting Information Available

This material contains additional examples of modeled FLN spectra in weakly coupled dimers obtained for different sets of parameters and is in Appendix A of this thesis.

References

- [1] Personov, R. I., in: Agranovich, V. M., Hochstrasser, R. M. (Ed.), *Spectroscopy and Excitation Dynamic of Condensed Molecular Systems*, North-Holland, Amsterdam 1983, pp. 555-619.
- [2] Jankowiak, R., Small, G. J., *Chem. Res. Toxicol.* 1991, 4, 256-269.
- [3] Nakhimovski, L., Lamotte, M., Jousot-Dubien, J., *Handbook of Low Temperature Electronic Spectra of Polycyclic Aromatic Hydrocarbons*, Elsevier, Amsterdam—New York—Oxford—Tokyo 1989.
- [4] Riseberg, L. A., *Phys. Rev. A* 1973, 7, 671-678.
- [5] Ariese, F., Jankowiak, R., in: Gooijer, C., Ariese, F., Hofstraat, J. W. (Ed.), *Shpol'skii Spectroscopy and Other Site-Selection Methods*, John Wiley and Sons, Inc., New York 2000, pp. 333-362.
- [6] Jankowiak, R., Reppert, M., Zazubovich, V., Pieper, J., Reinot, T., *Chem. Rev.* 2011, 111,

4546-4598.

- [7] Kharlamov, B. M., Personov, R. I., Bykovska.La, *Opt. Commun.* 1974, *12*, 191-193.
- [8] Purchase, R., Volker, S., *Photosynth. Res.* 2009, *101*, 245-246.
- [9] Hayes, J. M., Gillie, J. K., Tang, D., Small, G. J., *Biochim.Biophys. Acta* 1988, *932*, 287-305.
- [10] Jankowiak, R., Hayes, J. M., Small, G. J., *Chem. Rev.* 1993, *93*, 1471-1502.
- [11] Reppert, M., Acharya, K., Neupane, B., Jankowiak, R., *J. Phys. Chem. B* 2010, *114*, 11884-11898.
- [12] Renger, T., Marcus, R. A., *J. Chem. Phys.* 2002, *116*, 9997-10019.
- [13] Blum, K., *Density Matrix Theory and Application*, Plenum, New York 1981, pp. 261-299.
- [14] May, V., Kühn, O., *Charge and Energy Transfer Dynamics in Molecular Systems: A Theoretical Introduction*, Wiley-VCH, Berlin 2000, pp. 103-113, 137, 203, 233.
- [15] Kühn, O., May, V., Schreiber, M., *J. Chem. Phys.* 1994, *101*, 10404-10415.
- [16] Reppert, M., *Phys. Chem. Lett.* 2011, *2*, 2716-2721.
- [17] Schroder, M., Kleinekathofer, U., Schreiber, M., *J. Chem. Phys.* 2006, *124*, 084903.
- [18] Ishizaki, A., Fleming, G. R., *J. Chem. Phys.* 2009, *130*, 234110.
- [19] Novoderezhkin, V. I., van Grondelle, R., *Phys. Chem. Chem. Phys.* 2010, *12*, 7352-7365.
- [20] Reppert, M., Naibo, V., Jankowiak, R., *Chem. Phys.* 2010, *367*, 27-35.
- [21] May, V., Kühn, O., *Charge and Energy Transfer Dynamics in Molecular Systems*, 2nd Ed. Wiley-VCH, Weinheim 2004.
- [22] Shibata, Y., Nishi, S., Kawakami, K., Shen, J.-R., Renger, T., *J. Am. Chem. Soc.* 2013, *manuscript accepted*, DOI: 10.1021/ja312586p.
- [23] Wendling, M., Pullerits, T., Przyjalowski, M. A., Vulto, S. I. E., Aartsma, T. J., van Grondelle, R., van Amerongen, H., *J. Phys. Chem. B* 2000, *104*, 5825-5831
- [24] Hayes, J. M., Lyle, P. A., Small, G. J., *J. Phys. Chem.* 1994, *98*, 7337-7341.
- [25] Pieper, J., Voigt, J., Renger, G., Small, G. J., *Chem. Phys. Lett.* 1999, *310*, 296-302.
- [26] R äsep, M., Pieper, J., Irrgang, K.-D., Freiberg, A., *J. Phys. Chem. B* 2008, *112*, 110-118.

- [27] Kell, A., Feng, X., Reppert, M., Jankowiak, R., *J. Phys. Chem. B* 2013, submitted.
- [28] R äsep, M., Freiberg, A., *J. Lum.* 2007, 127, 251-259.
- [29] Renger, T., May, V., *Phys. Rev. Lett.* 2000, 84, 5228-5231.
- [30] Knapp, E. W., *Chem. Phys.* 1984, 85, 73-82.
- [31] Guskov, A., Kern, J., Gabdulkhakov, A., Broser, M., Zouni, A., Saenger, W., *Nat. Struct. Mol. Biol.* 2009, 16, 334-342.
- [32] Loll, B., Kern, J., Saenger, W., Zouni, A., Biesiadka, J., *Nature* 2005, 438, 1040-1044.
- [33] Neupane, B., Dang, N. C., Acharya, K., Reppert, M., Zazubovich, V., Picorel, R., Seibert, M., Jankowiak, R., *J. Am. Chem. Soc.* 2010, 132, 4214-4229.
- [34] Raszewski, G., Renger, T., *J. Am. Chem. Soc.* 2008, 130, 4431-4446.
- [35] Loll, B., Kern, J., Zouni, A., Saenger, W., Biesiadka, J., Irrgang, K. D., *Photosynth. Res.* 2005, 86, 175-184.

Chapter 6

Concluding Remarks and Future Prospects

Chapters two and three discuss analytical applications of low-temperature laser-induced fluorescence spectroscopy using both non-resonant and resonant laser excitations. Both modes of excitation are helpful in determination of conformation of chromophores in biological matter (e.g. in mAb and DNA) and provide more insight on the nature of physical complexes formed. In chapter two, though non-line narrowed fluorescence spectroscopy at 77 K is sufficient to elucidate that the enhanced π - π interaction provided by methylated cytosine favors intercalated conformation of BPT:DNA physical complex, more detailed information of this conformation can be obtained through collecting FLN spectra. In chapter three, we argue that π -cation interaction leads to blue-shifted and narrower fluorescence origin band at 5 K, compared to spectral properties of π - π interaction. We anticipate that if 4D5 monoclonal antibody with arginine inside the binding pocket could be mutated to an aromatic side chain (e.g. Phenylalanine), ELISA and fluorescence studies on pyrene/4D5 mutant can provide more direct evidence of the spectral differences associated with π - π and π -cation interaction.

In chapter four, we obtained fluorescence line narrowing (Δ FLN) spectra with ground-state excitation of pyrene (Py) in ethanol (EtOH) glass using time-resolved method, which completely removes laser scattering light and helps to determine the Huang-Rhys factor in a more accurate way. Chapter 4 provides experimental evidence that Δ FLN spectra resemble single-site fluorescence [1]. Besides, we argued that the simple repulsive-dispersive potential

model proposed in ref. [2] is not sufficient to account for a complex “color effect”, and cannot explain the very complex frequency dependence of the el-ph coupling (i.e., the frequency dependence of the S -factor) obtained for Py in ethanol glass and chlorin-doped 1-propanol glass [3]. At the high frequency edge the electron-phonon coupling is strongly enhanced by electrostatic interactions, and this should be included in more advance models developed to account for the observed variations of the electron-phonon coupling strength.

Chapter five shows that the analytical expression (AE) method developed for FLN spectra at the presence of excitation energy transfer is a good approximation of simple convolution method and the Redfield approach for systems with weak pigment coupling constant (smaller than reorganization energy) and small Huang-Rhys factor ($S < 1$). Though only calculation obtained for various dimers were discussed in chapter five, AE method can be easily extended to multi-pigment systems, and can also be used to model resonant hole burning line shapes, i.e., the model could be adapted to model hole-burned spectra in the low-fluence limit.

References

- [1] Reppert, M., Naibo, V., Jankowiak, R., *J. Chem. Phys.* 2010, *133*, 014506.
- [2] Renge, I., R äsep, M., Freiberg, A., *J. Lum.* 2011, *131*, 262-265.
- [3] R äsep, M., Pajusalu, M., Freiberg, A., *Chem. Phys. Lett.* 2009, *479*, 140-143.

Appendix A

Supporting Information for Chapter 5

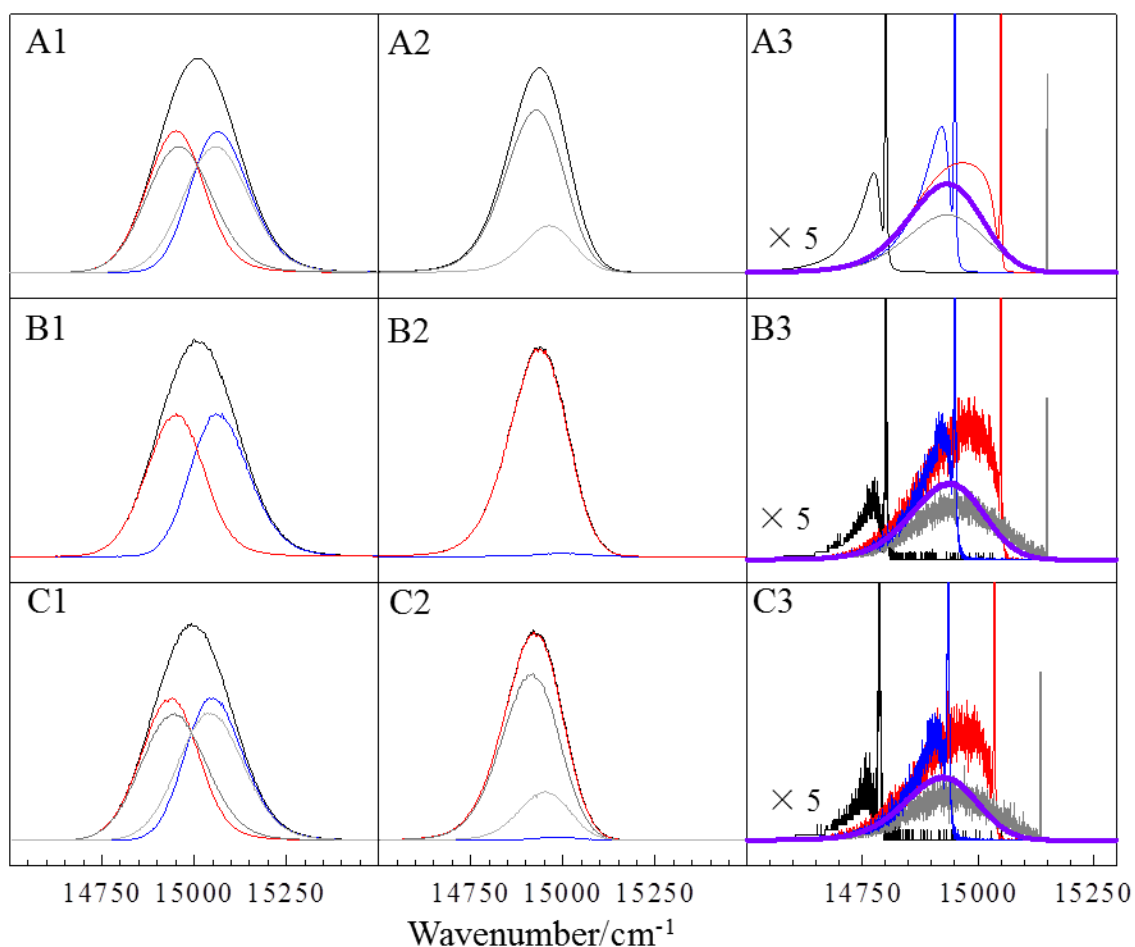


Figure A-1. Calculated spectra of weakly coupled dimer with site energies at 14950 cm^{-1} and 15050 cm^{-1} . Coupling constant is 0 cm^{-1} ; inhomogeneous broadening is 200 cm^{-1} ; S equals to 0.2 ; mean phonon frequency is 26 cm^{-1} . Rows A, B, and C are calculation results for analytical expression (AE), simple convolution (SC), and Redfield theory, respectively. Columns 1, 2, and 3 correspond to calculated absorption, emission, and FLN spectra, respectively. In the first two columns, black lines are calculated bulk spectra; red and blue curves are contributions from the pigments with lower and higher energy, respectively; dark and light gray lines are contribution from pigment with site energies at 14950 and 15050 cm^{-1} , respectively. In the third column, black, blue, red, and gray spectra are collected with excitation wavenumber at 14800 , 14950 , 15050 , and 15150 cm^{-1} , respectively (excitation frequencies are red-shifted by 14 cm^{-1} in R-approach to correct the shift due to reorganization energy); thick purple lines are calculated emission spectra (same as black curves in column 2 in each corresponding row). Other figures shown calculated spectra in this part follow the same figure legend unless otherwise stated.

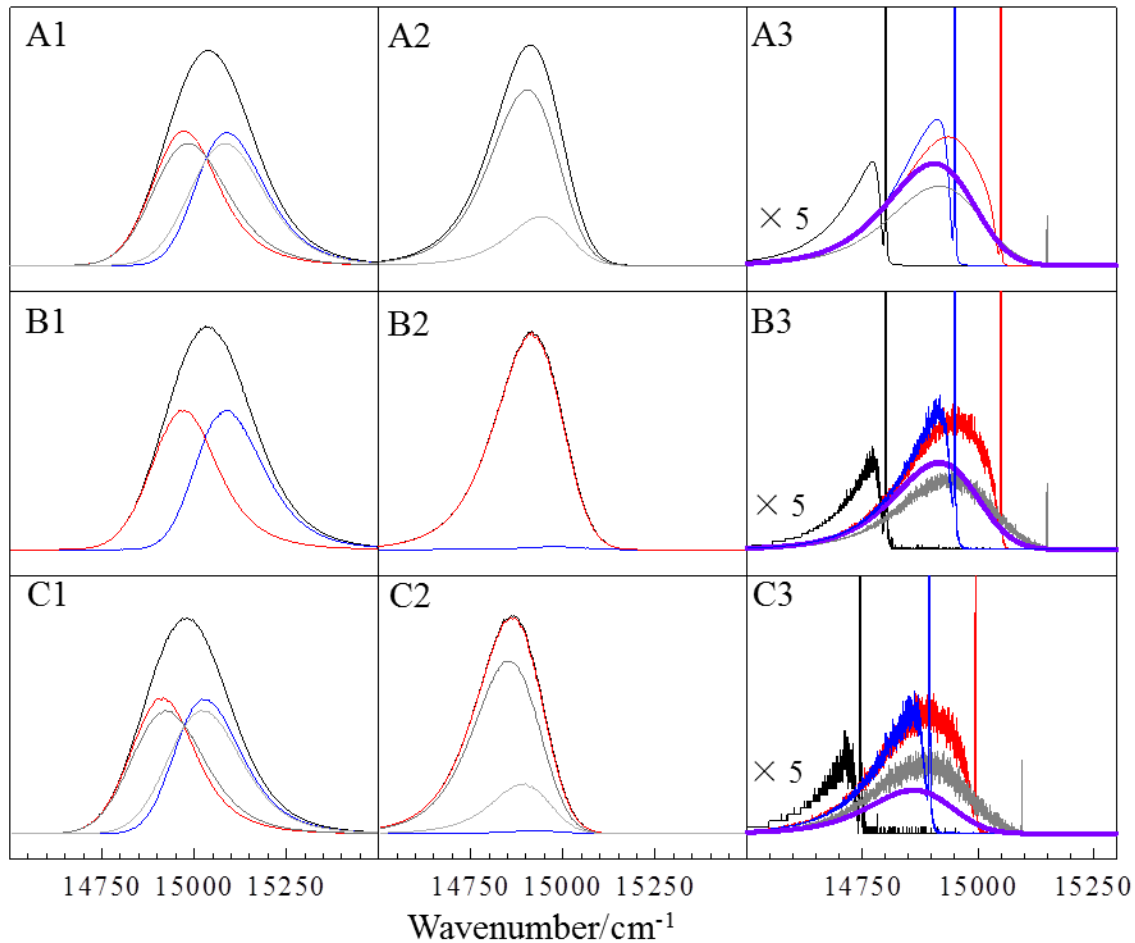


Figure A-2. Calculated spectra of weakly coupled dimer site energies at 14950 cm^{-1} and 15050 cm^{-1} . Coupling constant is 0 cm^{-1} ; inhomogeneous broadening is 200 cm^{-1} ; Huang-Rhys factor S equals to 0.8 ; mean phonon frequency is 26 cm^{-1} . In the third column, black, blue, red, and gray spectra are collected with excitation wavenumber at 14800 cm^{-1} , 15000 cm^{-1} , 15100 cm^{-1} , and 15200 cm^{-1} , respectively (excitation frequencies are red-shifted by 55 cm^{-1} in Redfield theory calculation to corrected the shift due to reorganization energy).

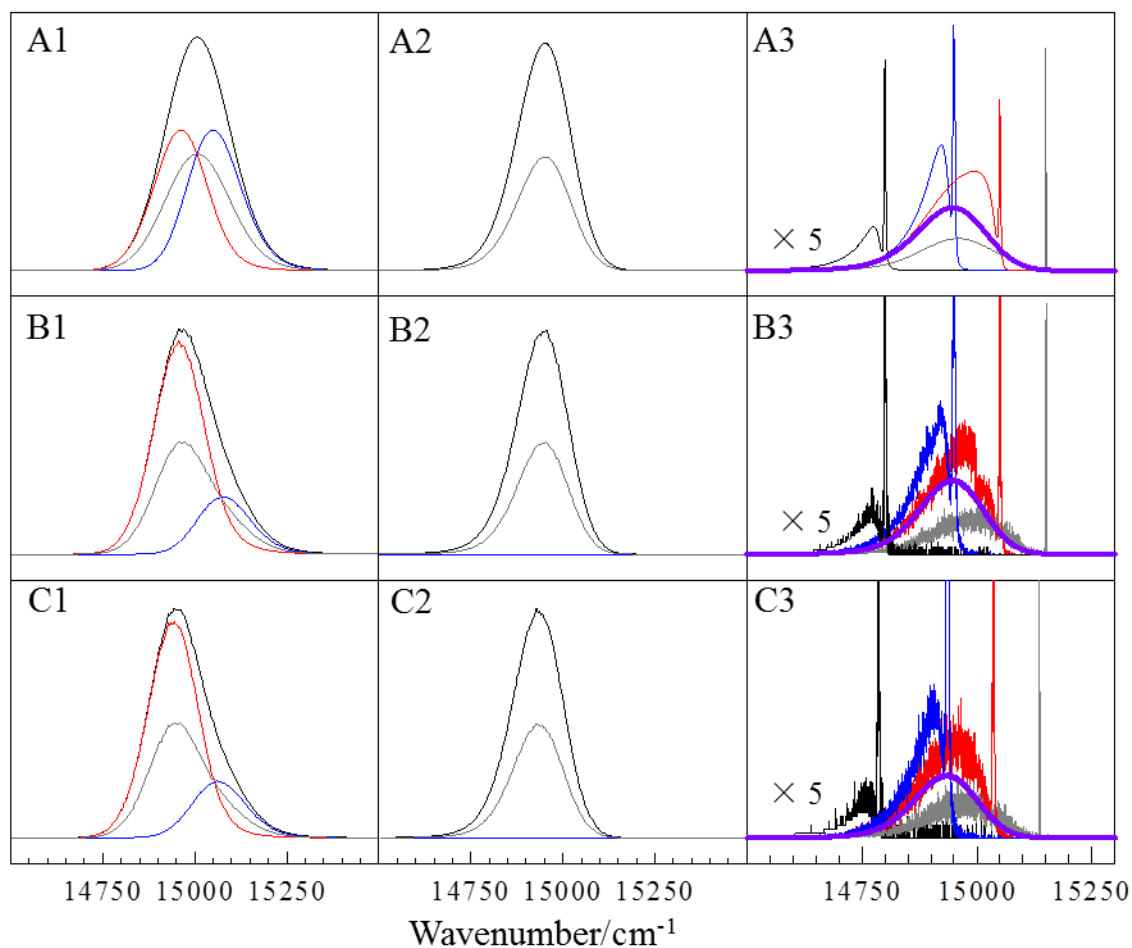


Figure A-3. Calculated spectra of weakly coupled dimer with degenerate site energy at 15000 cm^{-1} . Coupling constant is 25 cm^{-1} ; inhomogeneous broadening is 200 cm^{-1} ; Huang-Rhys factor S equals to 0.2. In the first two columns, black lines are calculated bulk spectra; red and blue curves are contributions from the pigments with lower and higher energy, respectively; gray lines are contribution from each pigment. In the third column, black, blue, red, and gray spectra are collected with excitation wavenumber at 14800 cm^{-1} , 14950 cm^{-1} , 15050 cm^{-1} , and 15150 cm^{-1} , respectively (excitation frequencies are red-shifted by 14 cm^{-1} in RC-approach to correct the shift due to reorganization energy).

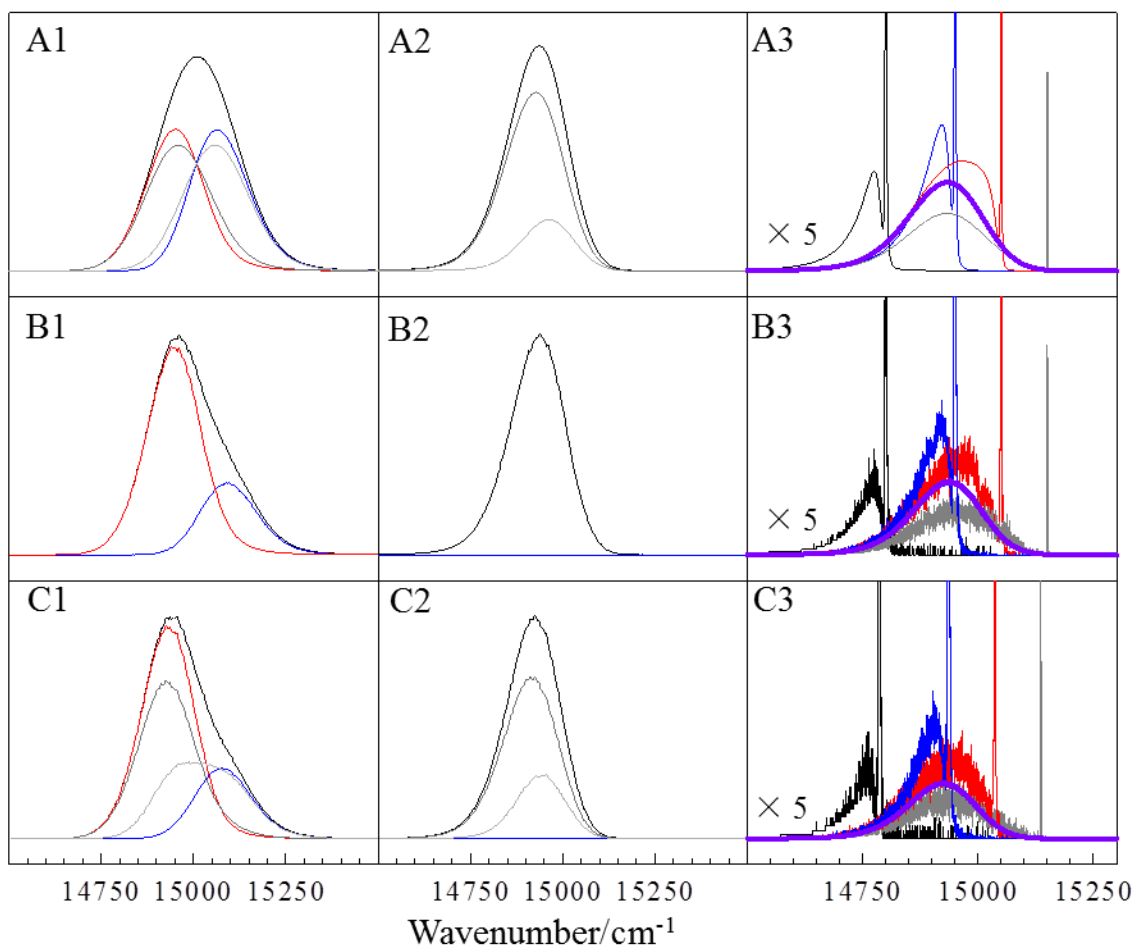


Figure A-4. Calculated spectra of weakly coupled dimer site energies at 14950 cm⁻¹ and 15050 cm⁻¹. Coupling constant is 25 cm⁻¹; Huang-Rhys factor S equals to 0.2.

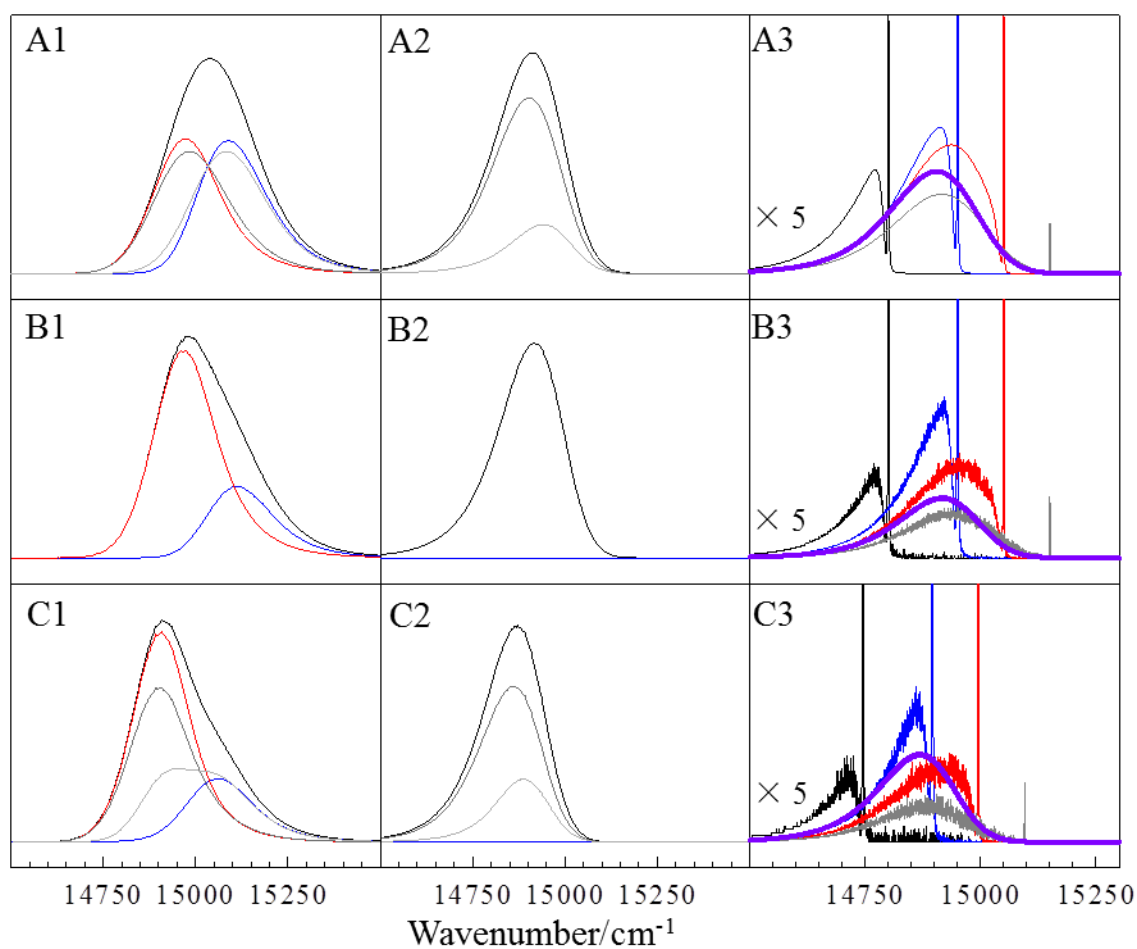


Figure A-5. Calculated spectra of weakly coupled dimer site energies at 14950 cm^{-1} and 15050 cm^{-1} . Coupling constant is 25 cm^{-1} ; inhomogeneous broadening is 200 cm^{-1} ; Huang-Rhys factor S equals to 0.8. In the third column, black, blue, red, and gray spectra are collected with excitation wavenumber at 14800 cm^{-1} , 14950 cm^{-1} , 15050 cm^{-1} , and 15150 cm^{-1} , respectively (excitation frequencies are red-shifted by 55 cm^{-1} in Redfield theory calculation to corrected the shift due to reorganization energy).